COPPE
Instituto Alberto Luiz Coimbra de Pós-Graduação e Pesquisa de Engenharia
UFRJ

AN OPTIMAL DESIGN MODEL FOR SANDWICH PIPE CONSIDERING STRUCTURAL AND THERMAL INSULATION REQUIREMENTS

Jiankun Yang

Tese de Doutorado apresentada ao Programa de Pós-graduação em Engenharia Oceânica, COPPE, da Universidade Federal do Rio de Janeiro, como parte dos requisitos necessários à obtenção do título de Doutor em Engenharia Oceânica.

Orientadores: Segen Farid Estefen
Marcelo Igor Lourenço de Souza

Rio de Janeiro
Julho de 2020

AN OPTIMAL DESIGN MODEL FOR SANDWICH PIPE CONSIDERING STRUCTURAL AND THERMAL INSULATION REQUIREMENTS

Jiankun Yang

TESE SUBMETIDA AO CORPO DOCENTE DO INSTITUTO ALBERTO LUIZ COIMBRA DE PÓS-GRADUAÇÃO E PESQUISA DE ENGENHARIA DA UNIVERSIDADE FEDERAL DO RIO DE JANEIRO COMO PARTE DOS REQUISITOS NECESSÁRIOS PARA A OBTENÇÃO DO GRAU DE DOUTOR EM CIÊNCIAS EM ENGENHARIA OCEÂNICA.

Orientadores: Segen Farid Estefen
Marcelo Igor Lourenço de Souza

Aprovada por: Prof. Segen Farid Estefen
Prof. Marcelo Igor Lourenço de Souza
Prof. Ilson Paranhos Pasqualino
Prof. Su Jian
Prof. Virgílio José Martins Ferreira Filho
Prof. Celso Pupo Pesce

RIO DE JANEIRO, RJ – BRASIL
JULHO DE 2020

Yang, Jiankun

An optimal design model for sandwich pipe considering structural and thermal insulation requirements/Jiankun Yang. – Rio de Janeiro: UFRJ/COPPE, 2020.

XIX, 149 p.: il.; 29, 7cm.

Orientadores: Segen Farid Estefen

Marcelo Igor Lourenço de Souza

Tese (doutorado) – UFRJ/COPPE/Programa de Engenharia Oceânica, 2020.

Referências Bibliográficas: p. 127 – 140.

1. Sandwich pipe. 2. Collapse pressure. 3. Thermal insulation. 4. Optimization. I. Estefen, Segen Farid *et al.* II. Universidade Federal do Rio de Janeiro, COPPE, Programa de Engenharia Oceânica. III. Título.

To my dear family for their endless love, support and encouragement

Acknowledgement

It would not be possible to accomplish the present thesis without supports from many people. First, I would like to express my sincere gratitude to my supervisor, Prof. Segen Farid Estefen, not only for his guidance and help during my time in Rio, but also for setting a great example showing me how to be an excellent scholar. I would always remember those days working with him. His patience and concentration have been a great inspiration to me.

I would like to thank my co-supervisor, Prof. Marcelo Igor Lourenço de Souza. Because of your help and suggestion, I achieved my first journal article, which gave me substantial confidence in my research ability. Thank you for all the insightful comments and ideas. I have learned a lot from all the enthusiastic discussions.

Special thaks to Dr. Claudio M.Paz, Thank you for your help with the software Abaqus and sharing experimental results with me. I also would like to thank Dr. Lu Hailong and Dr. Zhu Lei, thank you for your help and suggestions on my work.

Many thanks to all my friends here in Rio. I never felt lonely because I have a bunch of good friends. Thank all my Brazilian friends for teaching me Portuguese and explaining to me patiently every time I got confused in a Portuguese conversation. All the travelings we made, celebrations of the special days, the barbecues we prepared, the efforts we paid in Crossfit and the swimming pool, have made my life quite colorful in Rio de Janeiro. Studying and living together with them has been a pleasure for me.

The financial support from the Brazilian National Council for the Improvement of Higher Education (CAPES) is gratefully acknowledged. Many thanks also go to the PENO and staff of LTS for all the help during my doctoral study.

I am also grateful for the support from the China Scholarship Council (CSC), not only the financial support but also allowing me such a valuable opportunity.

Last, but certainly not least, to my family: my parents, Chunling Ge and Hong Yang, thanks for their endless love encouraging me to insist on my study. I would not have reached this stage without their support.

Resumo da Tese apresentada à COPPE/UFRJ como parte dos requisitos necessários para a obtenção do grau de Doutor em Ciências (D.Sc.)

UM MODELO DE PROJETO IDEAL PARA TUBO SANDUÍCHE, CONSIDERANDO OS REQUISITOS ESTRUTURAL E DE ISOLAMENTO TÉRMICO

Jiankun Yang

Julho/2020

Orientadores: Segen Farid Estefen
Marcelo Igor Lourenço de Souza

Programa: Engenharia Oceânica

Duto sanduíche (DS) é uma solução promissora para aplicações em águas ultraprofundas. Devido à vasta possibilidade de escolhas do material e da espessura de cada camada, o projeto pode desenvolvido para cenários específicos. O objetivo da tese é investigar um método de projeto ótimo para dutos sanduíche baseado em requisitos estrutural e de isolamento térmico. Resultados de testes experimentais de DSs submetidos à pressão externa são correlacionados com aqueles de modelo de elementos finitos não-linear. Um estudo paramétrico é então conduzido, para ampla faixa de variáveis, para analisar o comportamento de colapso de DS em escala real com anular constituído de compósito cementício com encruamento (SHCC). Uma equação é proposta para o colapso de DS baseada em resultados numéricos, utilizando técnicas de aprendizado supervisionado e algoritmos estocásticos. O programa computacional OLGA é empregado para analisar o desempenho do isolamento térmico do DS com anular de SHCC. Um modelo matemático para a transferência de calor do DS é desenvolvido para as condições de fluxo contínuo e interrupção de fluxo. Um modelo para estimativa de custo de DSs, incluindo os custos de material, fabricação e soldagem, é também considerado. Um modelo de programação não-linear "mixed-integer", incorporando requisitos estrutural e de isolamento térmico, é estabelecido para o projeto ótimo de configurações de DS sob diferentes condições de trabalho.

Abstract of Thesis presented to COPPE/UFRJ as a partial fulfillment of the requirements for the degree of Doctor of Science (D.Sc.)

AN OPTIMAL DESIGN MODEL FOR SANDWICH PIPE CONSIDERING STRUCTURAL AND THERMAL INSULATION REQUIREMENTS

Jiankun Yang

July/2020

Advisors: Segen Farid Estefen
Marcelo Igor Lourenço de Souza

Department: Ocean Engineering

Sandwich pipe (SP) is a promising solution in ultra-deepwater applications. Due to the vast choices of materials and thicknesses for each layer, the design process can be tailored for a specific scenario. The purpose of the thesis is to investigate an optimal design method for sandwich pipes based on structural and thermal insulation requirements. Experimental test results of SPs subjected to external pressure are correlated with those from a nonlinear finite element model. A parametric study is then conducted for a wide range of variables to analyze the collapse behavior of full-scale SP with strain-hardening cementitious composite (SHCC) core. An equation to predict the SP collapse pressure is proposed based on the numerical results using supervised learning techniques and stochastic algorithms. The software OLGA is employed to analyze the insulation performance of the SP with the SHCC core. A mathematical model for the SP heat transfer is developed under both steady-state and shut-in conditions. A cost estimate model for SPs, including material cost, fabrication cost, and welding cost, is also considered. A mixed-integer nonlinear programming model, incorporating structural and thermal insulation requirements, is established for the optimal design of the SP. The performance of the proposed model is evaluated in a case study. Finally, a parametric study is conducted to investigate the optimal SP configurations under different working conditions.

Contents

List of Figures **x**

List of Tables **xiv**

List of Symbols **xvi**

List of Abbreviations **xviii**

1 Introduction **1**

1.1 Overview 1

1.2 Motivation and objectives 3

1.3 Thesis organization 5

2 Literature review **8**

2.1 The core materials of SPs 8

2.2 SP collapse under external hydrostatic pressure 13

2.2.1 Analytical solutions 13

2.2.2 Experiments 15

2.2.3 Numerical simulations 15

2.2.4 Empirical equations 19

2.3 Installation of SPs 20

2.4 Thermal insulation of SPs 23

2.4.1 Thermal management of subsea pipelines 23

2.4.2 Heat conduction in multilayer structuress 26

2.5 Optimum design methods of subsea pipelines 27

2.5.1 Thermal insulation requirements and insulation thickness . . . 27

2.5.2 Structural requirements and wall thickness 29

2.5.3 Machine learning and optimization algorithms 30

2.6 Summary 32

3 Collapse pressure of SHCC SPs **34**

3.1 Experiments and parametric study 35

3.1.1 Experiments and Results . . . 35
3.1.2 Finite Element Model . . . 38
3.1.3 Parametric Study . . . 43
3.2 A suitable prediction equation . . . 55
3.2.1 Analytical solution . . . 56
3.2.2 Empirical solution . . . 58
3.3 Summary . . . 70

4 Thermal analyses of SP **73**
4.1 Insulation performance of the SHCC SP . . . 73
4.1.1 Subsea production system and pipeline geometry . . . 73
4.1.2 Flow assurance analyses . . . 76
4.1.3 Volumetric heat capacity and energy storage . . . 79
4.2 A thermal analysis model for SPs . . . 84
4.3 Summary . . . 90

5 An optimization model for the SP **92**
5.1 An MINLP model for SP optimal design . . . 92
5.1.1 Problem description . . . 92
5.1.2 Mathematical Model . . . 94
5.1.3 Model solving . . . 101
5.2 Case study . . . 103
5.3 Parametric study . . . 107
5.3.1 Parameter range . . . 107
5.3.2 Results and discussion . . . 109
5.4 Summary . . . 118

6 Conclusion and future work **122**
6.1 Overall summary . . . 122
6.2 Conclusion . . . 123
6.3 Future work . . . 125

Bibliography **127**

A Analytical solution for elastic collapse pressure of the SP **141**

List of Figures

1.1 Distribution of the main global deepwater basins 2
1.2 Schematic of single-wall pipe 3
1.3 Schematic of sandwich pipe with extra insulation layer 3
1.4 Schematic of pipe-in-pipe system 4

2.1 Stress-strain curves of the PP under different temperatures 9
2.2 Stress-strain curves of the ECC and plain concrete under uniaxial tensile test 10
2.3 Sandwich pipes with different core materials: (a) PP core; (b) cement core; (c) collapsed SP with PP core; (b) SP with SHCC core 11
2.4 Illustration of PCM incorporated cementitious composite 12
2.5 Sketch of the hyperbaric chamber for the SP collapse experiment . . . 15
2.6 Collapse experiment:(a) Putting the intact sample in the pressure vessel; (b) Collapsed sample 16
2.7 S-lay installation 20
2.8 J-lay installation 21
2.9 Reeling-lay installation 22
2.10 Reeling process scheme 22
2.11 Threaded SP connector by Quispe et al. 23
2.12 Schematic of temperature and pressure condition from reservoir to flowline 24
2.13 Cost and insulation thickness 28

3.1 Mechanical characteristics of stainless steel 35
3.2 Tested strain-stress relationships and fitted curves 36
3.3 Measurement of the geometric imperfection of a pipe: (a) Illustration of geometric imperfection; (b) Measuring pipe shape with FARO arm; (c) Mark the cross sections along the length 38
3.4 Mesh sensitivity study 39
3.5 2D finite element model for the SP system 39

3.6 Comparison of numerical results and experiments for prototypes using SS304 42
3.7 Comparison of numerical results and experiments for prototypes using SS316 42
3.8 Applicable limits and commercially available dimensions for steel pipes 43
3.9 Effect of outer pipe thickness-to-radius ratio on the collapse pressure of the SP system: (a) SP with thick core $r_1/r_3 = 0.65$; (b) SP with moderately thick core $r_1/r_3 = 0.73$; (c) SP with thin core $r_1/r_3 = 0.82$; 45
3.10 Illustration of different definitions for the pipe radius 46
3.11 SP configurations with the same r_1/r_3 and different t_3/r_3: (a) $t_3/r_3 = 0.02$; (b) $t_3/r_3 = 0.03$; (c) $t_3/r_3 = 0.05$; (d) $t_3/r_3 = 0.06$; (e) $t_3/r_3 = 0.08$ 47
3.12 P_{co} of the SP system and P_{co} of each layer in the SP system with respect to t_3/r_3 47
3.13 Characteristic responses of the SP systems with increasing thickness of outer steel pipe (Frictionless inter-layer condition) 48
3.14 Characteristic responses of component layers of the SP: the core layer of the SP-a and outer steel layer of the SP-e 48
3.15 Characteristic responses of the SP systems with increasing thickness of outer steel pipe (Fully bonded inter-layer condition) 50
3.16 Von Mises stress and the cross-section deformation of SPs with the frictionless inter-layer condition at the collapse pressure: (a) $t_3/r_3 = 0.02$; (b) $t_3/r_3 = 0.03$; (c) $t_3/r_3 = 0.05$; (d) $t_3/r_3 = 0.06$; (e) $t_3/r_3 = 0.08$ 51
3.17 Equivalent plastic strain and the cross-section deformation of SPs with the frictionless inter-layer condition at the collapse pressure: (a) $t_3/r_3 = 0.02$; (b) $t_3/r_3 = 0.03$; (c) $t_3/r_3 = 0.05$; (d) $t_3/r_3 = 0.06$; (e) $t_3/r_3 = 0.08$ 52
3.18 Effect of inner thickness-to-radius ratio on the collapse pressure of the SP system: (a) SP with thick core $r_1/r_3 = 0.65$; (b) SP with moderately thick core $r_1/r_3 = 0.73$; (c) SP with thin core $r_1/r_3 = 0.82$ 53
3.19 Characteristic responses of the SP systems with increasing thickness of inner steel pipe(Frictionless inter-layer condition) 53
3.20 Characteristic responses of SP systems with different core thicknesses (Frictionless inter-layer condition) 54
3.21 Geometric imperfection vs Collapse pressure: (a) SP with $Imp_1 = 0.2\%$; (b) SP with $Imp_3 = 0.2\%$ 55
3.22 Characteristic responses of SPs with different geometric imperfection 55
3.23 Influence of steel grade on the collapse pressures of SPs 56
3.24 The prediction accuracies of the trained equations proposed in the thesis. 64

3.25 The prediction accuracies of the trained equations proposed by previous researchers and by EUREQA. 65
3.26 P_{co} with respect to t_3/r_3 by ABAQUS vs Equation (d): (a) thick core ($r_1/r_3 = 0.65$), (b) moderate core ($r_1/r_3 = 0.73$), and (c) thin core ($r_1/r_3 = 0.82$). 66
3.27 Experimental test versus Equation (d) 68
3.28 Experimental test versus modified results by Equation (d) 69

4.1 Subsea production system 74
4.2 Pressure versus Temperature (Steady-state, Cluster A1) 76
4.3 Pressure versus Temperature (Steady-state, Cluster A2) 76
4.4 Pressure versus Temperature (Shut-in, Cluster A1) 77
4.5 Pressure versus Temperature (Shut-in, Cluster A2)) 77
4.6 Pressure versus Temperature (Shut-in, Cluster A1) 78
4.7 Pressure versus Temperature (Shut-in, Cluster A2)) 78
4.8 Required insulation thickness for the SP, the SW and the FP 79
4.9 U-values and heat capacities of SP, SW, FP and PIP 79
4.10 Leaking barrel as an analogy with pipeline heat loss in the shut-in condition 80
4.11 Required insulation thickness for the SP in the steady-state condition(Cluster A1) 81
4.12 Required insulation thickness for the SP in the shut-in condition(Cluster A1) 81
4.13 Sketch illustrating the energy conservation of the fluid in an SP element 85
4.14 Cross section area of the SP pipeline 85
4.15 Temperature distributions calculated by the model and OLGA 89
4.16 Temperature variation with time in the shut-in condition at x = 3000m 90

5.1 Logical relations among variables and constraints 94
5.2 Flowchart the of the GA-PSO algorithm 103
5.3 SP Cost and Structural constraint violation of each iteration 104
5.4 Violation of thermal insulation constraints of each iteration 104
5.5 Cost comparison of SPs and SW 106
5.6 A typical subsea production system 107
5.7 Costs and constraints violations of the optimal SPs at type 1 location under different working conditions ($T_{hydrate} = 20°C$): (a) Costs; (b) Structural violation; (c) Steady-state violation; (d) Shut-in violation 111
5.8 Thicknesses of each layer of the optimal SPs at type 1 location under different working conditions ($T_{hydrate} = 20°C$): (a) t_1; (b) t_2; (c) t_3; (d) t_4 112

5.9 Cost ratios of the optimal SPs and the optimal SWs at type 1 location under different working conditions ($T_{hydrate} = 20°C$) 112
5.10 Costs and constraints violations of the optimal SPs at type 2 location under different working conditions ($T_{hydrate} = 20°C$): (a) Costs; (b) Structural violation; (c) Steady-state violation; (d) Shut-in violation 114
5.11 Thicknesses of each layer of the optimal SPs at type 2 location under different working conditions ($T_{hydrate} = 20°C$): (a) t_1; (b) t_2; (c) t_3; (d) t_4 115
5.12 Cost ratios of the optimal SPs and the optimal SWs at type 2 location under different working conditions ($T_{hydrate} = 20°C$) 115
5.13 Costs and constraints violations of the optimal SPs at type 3 location under different working conditions ($T_{hydrate} = 20°C$): (a) Costs; (b) Structural violation; (c) Steady-state violation; (d) Shut-in violation 116
5.14 Thicknesses of each layer of the optimal SPs at type 3 location under different working conditions ($T_{hydrate} = 20°C$): (a) t_1; (b) t_2; (c) t_3; (d) t_4 117
5.15 Cost ratios of the optimal SPs and the optimal SWs at type 3 location under different working conditions ($T_{hydrate} = 20°C$) 117
5.16 Costs and constraints violations of the optimal SPs at type 4 location under different working conditions ($T_{hydrate} = 20°C$): (a) Costs; (b) Structural violation; (c) Steady-state violation; (d) Shut-in violation 118
5.17 Thicknesses of each layer of the optimal SPs at type 4 location under different working conditions ($T_{hydrate} = 20°C$): (a) t_1; (b) t_2; (c) t_3; (d) t_4 119
5.18 Cost ratios of the optimal SPs and the optimal SWs at type 4 location under different working conditions ($T_{hydrate} = 20°C$) 119

A.1 (a) Geometry of the sandwich pipe cross-section; (b) Stresses at the interfaces between the core layer and the steel layers 141

List of Tables

2.1 Properties of the proposed core materials of SPs 10
2.2 Numerical models for SPs by previous researchers 18

3.1 Geometrical parameters for sandwich pipes 37
3.2 Collapse pressures of sandwich pipes 37
3.3 Parameter ranges for the parametric study 44
3.4 Parameters for different SP configurations 45
3.5 Comparison between collapse pressures by Sato and Arjomandi with experimental results 57
3.6 Comparison between collapse pressures by Sato and Arjomandi with experimental results 57
3.7 Summary of all the equation forms tested. 62
3.8 Prediction error and SP configurations 67
3.9 Prediction error and SP configurations 68
3.10 The trained constants for Equation (d). 69
3.11 Parameters used for the feature scaling for Equation (d). 70

4.1 Subsea pipeline lengths 75
4.2 Subsea pipeline configurations 75
4.3 Properties of the insulation material 75
4.4 Thermal properties of commonly used insulation materials 82
4.5 Layer thicknesses for Scenario 1 and 2 83
4.6 SP configuration for model validation 88
4.7 Related thermal properties 89
4.8 Temperature and flow rate information 89

5.1 Price coefficient of steel grade 95
5.2 Price of different insulation materials. 96
5.3 Thermal properties of different materials for each layer 98
5.4 Oil properties 98
5.5 Settings of materials parameters 100
5.6 Input parameters for case study 103

5.7 Pipeline configurations and costs 105
5.8 Cost composition for each pipe configuration 105
5.9 Assumed input parameters and pipeline location 108
5.10 Parameter ranges for the parametric study 108
5.11 Employment frequency of each material in the optimal SP configurations at 4 types of location 113

List of Symbols

$i = 1$	stands for the inner steel layer of an SP
$i = 2$	stands for the core layer of an SP
$i = 3$	stands for the outer steel layer of an SP
$i = 4$	stands for the extra insulation layer of an SP
t_i	wall thickness of the i-th layer
r_i	outside radius of the i-th layer
D_i	outside diameter of the i-th layer
T_i	temperature of the i-th layer
r_c	average radius of the core layer ($r_c = \frac{(r_1+r_3)}{2}$)
Imp_i	geometric imperfection of the i-th layer
Imp_c	average imperfection of the core layer ($Imp_c = \frac{(Imp_1+Imp_3)}{2}$)
C_i	cost per unit length of the i-th layer
Cir_i	perimeter of the i-th layer
lb_i	lower bound of the thickness of the i-th layer
ub_i	upper bound of the thickness of the i-th layer
α_1	steel grade parameter of the steel layers
α_2	material parameter of the core layer
α_3	material parameter of the insulation layer
E_p	Young's modulus of steel
σ_p	steel yield stress

v_p	Poisson's ratio of steel
ρ	material density
k	thermal conductivity
c	specific heat per mass
P_{co}	collapse pressure
$P_{predict}$	collapse pressure provided by prediction models
h_{wd}	water depth
g	gravitational acceleration
M_f	fluid mass flow rate
L	total length of a pipeline
$T_{require}$	required minimum fluid temperature in the steady-state condition
T_{sea}	sea water temperature
T_{in}	inlet fluid temperature
$t_{require}$	required cool-down time in the shut-in condition
E_c	elastic modulus of the SP core layer
v_c	Poisson's ratio of the SP core layer

List of Abbreviations

SP	Sandwich Pipe
SW	Single-Wall pipe
PIP	Pipe-In-Pipe
FP	Flexible Pipe
FE	Finite Element model
SHCC	Strain-Hardening Cementitious Composite
PP	Polypropylene
SPP	Syntatic Polypropylene
PSO	Particle Swarm Optimization
GA	Genetic Algorithm
ML	Machine Learning
MINLP	Mixed-Integer Nonlinear Programming
VHC	Volumetric Heat Capacity
PCM	Phase Change Material
TDP	Touch Down Point
WAT	Wax Appearance Temperature
PP SP	Sandwich Pipe with PP core
SHCC SP	Sandwich Pipe with SHCC core
CDP	Concrete Damage Plasticity
DP	Drucker-Prager model

PEEK	Poly-Ether-Ether-Ketone
PC	Polycarbonate
SEF	Syntactic Epoxy Foam
HDPF	High Density Polyimide Foam
SFRC	Steel Fiber Reinforced Concrete
ECC	Engineered Cementitious Composite
PCM-RBA	PCM integrated Recycled Brick Aggregates
U-value	Overall Heat Transfer Coefficient
GOR	Gas Oil Ratio

Chapter 1

Introduction

1.1 Overview

Oil and natural gas have been major sources of energy supply for the world and will continue to do so over several decades. As onshore and shallow water reserves and production capacity decline, the oil industry shifts its attention to the deepwater and ultra-deepwater fields. From 2012 to 2014, over 70% of the top 10 annual oil and gas discoveries were made in deepwater regions[1]. Besides, the oil and gas reserves in deepwater areas account for 44% of the total offshore oil and gas reserves worldwide. Figure 1.1 shows the distribution of the main global deepwater basins.

The concept of deepwater is actually dynamic and is constantly changing with the progress in offshore technology. Currently, offshore oil fields with a water depth of 300 m are considered deepwater and those with water depth over 1500 m are classified as ultra-deep water. In deepwater and ultra-deep water applications, the conventional single-wall (SW) pipe (Figure 1.2), due to the excessive steel pipe thickness needed to withstand the extremely high hydrostatic pressure, becomes expensive and difficult to install. Further, the low water temperature incorporating high fluid pressure causes severe flow assurance problems to SWs [2, 3]. Aiming at solving the related challenges, Paqualino et al. [4], Netto et al. [5], and Estefen et al. [6] initially proposed the concept of sandwich pipes (SP) as an alternative solution for deepwater applications. An SP is composed of two steel tubes separated by a core layer that can be filled by materials with good structural strength and adequate thermal insulation properties. Further, an extra insulation layer can be applied outside the outer steel pipe of an SP when high thermal insulation is required. Figure 1.3 shows the schematic of an SP. Since the core layer provides both structural resistance and thermal insulation, SPs are able to provide high structural strength using relatively thin steel tubes while attending the thermal insulation requirements. By employing thin steel tubes, replacing the SW with the SP decreases both weight

and cost of the pipeline for deepwater applications.

Figure 1.1: Distribution of the main global deepwater basins (adapted from [1])

Since the pipe-in-pipe (PIP) systems also consist of two concentric steel pipes separated by a core layer (Figure 1.4), the configurations of PIPs and SPs are quite similar. And the PIP receives more attention since it was proposed earlier than the SP. Therefore, sometimes the SP is misrecognized as the PIP. In fact, PIPs and SPs differ from each other in several aspects. When applying single-wall (SW) pipes fails to solve flow assurance problems, PIP systems, incorporating nonstructural insulation material or hot water in its core layer, are employed to deliver excellent thermal insulation. Besides, the annular space of PIP systems is also used for well injection, umbilical cables, active heating systems, etc. In the case of SPs, the core layer is filled with low-cost materials with adequate thermal insulation properties and good structural resistance. The application of SP systems is not to provide excellent thermal insulation but to reduce both pipeline cost and its submerged weight, while maintaining adequate thermal insulation and good structural strength for deep-water application. Usually, the core layer of PIPs only provides thermal insulation properties without structural resistance, while that of SPs combines both structural functionality and thermal insulation. For the PIP, inner and outer steel pipes are designed independently against failure under internal and external pressures while in the SP the design integrates all the three layers to resist the acting pressure loads. Since the inner pipe and outer pipe of PIPs independently withstand operational loads, thick steel pipes are still needed for PIPs in the deep-water applications.

Sandwich pipes can be an effective solution for applications where thermal insulation, resistance to excessive external pressure and reduction of buoyancy weight during the installation process are required. Thus, the SP is suitable for severe conditions involved high hydrostatic pressure and low temperature which are observed normally in Brazil's pre-salt reservoir [7] and in Arctic offshore exploration [8].

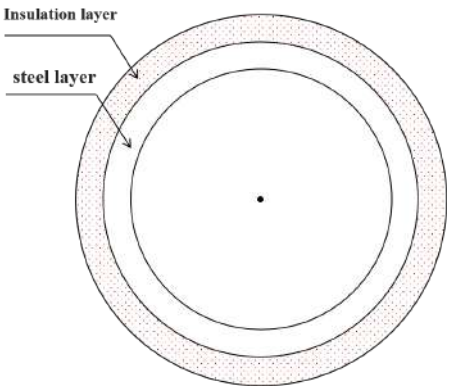

Figure 1.2: Schematic of single-wall pipe

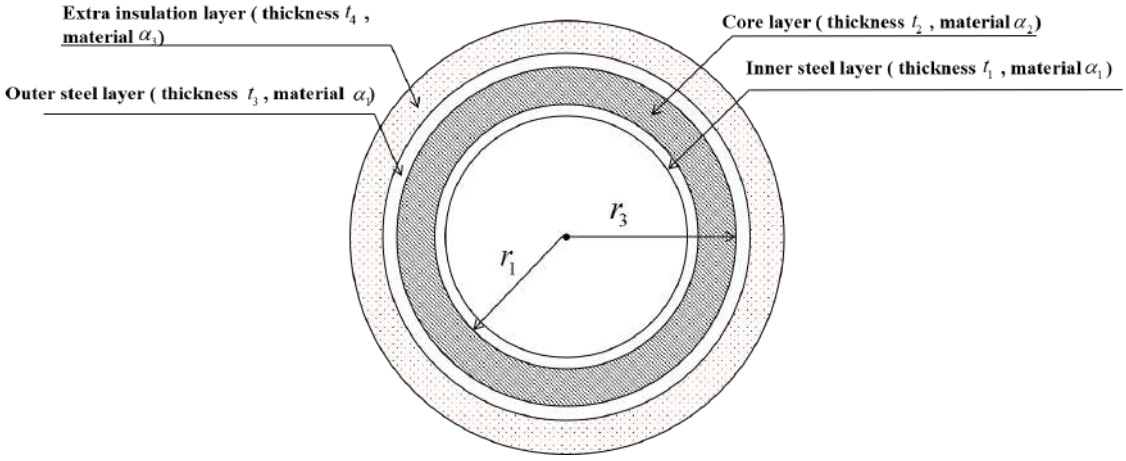

Figure 1.3: Schematic of sandwich pipe with extra insulation layer

1.2 Motivation and objectives

After decades of research on sandwich pipes, previous researchers have evaluated the feasibility, benefits, and limitations of the application of sandwich pipes in deep-water scenarios in terms of structural integrity, thermal insulation performance, and suitable joining methods. Sandwich pipes are proven to be promising solutions for ultra-deep-water applications. A wise design method is essential for a successful application of sandwich pipes. As concluded by Netto et al. [5], the design of sandwich pipes shall be tailored based on the specifics of each scenario because of

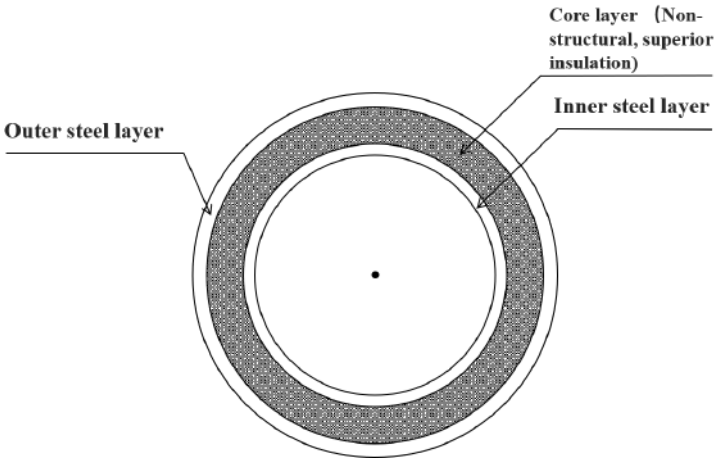

Figure 1.4: Schematic of pipe-in-pipe system

the wide range of choices. Despite the fact that considerable researches on sandwich pipes were reported in the literature, few studies discussed the design method of sandwich pipes. Up to now, a comprehensive optimal design model of sandwich pipes has not been reported in the literature. Castello et al. [9] briefly presented a design procedure for sandwich pipes without further investigation of the optimal design. Using a simplified cost function, Arjomandi and Taheri [10] presented a general procedure of the optimal design of a sandwich pipe without presenting an optimization model. More recently, a D.Sc. thesis by Basto [11] initially investigated the optimal design of the SP. In his proposed optimization model, the material costs of the SP section and the threaded connector were selected as the objective function. The required collapse pressure and the maximum tensile stress were set as the structural constraints. And the required overall heat transfer coefficient was employed as the thermal insulation constraints. However, the proposed optimization model can be improved in several aspects like considering the thermal insulation requirements in the shut-in condition or including more available materials in the design.

Subsea pipelines like single-wall pipes and pipe-in-pipes are designed so that each layer of the pipe provides a single functionality. The steel layer only provides structural strength, while the insulation layer only gives thermal insulation. Therefore, for a given scenario, the design of SWs and PIPs involve determining the material and thickness of the steel layer to meet structural requirements and that of the insulation layer to meet the thermal insulation requirements, respectively [12, 13]. However, the same design procedure is not suitable in the case of sandwich pipes. As the core layer of sandwich pipes provides both structural resistance and thermal insulation, different choices of the thickness and material for the core layer affect both structural resistance and thermal insulation of the whole SP system and, thus, affect the choices of thicknesses and materials of both steel layers and the extra insulation

layer. Therefore, sandwich pipes need an integral design procedure considering all the layers. Furthermore, for a certain scenario, the configuration of SPs that can meet the application requirements is not unique. Several configurations of SPs that combine different material and thickness of each layer can provide proper structural resistance and thermal insulation. How to optimally design sandwich pipes with a wide range of choices remain unanswered.

Based on the above observations, the thesis is dedicated to developing a suitable optimal design model for sandwich pipes so that their advantages can be fully exploited. The model can serve as a reference for standard design method of SPs. To construct the optimal model, the structural strength and thermal insulation of SPs should be analyzed first. The main objectives of the investigations presented in the thesis can be summarized as:

- To investigate the collapse pressure and the post-buckling behavior of several SPs with SHCC cores and to propose a suitable prediction equation of the collapse pressure;
- To evaluate the thermal insulation performance of SPs and to develop a mathematical model for the analysis of heat transfer in SPs;
- To develop a design model for the optimization of SPs.

1.3 Thesis organization

The innovative contributions achieved throughout the thesis are concluded as follows:

1. An unusual collapse behavior of the SHCC SP with frictionless inter-layer adhesion, which has not been reported previously, is observed and thoroughly discussed. The results improve the understanding of the mechanical behavior of SPs with weak inter-layer adhesions.
2. Based on supervised learning techniques, a suitable prediction equation for the collapse pressure of SHCC SPs, which captures its special behavior, is proposed.
3. An optimal design model is initially developed, which fills the theoretical gap and provides a reference for possible design criteria of SPs in the future.

Chapter 2 – Literature review

This chapter systematically reviews related researches of SPs, providing some of its historical backgrounds and recent outcomes. With the objective of developing

an optimization model, existing materials for the core and insulation layers are summarized to define the possible choices for the SP optimization model. Special attention is paid to the prediction methods of the SP collapse pressure as well as the researches on thermal analyses related to flow assurance problems in a multi-layer pipeline. Basic theories and applications of machine learning techniques and optimization algorithms are introduced.

Chapter 3 – Collapse pressure of SHCC SPs

In this chapter, experiments of collapse under external pressure are carried out on SPs composed of two steel tubes and SHCC core. The experimental results have been employed in the correlation studies with the finite element model using the software ABAQUS. The proposed numerical model has been used in a parametric study for the collapse simulation of 6,000 different practical configurations. The influence of geometric parameters and material properties of the SP on its collapse pressure under external pressure and post-buckling behavior are systematically analyzed. Additionally, based on the extensive simulation results, supervised machine learning techniques are applied to support the regression for equations in different forms. Finally, one suitable prediction equation of the SHCC SP collapse pressure is obtained.

Chapter 4 – Thermal analyses of SPs

Chapter 4 evaluates the insulation performance of the SHCC SP using the professional multiphase computational software OLGA[14]. A case study is conducted assuming a subsea production system with depth at 2200m for a comprehensive evaluation of the insulation performance of the sandwich pipe, including both the steady-state and the shut-in working conditions. For a comparative study, scenarios using single-wall pipe (SW), pipe-in-pipe (PIP), and flexible pipe (FP) are also considered separately. Further, a mathematic model for the analysis of heat transfer in SPs is developed to provide a quick prediction of the minimum fluid temperature in the steady-state condition and the cool-down time in the shut-in condition.

Chapter 5 – An optimization model of SPs

Chapter 5 describes the optimal design model of SPs. A cost model of SPs is initially proposed. Along with the results from Chapters 3 and 4, a mixed-integer nonlinear programming (MINLP) model for the optimal SP is developed. The optimization model is employed in a case study where the optimal SP is compared with single-wall pipes (SW) and SPs developed by the existing design method. A parametric study that combines 540 practical subsea working conditions is then carried out. Further, similar to the established optimization model, an optimization model of SWs is also developed. Finally, the cost ratios of the optimal SPs and the optimal SWs under different working conditions are calculated where the preferred application conditions of SPs are discussed.

Chapter 6 – Conclusions and future work

The final chapter summarizes the principal conclusions obtained during the thesis preparation as well as the contributions of the thesis. The future potential works are indicated by pointing out some of the important works that exceed the scope of the thesis.

Chapter 2

Literature review

2.1 The core materials of SPs

The core layer of the SP is supposed to provide both structural strength and thermal insulation. However, for a certain material, a higher structural strength usually leads to lower thermal insulation capacity. Thus, it is crucial for the choice of the core material to balance the mechanical and thermal performances of the SPs. Besides, parameters like density, cost, and maximum service temperature should also be considered to deliver a good overall performance.

Due to their wide availability and relatively low cost, plain cement and polypropylene (PP) were initially proposed as the SP core materials by Estefen et al. [6]. Since then, the proposed core materials follow two general categories, the polymer-based, and cement-based materials. Souza et al. [15] conducted a great job on the evaluation of several polymer-based materials for SP applications. Considering factors that include the density, yield strength, yield elongation, thermal conductivity, maximum service temperature, and the cost, they employed a digital logic approach to assess the applicability of several polymeric materials. In addition to the PP, the authors recommended the poly-ether-ether-ketone (PEEK) and the polycarbonate (PC) as potential SP core materials. Castello [16] investigated the applicability of the syntactic epoxy foam (SEF) and high density polyimide foam (HDPF) for SPs. SEF is a composite material synthesized by filling an epoxy resin matrix with hollow glass microspheres, which has almost the same yield strength but only half of the thermal conductivity. Except for the high price, HDPF is an advanced thermoplastic elastomer with excellent mechanical and thermal properties required by SP systems, which is extensively used in the aerospace, automotive and marine industries. The structural behaviors of polymeric materials are normally temperature-dependent and the deterioration of the structural strength with hot oil passing the SP should be considered. Several stress-strain curves of PP under

different temperatures are shown in Figure 2.1. Since the maximum strain during the installation process is relatively small compared to the yield strain of polymeric materials, the polymer-based core layer is usually modeled as a fully elastic, or hyperplastic incompressible material by Ogden model [17], in which the material coefficients should be calibrated by the measured stress-strain data.

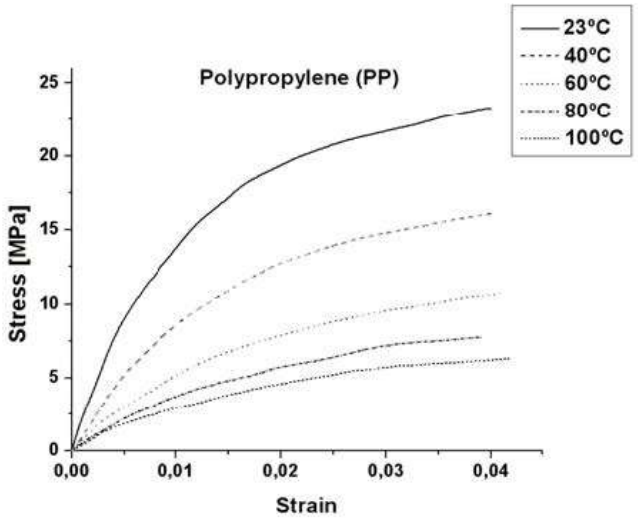

Figure 2.1: Stress-strain curves of the PP under different temperatures (adapted from [15])

Because of the low ductility, plain cement is not the best choice for the SP core layer as the whole system undergoes relatively large strain during the installation process. To overcome the tensile ductility problem, An et al. introduced the steel fiber reinforced concrete (SFRC) [18] and the SHCC [19] to the cement-based core materials. With the ability of the steel fibers to hold the cement together after appearing of the first crack, SFRC is proven to have superior resistance to cracking and crack propagation under flexural loading [20]. The SFRC demonstrates a strain-softening constitutive law which can be simulated by Concrete Damage Plasticity (CDP) model. The SHCC, on the other hand, displays strain-hardening behavior and multiple fine cracking characteristics, which allow for large energy absorption. The ultimate tensile strain of the SHCC can reach around 4% under monotonic load [21]. According to An et al. [19], the SHCC is one of the composite family of engineered cementitious composites (ECC). Figure 2.2 illustrates a typical stress-strain curve of the ECC with strain-hardening behavior, in which the ultimate strain of the ECC is expanded by ten times of the plain concrete. In the previous researches, the SHCC plasticity behavior was simulated by the CDP model [19], or the Druker-Prager (DP) model [22].

Table 2.1 summarizes the properties of all the proposed core materials of SPs.

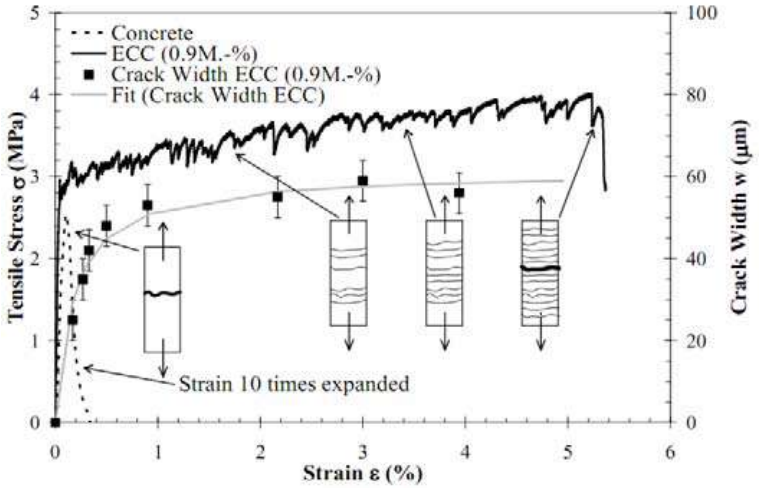

Figure 2.2: Stress-strain curves of the ECC and plain concrete under uniaxial tensile test (adapted from [23])

Table 2.1: Properties of the proposed core materials of SPs (collected from [6, 7, 16, 18, 23])

Category	Material	Density (kg/m^3)	Tensile strength (Mpa)	Tensile strain (%)	Elastic modulus (MPa)	Thermal conductivity (W/mK)	T_{max} (℃)
Polymer-based material	PP	900	23	8	1000	0.2	145
	PEEK	646	68	4	2331	0.18	348
	PC	679	44	5	2599	0.22	188
	ESF	720	22	8.5	1580	0.12	177
	HDPF	500	26	9.1	521	0.066	300
Cement-based material	Plain cement	2200	2.89	0.024	12280	0.67	-
	SFRC	-	2.79	0.75	37673	-	-
	SHCC	1473	4.5	4.5	11410	0.28	-
Note: T_{max} is the maximum service temperature.							

Although several core materials were proposed previously, only the mechanical performances of SPs with SHCC, PP or cement cores were experimentally investigated by previous researchers [6, 19], see Figure 2.3. Thus, most of the related researches focused on SPs with SHCC or PP cores.

In addition to all the existing SP core materials, the phase change material (PCM) incorporated with the cementitious composite can be a promising candidate. Previous researchers paid more attention to the mechanical performance than the thermal insulation performance. In most of the researches, only the thermal conductivity, which decides the SP insulation performance in the steady-state con-

Figure 2.3: Sandwich pipes with different core materials: (a) PP core; (b) cement core; (c) collapsed SP with PP core; (b) SP with SHCC core (adapted from [19])

dition, was included when selecting the SP core material. However, the thermal analyses conducted in chapter 4 show that the thermal energy storage capacity of the core material has a dominant impact on the SP insulation performance in the shut-in condition. Further, the results in chapter 5 also indicate that improving the energy storage capacity of the core material would improve the overall performance of SP by allowing a more balanced SP design. Thus, aiming at indicating the promising direction, relevant studies on the materials combining the PCM and cementitious composites are included in this section.

The PCMs possess large energy storage capacity due to the endothermic/exothermic energy transfer during the solid-liquid phase transformation [24]. Thus, the application of PCMs to delay and decay of indoor temperature fluctuations has drawn substantial attention in areas of residential buildings [25, 26]. To date, the organic paraffin is considered to be a promising candidate due to its inherent merits of large volumetric heat capacity (VHC), little or no phase segregation, chemical inertness and compatibility with most construction materials [27]. Since the pure paraffin cannot be directly employed into construction materials due to leakage problems, PCMs are often impregnated into porous granular materials. In this way, PCM is retained in the porous pace by capillary force and surface ten-

sion, thus preventing the leakage. Typically used porous materials are expanded perlite [28], recycled brick aggregates [29], and porous clay minerals [30]. After the impregnation, the PCM composites are incorporated into cement to form the PCM incorporated cementitious composite, Figure 2.4.

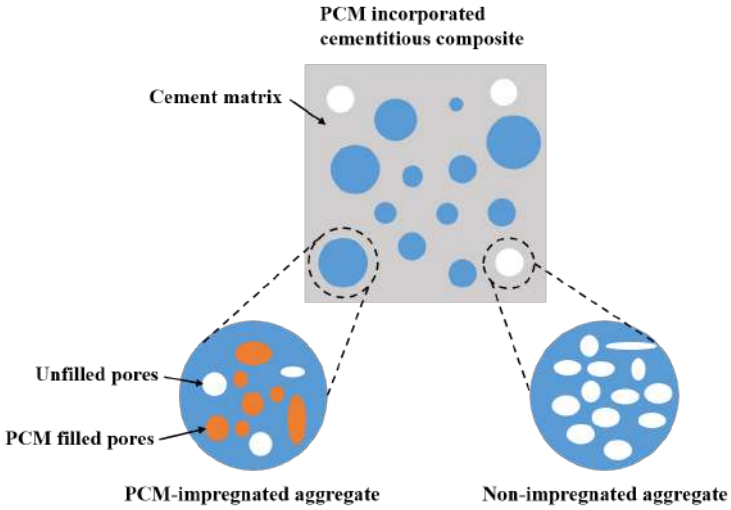

Figure 2.4: Illustration of PCM incorporated cementitious composite

According to the study by Ramakrishnan et al. [28], the composite PCM fabricated on paraffin/hydrophobic expanded perlite (EPO) showed an apparent density and 28-day compressive strength of 1244.2 kg/m^3 and 17.9 MPa respectively, when integrated into ordinary cementitious composite at 80% volume replacement of fine aggregate. It was reported that the PCM composite could reduce the peak indoor temperature by up to 2.8 ℃ and 4.43 ℃ in summer. Mankel et al. [29] experimentally investigated the mechanical and thermal performance of PCM integrated recycled brick aggregates (PCM-RBA) and concluded that the material is efficient in thermal energy storage. A heat storage capacity of around 26 MJ/m^3K was achieved in the temperature range of 18–28 ℃. Meanwhile, PCM- RBA lost 25% of the flexural strength and 27% of the compressive strength compared to the reference mortar without the PCM.

The construction materials used in residential buildings share the same necessities, which are structural strength and thermal insulation, with the SP core layer materials. Thus, the PCM integrated cementitious composite, which is widely investigated in the construction and building area, can be a promising material for the SP core layer. The investigation in Section 4.1 indicates that a higher heat storage capacity of the SP is critical for a qualified insulation performance in the shut-in condition. The VHC of the current SP core materials like SHCC and PP are 1.29 and 1.44 MJ/m^3, respectively. The employment of the PCM integrated cementitious composite like PCM-RBA can increase the VHC by nearly 20 times

of the SP with existing core materials. Meanwhile, no significant loss of structural strength caused by adding PCM to the cement composite was reported.

To conclude, the PCM incorporated cementitious composite can be a promising SP core material, providing good thermal insulation and adequate structural strength. However, impacts on the cost, submerged-weight, mechanical performance of the SP caused by the application of PCM composite should be investigated.

2.2 SP collapse under external hydrostatic pressure

In ultra-deep water scenarios (beyond 1,500 m), the extremely high hydrostatic pressure may cause the collapse failure of the subsea pipeline which makes the external pressure capacity of the SP systems essential to the design process. The SP system should be designed as an integrated system since all three layers contribute to structural strength. Also, the behavior of the SP system under external pressure can be complicated as it is influenced by many factors like the material and geometric properties of each layer and the inter-layer adhesion conditions. The optimized design of the SP system can only be achieved with a full understanding of the mechanical behavior of such a system and an accurate prediction of the external pressure capacity. Therefore, considerable attention has been paid to this topic during the past few years. The methods applied by previous researchers to study the collapse pressure of the SP can be classified into four categories: 1) Analytical or semi-analytical solution; 2) Experiments; 3) Numerical simulation; 4) Empirical equation.

2.2.1 Analytical solutions

The analytical solution can provide a quick estimation on the collapse pressure of the SP as well as a physical understanding of the collapse mechanism. Assuming a perfect bounded inter-layer relation, Sato and Patel [31] developed an analytical solution for the elastic buckling of SPs. The variational principle of minimum potential energy was applied to build the equilibrium equation of the SP system. The smart solution from their method was to express the strain energy of the core layer as the work done by the internal and external steel layers at the interface. However, the analytical solution was proposed without enough details, and the presented equations include some typing errors. As the solution includes several typical theories in solving the SP elastic collapse pressure, their analytical solution is redeveloped with details and presented in appendix A. Based on Sato's work [31], Arjomandi and Taheri [32] developed a similar analytical solution for SP considering four kinds

of inter-layer relations: a) Core layer is fully bonded to the inner and outer layer; b) outer layer is bonded to the core while the inner layer is free to slide in the tangential direction; c) Inner layer is bonded to the core while the outer layer is free to slide in the tangential direction; d) Core can slide freely against both layers. In the solutions developed in the two previous papers, the Sander's equation (shell theory) was applied to the kinematic relation for inner and outer pipe and linear kinematic relation was applied to the core layer. Thus, radial and shear strains in the inner and outer pipes and non-linear strain in the core layer were neglected for simplicity. In order to capture the non-linear strain effect, Hashemian [33, 34] applied a more complex kinematic relation for all layers and developed an eigenvalue buckling solution for the SP. The equations that dominate the buckling phenomenon were obtained by setting the second variation calculus of the total potential energy of the SP to zero. Due to the complexity of the equations, buckling pressure had to be calculated by numerical methods. Based on a stress function method and assuming a perfect bounded inter-layer relation, Jin et al. [35] proposed a three-dimensional analytical model to determine the stress and displacement of SP systems subjected to linearly varying external pressure. Xue et al. [36] developed a first-order shear deformation theory for SPs under external pressure by considering the initial curvatures in the circumferential direction. A bifurcation study on the elastic collapse was conducted. More recently, Ghahfarokhi and Rahimi [37] proposed an analytical approach for SPs with the iso-grid core. By transforming the sandwich pipe with iso-grid core into a single-walled pipe, the critical buckling pressure was solved by Rayleigh–Ritz energy method.

To date, most analytical solutions can only provide elastic collapse pressure of the SP. However, for some SP configurations, plastic buckling could happen where the stress of the partial or whole material pertaining to the plastic region when buckling occurs. The analytical solution may not provide an accurate collapse pressure when the SP configuration has a plastic buckling. Further, due to the natural complexity of the problem, there was a tradeoff between accuracy and simplicity for the previous analytical solutions. To reduce the complexity of the equilibrium equation, the above-mentioned analytical solutions inevitably rely on certain simplifications like assuming perfect geometry, neglecting the material plasticity, applying the shell theory, idealizing the interlayer adhesion, and so on. These assumptions can make the estimation deviate from reality in some SP configurations. The applicability of the analytical solution presented in appendix A is discussed in section 3.2.1.

2.2.2 Experiments

Most experimental research on the collapse pressure of sandwich pipes has been conducted at the Subsea Technology Laboratory at COPPE – Federal University of Rio de Janeiro. Estefen et al. [6] conducted eight small-scale collapse experiments on an SP composed of two aluminum tubes separated by a cement or polypropylene (PP) core. The researchers applied a calibrated finite element model for the strength analyses of the SP under external pressure and longitudinal bending. Using the same materials (Aluminum and PP), Souza [38] carried out collapse experiments on an SP with silicon grease in the interface layer. Focusing on the inter-layer adhesion behavior, Castello et al. [39] proposed six experiments on SPs composed of steel tubes and PP cores. An et al. [19] conducted a full-scale laboratory test to analyze the collapse pressure of SPs with SHCC cores (SHCC SP). The preparation of the SHCC material and the whole collapse experiment process were explained with details. With the experimental results, the researchers proposed a proper numerical model for the collapse simulation.

Until now, a limited number of experiments on the collapse pressure of SPs can be found in the literature. The previous experimental researches focused on SPs with SHCC, PP, and cement cores. In general, the collapse pressure of an SP can be experimentally obtained by the following process. The SP prototypes are put inside a hyperbaric chamber (Figure 2.5) with welded lids to close the ends. Then, the hyperbaric chamber is filled with water. The pressure is increased by pumping water into the chamber. The experiments are concluded when a sudden drop of pressure occurred, which implied the collapse of the SP prototype. Figure 2.6 shows an intact SP before the test and a collapsed SP afterward.

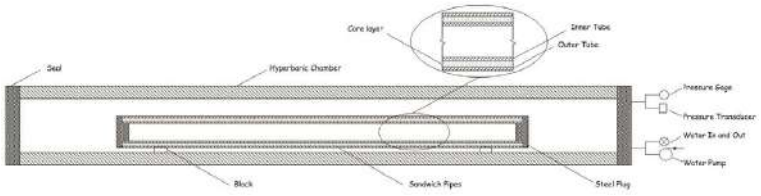

Figure 2.5: Sketch of the hyperbaric chamber for the SP collapse experiment (adapted from [23])

2.2.3 Numerical simulations

Experiments are usually considered the most accurate method to discover the collapse pressure of an SP system. However, the experimental approach is impractical for a large-scale parametric study. Numerical simulation is more suitable for studies focusing on several SP configurations. By setting different maximum shear

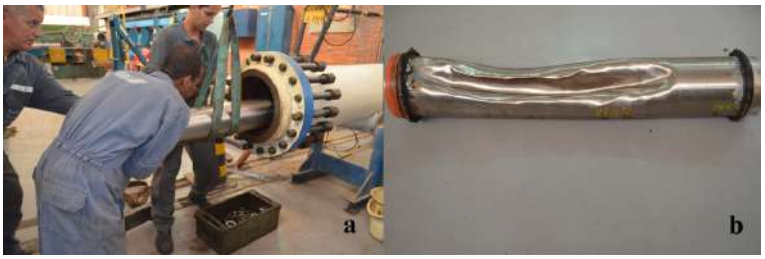

Figure 2.6: Collapse experiment:(a) Putting the intact sample in the pressure vessel; (b) Collapsed sample

stresses for inter-layer adhesion, Castello [40, 41] numerically investigated the ultimate strength under external pressure and the bending moment of an SP with a PP core. Later, Castello [9] extended the previous research by including the thermal insulation performance of the SP and concluded that, with proper core materials, SPs could generate significant advantages in deep-water applications. An et al. [18, 42] conducted numerical analyses on the ultimate strength of an SP filled with strain-hardening cementitious composite (SHCC) under external pressure and at the bending moment. The researchers produced pressure curvature failure envelopes for SPs with different interface conditions. By building a 2D model, Fu et al. [22] numerically studied the effect of initial imperfections on the collapse pressure of an SP filled with SHCC. With proper modeling, collapse mechanisms and post-buckling behavior can be investigated by parametric studies. Assuming a full elastic core and perfect inter-layer bonding, Arjomandi and Taheri [10] investigated the behavior of SPs with 3840 practical configurations subjected to external pressure. In their later study [43, 44], this parametric study was further developed by considering four different inter-layer adhesions for SPs. He et al. [45] numerically studied the effects of different inter-layer adhesion strengths, relative angles between the main axis of the inner and outer pipes, and geometrical and steel properties on the collapse pressure of SPs with PP cores. Several pieces of research [5, 6, 8, 9, 22, 41, 44] reported that the inter-layer adhesion has a significant impact on the structural performance of SPs. Xu et al.[46] dedicated investigations to the collapse pressure of SPs with PP cores under different inter-layer adhesion strength. The stick-slip levels of two different adhesives in steel pipes were experimentally evaluated. Recently, Fernández-Valdés et al. [47] established a full ring 2D model for the collapse analysis of SPs with cement core and PP core in the ANSYS software. The researchers investigated the effects of different initial imperfections and inter-layer friction behaviors on the collapse pressure of SPs subjected to external hydrostatic pressure, where different inter-layer friction behaviors were modeled using the Coulomb friction model and different friction coefficients.

The finite element (FE) model established in the software ABAQUS [48] was

widely used to investigate the collapse behavior of SP under external pressure numerically. Table 2.2 summarizes the numerical models for SPs with different core material by previous researchers. As shown, with a proper numerical model, the numerical simulation can accurately predict the collapse pressure of the SP subjected to external pressure. For the SP with PP core, the numerical model with the fully bonded inter-layer condition predicts more accurately than the model with the frictionless inter-layer condition. For the SP with SHCC or cement core, the model with the frictionless inter-layer condition gives a more accurate prediction. Since only the experimental results of SPs with PP, cement, and SHCC cores are available in the literature, most of the numerical studies focused on SPs with these core materials. To date, there has been no comprehensive study on the collapse pressure and post-buckling behavior of SPs with SHCC cores.

Table 2.2: Numerical models for SPs by previous researchers

Researcher	Core material	Type of elements	Model features	Steel layer model	Core layer model	Interface model	P_{co}*	P_{co}**	P_{co}***
Estefen et al.[6]	PP	CPE8	2-D Quarter ring	J2 flow associated with isotropic hardening and von Mises criteria	Hyperelatstic, incompressive by Ogden model	Fully bonded or frictionless	30.3	9.6	26.6
	cement				Simplified associative flow rule with isotropic hardening		35.4	23.5	25.1
An et al. [19]	SHCC	C3D8R	2-D Quarter ring		Concrete damaged plasticity model	Fully bonded or frictionless	35.7	31.9	30.3
Fu et al. [22]	SHCC	CPEG8R	2-D Quarter ring		Drucker prager model	Frictionless	-	27.8	30.3
Xu et al. [46]	PP	Steel: C3D27; PP: C3D27H	2-D half ring		Hyperelatstic, incompressive by Ogden model	Non-linear axial springs	-	-	-
Arjomandi et al. [10]	Polymeric material	C3D20R	2-D Full ring	Elastic perfecly plastic	Pure elastic model	Fully bonded	-	-	-
He et al. [45]	PP	Steel: CPE8R; PP: CPE8H	2-D Full ring	Exponentially hardening by Ramberg–Osgood law	Hyperelatstic, incompressive by Ogden model	Isotropic coulomb friction model	-	-	-

Note: P_{co}* and P_{co}** are the numerically predicted collapse pressure with fully bonded and frictionless inter-layer conditions, and P_{co}*** is the experimental collapse pressure.

2.2.4 Empirical equations

For the conceptual design of SPs, a quick and accurate prediction of the collapse pressure of different SP systems is required. Intending to achieve both speed and accuracy of the estimation, researchers have proposed several empirical equations. Based on their analytical solution, Sato and Patel [31] proposed a simplified equation for the collapse pressure of SPs, assuming that the core material fills the entire inner space of the outer pipe. Arjomandi and Taheri [32] improved the accuracy of Sato's equation by including more effective structural parameters. With a large amount of data calculated by their semi-analytical solution, Hashemian [33] also proposed an empirical equation applying the regression method. He et al. [45] numerically studied the effect of different inter-layer adhesion strengths, the relative angle between the main axis of the inner and outer pipes, and geometrical and steel properties on the pressure capacity of SPs with polypropylene (PP) as the core material. Based on a large amount of simulation data, the empirical equation can fit the finite element (FE) results within a maximum error of 19.58%. Using practical SP configurations and three different Young's modulus core materials (representing a soft, moderate and hard core), Arjomandi and Taheri [10] proposed an equation for fully bonded SPs based on more than 3000 FE simulation results. In a later work [43], They described two categories of post-buckling behaviour, claiming that the overall stiffness of some SP configurations could still increase after a threshold pressure in which the plasticity response dominates the behaviour. Further, with 768 FE simulation results for each inter-layer adhesion, empirical equations were proposed for SPs with four different conditions for the inter-layer adhesion. Later, Arjomandi and Taheri [44] expanded the FE simulation results to more than 12,000 in total and proposed 12 empirical equations for the prediction of the SP pressure capacity.

Generally, there are two types of empirical equations. First, empirical equations proposed from the simplification of the analytical solution, as in the works of Sato and Patel [31] and Arjomandi and Taheri [32]. Since the analytical solution is unable to achieve adequate accuracy for various configurations of SP systems, the simplified empirical equation obtained from the analytical solution usually performs worse, as observed by Arjomandi and Taheri [10]. Second, empirical equations acquired by regression methods from a large amount of data from numerical simulations [10, 33, 43–45, 49]. The regression equation seems to be a promising solution for a quick and accurate prediction of the SP collapse pressure.

2.3 Installation of SPs

There are several methods to install a subsea pipeline, among which the S-lay, J-lay, and Reeling-lay are the most common methods. The traditional method for subsea pipeline installation in relatively shallow water is referred as the S-lay method, shown in Figure 2.7. The pipe segment between the seabed and the stinger forms an elongated S shape during the installation. The stinger on the vessel is a structure that supports the pipe through the transition from the horizontal position to the inclined suspended shape. The pipe segment would be bent twice before it reaches the seabed. The upper curved part is called the overbend. In this position, the pipe is mainly subject to bending and tension. After that, the pipe continues in a quasi-straight line under tension and hydrostatic pressure, until it bends gradually in the opposite direction to lay on the seabed. The second curved part is called sagbend. When the depth of seabed increases, the suspended length of the pipe will also increase; this induces additional tension in the pipe.

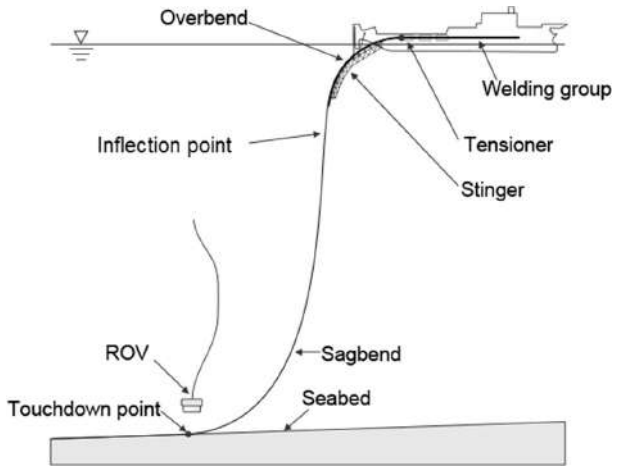

Figure 2.7: S-lay installation (adapted from [50])

In extremely deep water, the departure angle of the pipe, in an S-lay installation, becomes so steep that the required stinger length may not be feasible. Under this circumstance, the J-lay method was invented for deepwater subsea pipelines. Similar to S-lay, the name J-lay is given because of the configuration of the pipe resembling a J shape during installation, see Figure 2.8. Line pipes are joined to each other by welding in a vertical or near vertical welding station. As more and more line pipes are connected together, a string is formed and lowered onto the subsea floor. Hence, the J-lay method is inherently slower than the S-lay method and is, therefore, more costly.

In both S-lay and J-lay installation, the pipeline segments are connected by welding on the lay barge. The offshore welding increases the operational time of the lay barge, and thus, increases the installation cost. The reeling-lay is a pipe

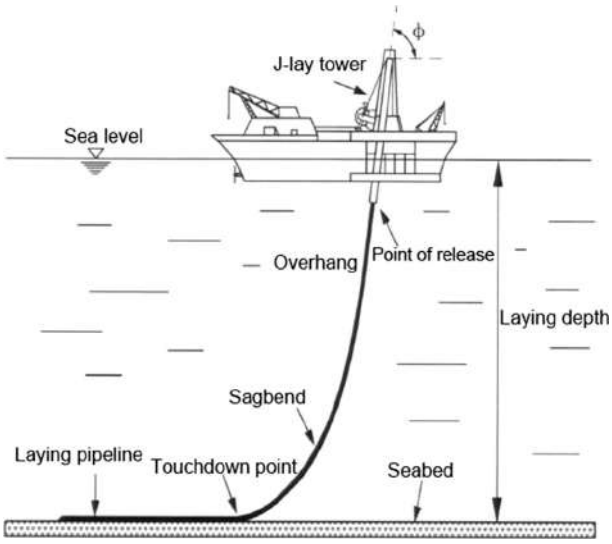

Figure 2.8: J-lay installation (adapted from [50])

laying method emerging in the late 20th century (Figure 2.9). With reeling-lay, the pipe segments can be welded together on land to a great length, then reel up to a drum mounted on a reel laying vessel. Subsequently, the pipe is unreeled and straightened at the offshore site before launching it to the seabed (Figure 2.10). Reeling, unreeling, and straightening involve plastic strains and variations in both cross-sectional ovalities and residual strains, which may have a detrimental effect on the ultimate strength of the pipeline. For a particular drum, the maximum residual strain and the ovality induced by reeling-lay are proportional to the outmost diameter of the pipeline. Estefen et al. [51] conducted numerical and experimental simulations to evaluate the reeling-lay effect on the collapse pressure of the SW. The researcher found that the collapse pressure decreased substantially with the increase of the pipeline diameter. Usually, depending on the wall thickness, the maximum allowed diameter for the reeling-lay is around 18 inches. Also, due to the limited size of the drum, only short lengths of pipe can be laid (usually 3–15 km depending on pipe diameter). However, it is possible to install longer pipelines if more drums of pipe are available.

Comparing to the conventional SW, the welding process for SP segments consumes significantly more time since the connection should be conducted for several layers. Thus, the S-lay and J-lay methods with offshore welding are not practical for the SP since the long offshore welding time duration could substantially increase the installation cost. The reeling-lay is considered a preferred installation method since it can reduce the installation cost for the SP by eliminating the offshore welding time. Castello et al. [41] numerically investigated the effect of the reeling-lay process on the collapse pressure of a PP SP with an utmost diameter of $8\frac{5}{8}$ inches. The results show that the reeling-lay process caused a small reduction of the collapse

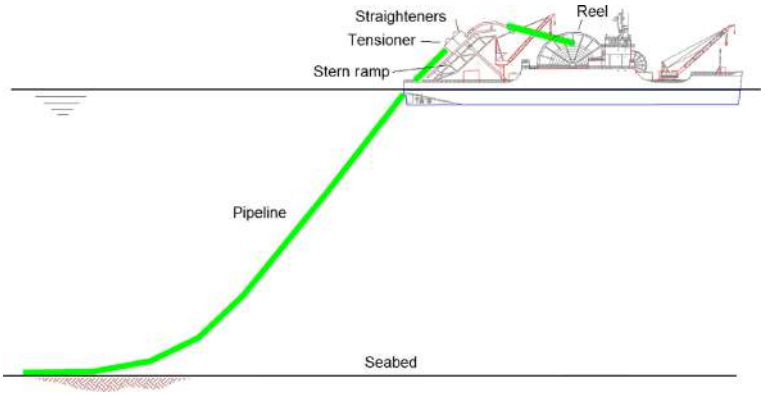

Figure 2.9: Reeling-lay installation (adapted from [50])

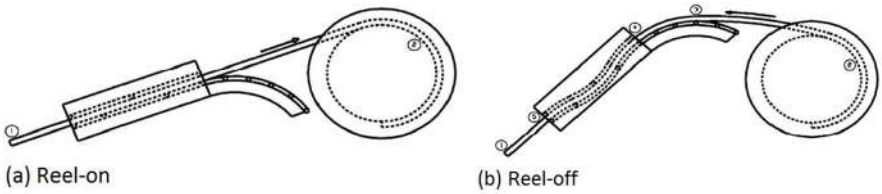

Figure 2.10: Reeling process scheme

pressure (1.4%). Later, Fu et al. [22] established a numerical model to investigate the behavior of an SHCC SP in the whole bending and straighten process. Subsequently, Paz et al. [52] experimentally evaluated the detrimental effects of reeling-lay on the collapse pressure of SHCC SPs with an utmost diameter around 8 inches. One of the two specimens was submitted to the bending on the rigid surface of a reeling-lay simulation apparatus, and the other specimen was kept intact before the collapse test. Their results suggested that the negative influence of the reeling-lay installation to the collapse pressure of the tested specimens can be neglected.

For the installation of an SP with a large diameter, the reeling-lay is not suitable, and the S-lay or J-lay is required. In this situation, employing an SP connector is a practical way for the connection of SP segments. Quispe, J. L. P. [53] proposed an SP joint using the threaded connection (Figure 2.11) and carried out numerical analysis under different make-up torque, axial load, and the combined load of bending and external pressure. The connector design paid special attention to manufacture aspects, installation, and operation issues. The joint was focused on metal-to-metal seal through the contact of metal surfaces. Onyegiri and Kashtalyan [54–57] conducted several studies on joining methods for SP segments. First, the mechanical response of a swaged field joint connecting SP segments with different geometric properties was studied [54]. Later, they numerically investigated the use of a snap-fit connector [55] for SP installation. Regions susceptible to high stress concentration under combined loads were identified. In the companion paper [56], an optimization study on the stress relief groove in the pin of the snap-fit connec-

tor was carried out. The relation between the geometric properties and the stress concentration factor at the stress relief groove was discussed. Finally, they evaluate the performance of swaged weld for SPs during J-lay installation [57].

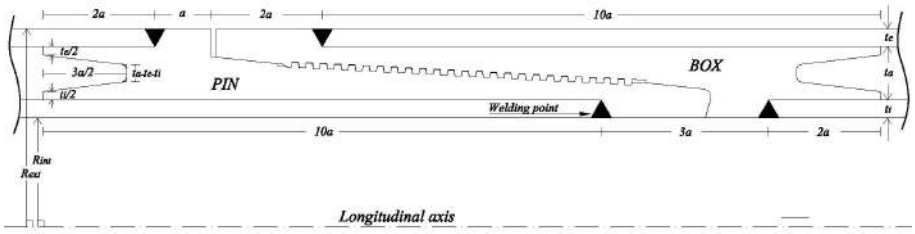

Figure 2.11: Threaded SP connector by Quispe et al.[53]

2.4 Thermal insulation of SPs

2.4.1 Thermal management of subsea pipelines

Flow assurance is one of the most important design issues for offshore pipelines in deepwater, which usually does not arise in shallow water where water temperatures are higher and hydrostatic pressures are lower. The term Flow Assurance was proposed by Petrobras in the early 1990s. In general, flow assurance includes all issues important for ensuring the flow of produced fluid from the reservoir to reception facilities [58]. When oil, gas, and water are flowing simultaneously inside a deepwater pipeline, several problems may arise [59]:

- Water and hydrocarbon fluids can form hydrates and block the pipeline.
- Wax and asphaltene can deposit on the wall of the pipeline and reduce and/or block the flow.
- Corrosion may occur if water cuts are high and/or impurities exist in the hydrocarbon fluids.
- Scales may form due to pressure and temperature changes along the pipeline or from incompatible crude mixing.
- Slugging may occur and cause operational problems.

Among the flow assurance issues, wax and hydrate formations are mainly influenced by the fluid temperature, which dictates the requirements for the pipeline insulation system. A schematic of an oil phase diagram shows the possibilities as the oil follows a path along a steadily decreasing temperature and pressure as it moves from the reservoir into the wellhead and flowline (Figure 2.12). In deepwater

fields, depressurization can not mitigate the hydrate problem since the hydrostatic pressure at the seabed is high enough to form the hydrate. Thus, controlling the fluid temperature to avoid hydrate and wax is one of the main challenges of flow assurance.

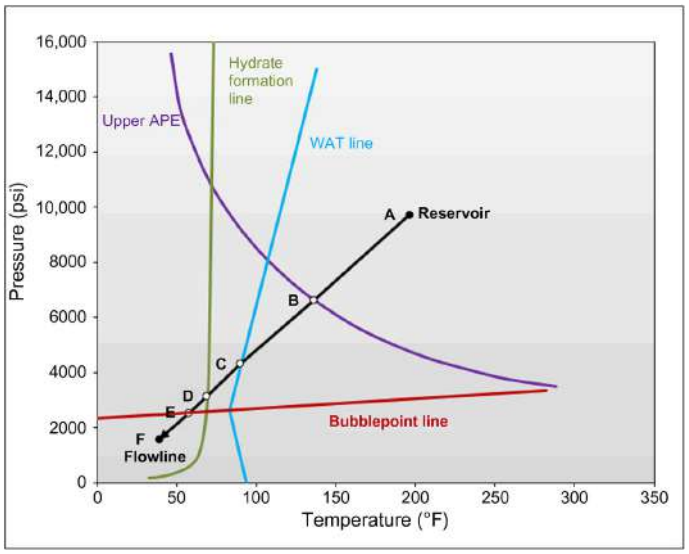

Figure 2.12: Schematic of temperature and pressure condition from reservoir to flowline (adapted from [59])

Su [58] comprehensively reviewed the challenging engineering problems, corresponding understandings, and solutions concerning flow assurance, which include topics such as flow regime transition, pressure gradient, liquid holdup, slugging, simulation of transient flow, thermal insulation, active hearting, and modeling of wax deposition. The author classified the passive insulation systems as integral external insulation, multilayer insulation, insulation modules, PIP system, and bundle insulation. All the insulation systems employ materials with low heat conductivity to prevent heat transfer from the produced fluid to the seawater. Normally, the insulation materials are polymeric such as polypropylene, polyurethane, and epoxies. According to Grealish et al. [60], these insulation materials come in four main forms as solid, blow foam, syntactic, and composite syntactic. Blown foam materials offer good insulation properties but have limited water depth if unprotected. Syntactic and composite syntactic foams offer good water depth capability as well as good insulation and hydrostatic strength properties. Solid materials have the best depth capability but have less favorable insulating properties. Collins [61] summarized and evaluated the offshore insulation materials from the aspects of design, manufacture, performance and deformation during reeling. Using experimental results, Gac et al. [62] developed a mathematic model, coupling thermal gradient, water absorption, and hydrolysis kinetics, to predict the degradation of polyurethane as offshore insulation material. In addition to traditional insulation materials, insulation sys-

tems incorporating phase change materials (PCM) also have drawn attention. In the steady-state working condition, the PCM absorbs heat from the produced fluid and remains in the liquid state, acting as a heat accumulator. During the shut-in condition, the crystallization of the PCM releases partially the stored heat back to the fluid. Thus, such an insulation system produces considerable thermal inertia delaying the hydrate formation [63]. Alawhadhi [64] numerically evaluated the insulation performance of pipe with PCM materials, where the PCM layer is located at the inner surface of the insulation layer. The results indicate that the insulation with PCM is an effective thermal barrier in reducing the heat loss for a significant amount of time. Wang et al. [65] developed a pseudo-3D mathematical model to investigate the thermal behavior of a long-distance pipe insulated by multilayers with micro PCM particles, where the PCM particle is embedded in a polymeric matrix. They concluded that it is foreseeable that incorporating micro PCM particles into the composite layer can potentially prolong the cool-down time as demanded by the oil and gas industry for pipeline intervention.

When the passive insulation systems are not sufficient to meet the severe thermal insulation requirements, active heating is required. Heated flowlines can significantly reduce the complexity of shutdown and start-up operations, and provide better overall flow assurance. Two methods of active heating of deepwater pipelines have been studied: electrical heating and heating by a circulating heat medium. Su et al. [66] presented a global heat balance analysis of a subsea pipeline with active heating and passive insulation system. Both active heating systems by circulating hot water and electrical resistance were considered. An optimum heating strategy for long-distance pipelines was proposed, which reduces the power requirement considerably. Subsequently, Su et al. [67] conducted a steady heat transfer analysis on the SP with electrical heating, where the fluid temperature distribution was calculated by a 2D heat transfer model. Nysveen et al. [68] evaluated several electrical heating methods by numerical studies. Further, some operational experience of active heating was summarized, which gives an important guide for the electrical heating application. More recently, Verdeil et al. [69] proposed a generic solution to overcome the high voltage requirement and the high energy loss in the power cable for remote tie-backs by optimizing pipeline cross-sections and field architecture.

For the subsea pipeline with active heating technology, the passive insulation system is necessary to improve the heating efficiency. Thus, a passive insulation system is almost mandatory for the subsea pipeline in deepwater applications.

2.4.2 Heat conduction in multilayer structuress

The SP system is a kind of passive insulation system with several variations. Different core materials could be employed with specific thermal insulation requirements. Further, an extra insulation layer with different insulation material can be applied outside of the outer steel pipe to meet high thermal insulation requirements. For an SP working normally on the seabed, the temperature of the external fluid (seawater) may be lower than 4 ℃, and the internal fluid (oil and gas) may reach 90 ℃. It is a typical heat conduction problem in multilayer cylinders, including steady and transient states.

Castello et al. [9] compared SPs with different core layer materials that provide the same maximum overall heat transfer coefficient (U-value). The U-value method is an efficient and simplified way to evaluate the insulation capacity of a subsea pipeline in the steady-state working condition. However, it is not able to indicate the insulation capacity in the shut-in (transient) working condition. Estefen et al. [70] conducted steady-state simulations with the OLGA software of the application of SPs for long-distance gas transportation, where the pressure and temperature curve of the pipeline was compared with the hydrate formation curve. The insulation capacity of the SP was compared with the SW and the PIP, and the SP showed superior insulation over the SW while the PIP gives the best insulation performance. Escobedo et al. [71] developed a transient analysis model by coupling the fluid flow conservation equations and the heat conduction equations of the pipe wall. A good correlation between their model and the OLGA software was achieved. The authors conclude that it is essential to account for the thermal capacity of the wall layers that compose the pipeline since they significantly influence the cool-down time. Su et al. [72] developed a mathematical model for transient heat transfer analysis of a multilayer pipeline. An improved lumped-differential formulation was proposed for the solution of the transient heat conduction equation in composite media. Later, Su et al. [73] developed mathematical models governing the heat conduction in the multilayered pipe and the energy transport in the produced fluid. With the developed models, the simulations of the cool-down process of SPs in three configurations, as well as SPs with direct electrical heating, were carried out. An and Su [74] developed improved lumped parameter models for the transient heat conduction in multilayer composite slabs subjected to combined convective and radiative cooling. The improved lumped models were obtained through two-point Hermite polynomial approximations for integrals. Transient combined convective and radiative cooling of three-layer composite slabs was analyzed to illustrate the applicability of the proposed lumped models, with respect to different values of the Biot numbers, the radiation-conduction parameter, the dimensionless thermal contact resistances, the

dimensionless thickness, and the dimensionless thermal conductivity. The method was also applied to analyze the transient heat conduction problem of steel-concrete-steel sandwich plates. Kayhani et al. [75] presented a steady analytical solution for heat conduction in a cylindrical multilayer composite laminate. The problems with various conditions, including combinations of thermal conduction, convection, and radiation, can be solved using the analytical solution. The Sturm-Liouville theorem was used to derive an appropriate Fourier transformation, which was solved by the recursive Thomas algorithm.

2.5 Optimum design methods of subsea pipelines

The design of a subsea pipeline involves the determination of wall thickness, insulation thickness, pipeline diameter, and the corresponding material. The pipeline diameter is mainly decided by the flow velocity of the produced fluid, which is a predetermined parameter for the mechanical strength and insulation capacity of the pipeline. Thus, the following literature review concentrated on the researches related to the determination of the thickness and material for the subsea pipeline.

2.5.1 Thermal insulation requirements and insulation thickness

For a specific application, the thermal insulation requirements are the guidelines in the selection of insulation material, thickness, and pipeline type. According to the experience of the Brazilian offshore industry [2, 3], the insulation system should keep the fluid temperature above a particular value, like the wax appearance temperature (WAT), in the steady-state working condition. And the insulation system should be able to provide 2 to 8 hours of cool-down time (defined as the time needed by the coldest point of the flowline to enter into hydrate formation zone). According to Hazirah [76], the maintenance process, the operative procedures to bring the system outside the hydrate formation zone forever, may take more than 6 hours. Therefore, 8 to 12 hours of cool-down time is necessary for a qualified insulation system. Dwight [77] also claims that the operators typically requires 8 to 12 hours of temperature levels above hydrate formation temperature during the shut-in operation. In these studies [78–80], the thermal insulation requirements are simplified as a required U-value of the pipeline, which only considered the insulation for the steady-state condition.

A cost-effective insulation system is of great importance for subsea applications. Insulation optimization is a hot spot in the district heating area where hot water or steam circulation in pipelines is applied to warm residential buildings. There are

several works to optimize the pipe insulation [81–88]. For a district heating system, the temperature of the pipeline is governed by the amount of fuels used to generate thermal energy, which makes the temperature of the pipeline independent of the insulation thickness [82]. The main goal of these researches, towards insulation optimization, is to wisely balance the fuel cost and the insulation cost (see Figure 2.13). In contrast, offshore heating systems are usually an expensive choice and the temperature of offshore flowlines and pipelines is highly dependent on the insulation thickness. However, despite the extensive use of insulation in the offshore industry, researches on insulation optimization are not frequent.

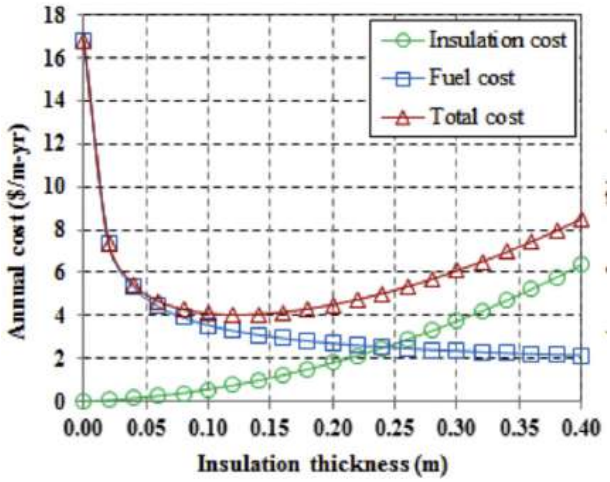

Figure 2.13: Cost and insulation thickness (adapted from [82])

Chin and Bomba [89] developed a structural and thermal optimization design method for cased insulated flowline configurations, including pipe-in-pipe and non-steel synthetic jacket insulated flowlines. The pipeline installation process is sensitive to the diameter to thickness ratio and submerged weight of the cased pipeline. In their approach, a design map for pipe configuration was developed considering the required U-value and the constraint from installation. Haoran and Yongtu [90] proposed an optimal design method using an improved particle swarm optimizer (PSO) algorithm, which jointly considered insulation performance and structural integrity of subsea pipelines. Azevedo and Teixeira [80] introduced the design process of the insulation system for a deepwater field in Brazil. They used a required overall heat transfer coefficient to decide the insulation material and its thickness. Faluomi and Arcipreti [91] did a review of the insulation systems. By building a multiphase flow package, they used a single pipeline as a case study to evaluate different insulation systems, including passive and active systems. Hazirah [76] built a transient heat transfer model to calculate the temperature drop profile for the pipeline with multi-coating layers. Based on the model, the authors collected the thermal properties of several typical insulation materials and incorporated them into a software which

was used to compare the insulation performance of pipelines with different insulation configurations. However, no optimization method was applied in their study to determine the most economical insulation design. Pavel [92] proposed an optimization scheme combining Matlab and Ansys software applied to the insulation design of gate valves. The genetic algorithm was employed in their work.

For the subsea pipelines, the design of a thermal insulation layer is achieved by attending the corresponding thermal insulation requirements, which principally involves the minimum fluid temperature in steady-state condition and minimum cool-down time in the shut-in condition. Several pieces of research on the design of the insulation layer could be observed in the literature. However, no study on the optimal design of the SP insulation system is reported.

2.5.2 Structural requirements and wall thickness

The structural design of the offshore pipeline addresses the ability to withstand operating, testing, and installation stresses in the pipe as well as the ability of the pipeline system to withstand environmental forces. For a conventional SW, the current design practice is to limit the hoop stress for design against the differential pressure and to limit the equivalent stress for design against combined loads [93]. For single wall pipe design, the mechanical strength is required to meet the commonly used design codes: ASME B31 Codes, ISO Pipeline Code, API RP1111, and Classing Undersea Pipelines and Risers and DNV Pipeline Rules. The selection of material grade and wall thickness can be accomplished by the equations suggested in these codes. Based on the data of a full-scale test, Alexander [94] proposed a limit state design procedure which provides a legitimate basis for reducing safety factors while maintaining an adequate level of reliability. Wang [95] mainly considered the effect of hoop stress and equivalent stress on subsea pipeline design as well as others like thermal, pressure, soil friction restraint, and externally applied axial forces, and performed the calculation of unsupported span under static and dynamic situations. Considering the related uncertainty factors like inhibitor efficiency, Hasan [96] properly quantified the internal corrosion and consolidated the metal loss in a corrosion risk-based pipeline design method.

For the PIP system, the thickness of each layer is designed separately [13]. The carrier pipe is used to protect the inner pipe against the external hydrostatic pressure and is designed for failure modes associated with critical collapse, installation and trawl gear interaction while the inner pipe is designed for bursting and installation only [97]. In a compliant system, where continuous force transfer occurs between the inner pipe and outer pipe, the design should consider the axial and bending force that transfer between inner and outer pipe [98]. Sahota [99] discussed the design

detail of a PIP system incorporates a 10-inch production pipe insulated in a 16-inch carrier pipeline for a reservoir with high pressure and temperature. The analysis is conducted by the finite element method using the Abaqus software.

Similar to the design of the insulation layer, the structural layer of an SW or a PIP is designed with respect to the structural requirements involved in the deepwater application. As the conventional solution, the SW has comprehensive and standard design procedures defined in the above codes. The determination of the steel layers of a PIP can be carried out by separately applying the design codes on the carrier and inner pipes of the PIP. To date, the method to design the structural layers of an SP has been barely reported.

2.5.3 Machine learning and optimization algorithms

The optimization problems in the real industry are complicated by nature. Likewise, the optimization of the sandwich pipe combining structural and thermal analyses is a strong non-linear problem involving multiple variables and constraints, which is discussed in chapter 5. Optimization methods that require gradient information are prone to provide local optima instead of a global one [100]. Naturally inspired algorithm like genetic algorithm (GA) [101] and particle swarm optimization (PSO) [102] has a distinct advantage of avoiding local optima which is difficult for the gradient type method.

Genetic algorithm is one of the most popular methods widely used for optimization problems. Dao [103] found over one hundred thousand papers published related to GA which is inspired by Darwin's evolution theory. Lucena et al. [100] applied GA to the optimization of subsea pipeline routes, and different constraint handling methods are compared in their work. GA is also employed in [104] working with a commercial software to optimize the insulation of a residential building. For a certain problem, one potential solution is treated as an individual with its information coded in its chromosome. The evolution starts with an initialization algorithm which randomly generates a group of individuals. After initialization, one or several objective functions defining the problem are used to evaluate the fitness of each individual, taking into account the constraint function. Then the operation of selection begins. The fitness-proportional roulette wheel method is commonly used as the selecting operator. The fittest individuals have a higher probability of surviving and reproducing. In the reproducing process, the genes from parent individuals are combined and exchanged to produce descendants. A mutation may happen in the gene of the descendants to provide a better exploration of the search space. Then the next loop begins with the evaluation of the descendants. The GA algorithm terminates when the stopping criterion is reached. Usually, the criterion is simply

the maximum number of loops defined. When the algorithm ends, the individual with the best fitness is considered the optimized solution [105].

Particle swarm optimization (PSO) was introduced by Eberhart in 1995 [102]. It imitates the social behavior of birds to find the optimized solution. The algorithm involves communication between individuals and the memory of each individual. In the PSO, one possible solution to the optimization problem is treated as the position of each particle. Like the GA, the PSO starts with random initialization. The objective functions and constraints are used to evaluate the fitness of the particles. During iteration, each particle keeps track of its coordinates in hyperspace which are associated with the best solution (fitness) it has achieved so far. (The value of that fitness is also stored). This value is called personal best (pbest). Another "best" value is also tracked. The "global" version of the particle swarm optimizer keeps track of the overall best value, and its location, obtained by any particle in the population, called global best (gbest). The particle swarm optimization concept consists of, at each time step, changing the velocity (accelerating) each particle toward its pbest and gbest. Acceleration is weighted by a random term, with separate random numbers being generated for acceleration toward pbest and gbest. The algorithm ends when the maximum iterations number is reached, and the particle with the gbest is the optimized solution [106]. Due to its simplicity, PSO is also widely applied for engineering optimization [107, 108].

For the stochastic optimization algorithm like GA and PSO, it is inevitable to evaluate a large number of candidate solutions for each run. When the evaluation of each candidate solution is computationally expensive, each run of the optimization algorithm would be time-consuming or even impractical sometimes due to the heavy computational work. For the optimization of the SP, it is critical to have quick and accurate prediction methods of the structural strength and insulation capacity of a particular SP configuration. However, as discussed in previous sections, these predictions involve complex modeling with theories related to the physical background, which normally can not be quickly achieved. In this situation, Machine learning, with its outstanding ability to extract patterns from a large amount of data, can be a promising solution to overcome the challenge.

Depending on the data properties and the learning task to be performed, there are two classes of machine learning: supervised learning and unsupervised learning. Supervised learning is the case where both target y (also called response, outcome, e.g., house price) and features x (also called predictors, regressors, e.g., house size, location) are measured. And the goal is to find the pattern behind y and x, then use the trained pattern for further prediction. Normally, the pattern is established by minimizing the difference between the prediction value and the corresponding target value. If the target y is quantitative (e.g., price), the supervised learning

problem is further classified as a regression problem; if y is categorical (e.g., spam / legitimate), the problem is classified as a classification problem. For unsupervised learning, y is not provided in the data. The learning goal becomes fuzzy, usually to find groups of samples with similar behaviors. In this study, the objective is to build the pattern between the SP configuration and its structural strength. Thus, it is a supervised learning problem. The application of supervised learning is presented in section 3.2.2, where a prediction model of the collapse pressure of the SHCC SP is proposed.

Machine learning has been applied to many areas and is very well described in the available literature. Nilashi and Othman [109] applied supervised and unsupervised learning for disease diagnoses and prediction. Yang Liu [110] applied data mining to extract oil reservoir model from data gathered by permanent downhole gauge. Grimstad and Gunnerud [111] applied data mining to transform production data of an oil field under operational guidance. Arun [112] has built a prediction model for the properties of polymer dielectrics using machine learning techniques. Data mining is also employed in electrical engineering [113] and financial area [114]. The extensive applications of machine learning by scholars from different areas prove the stability and maturity of this technique.

2.6 Summary

This chapter reviews researches related to the core materials, collapse pressure, installation method, thermal insulation of the SP. Further, the optimum design methods of subsea pipelines have been discussed. Based on the review, several observations are obtained:

1. There are two types of the SP core materials, which are the cementitious composites and the polymeric materials. Most of the previous researches focused on SPs with PP or SHCC core. Researches on the PCM incorporated cementitious composite in the area of the residential building show a new promising material for the SP.

2. The analytical solutions for the SP collapse pressure give insightful understandings of the problem and are quick to conduct. Since the development of the analytical solution involves several simplifications, the prediction accuracy needs to be evaluated. The collapse pressure obtained by the experiment is more reliable. However, the preparation of the collapse test needs extra time and work. Previous researchers conducted collapse tests on the SPs with SHCC, PP, and cement cores. With proper modeling, finite element simulation is able to provide accurate SP collapse pressure subjected to different loadings.

Empirical equations were proposed for a quick estimation of the SP collapse pressure. There are two types of empirical equations, the one developed by simplifying the analytical solution and the one developed by regression using numerical simulation results.

3. Reeling-lay is a suitable installation method for the SP since it reduces the offshore welding time. For the SP with a diameter that exceeds the limit of the reeling-lay, using special SP connectors seems to be a feasible solution. During the installation process, the SP experience several loads like bending, tension, and external hydrostatic pressure.

4. Flow assurance is a broad topic that involves issues like wax and hydrate deposition, slugging, scales formation, and corrosion. Thermal insulation is employed mainly to prevent the wax and hydrate formation. The SP is a kind of passive insulation system which needs to be designed with respect to the thermal insulation requirements. The heat transfer process inside the SP can be analyzed by heat conduction equations of a multilayer pipeline.

5. By far, the design of a pipeline with respect to structural and thermal insulation requirements is conducted separately. This is reasonable for the SW and the PIP, where the steel layer and insulation layer perform only one function, which is to provide structural resistance or thermal insulation. In this circumstance, the structural design is independent of the insulation design. The thickness of the structural layer has little impact on pipeline insulation capacity and vice versa. Unlike the conventional pipeline, the core layer of the sandwich pipe provides both insulation and resistance. Thus, the design of the SP is constrained simultaneously by the structural and thermal insulation requirements. Few studies that combined the thermal and structural analysis in the pipeline design were reported. Moreover, only one research [11] which carries an integral design to optimize the overall SP design was found in the literature.

Chapter 3

Collapse pressure of SHCC SPs

Cementitious composite material is a major option for the core material of an SP system. The collapse pressure and post-buckling behavior of an SP system with cementitious composite material differ from those of an SP system with PP cores for two reasons: 1) The interlayer adhesion should be differently considered in the numerical model for the different core materials. During the manufacturing process, it is difficult to avoid the presence of air bubbles at the interfaces between the steel tubes and the SHCC core, which weakens the interlayer bonding strength. Therefore, while the fully bonded condition may be acceptable for an SP system with PP core, it is not realistic for an SP system with SHCC core. An et al. [19] also found that a numerical model with unbonded interfaces could better reflect the actual interface conditions of SP systems with SHCC cores. 2) The material setting is completely different. Previous researchers assumed that PP is a linear elastic or a hyperelastic material. For the SHCC material, the compressive and tensile behaviors are not the same. The plastic behavior of the SHCC under tension is complex due to the appearance of microcracks. Therefore, the objectives of this chapter are to fully investigate the collapse pressure and the post-buckling behavior of several SPs with SHCC cores, and to develop an accurate and quick prediction model for SHCC SPs.

Initially, the experimental procedure and results about the collapse pressure of SPs with SHCC cores were examined. Next, the experimental data were used to establish and calibrate the numerical model. A parametric study of SP with practical configurations was then performed. The collapse pressure and post-buckling behavior were thoroughly investigated. Then the analytical solutions for the SP collapse pressure, shown in appendix A, were evaluated with the experimental results. Based on the extensive simulation results, supervised machine learning techniques were applied to support the regression of equations in different forms, which come from three sources: (a) equation forms proposed by previous researchers, (b) equation forms found by the automatic machine learning software EUREQA [115, 116], and (c) equation forms proposed in the thesis. Further, the performance of the

equation forms in terms of prediction accuracy was compared. Finally, the equation form with the best accuracy was suggested for the design of SHCC SPs.

3.1 Experiments and parametric study

3.1.1 Experiments and Results

An et al. [19] conducted experimental research on SPs with SHCC cores. The researchers explained the details of the experiments on both material characteristic testing and the collapse of SPs. The present research followed the same experimental procedure carried out in An's work. However, this study conducted nine new collapse tests on SPs with different configurations and included SS316 stainless steel, which possesses rough internal and external surfaces. A different super-plasticizer was used for the SHCC, which caused slightly different mechanical behavior.

Material characteristics

To evaluate the material mechanical behavior, tensile tests were conducted for the two stainless steel types, SS304 and SS316, and compression tests were carried out for SHCC. Their mechanical behaviors were used later for the ABAQUS simulation. *Stainless steel* Samples were extracted along the longitudinal direction of the stainless-steel pipe that composed the sandwich pipe prototype. The thickness of the SS316 was 2.77 mm and that of the SS304 was 2 mm. Tensile tests were carried out on the samples using an Instron machine with a strain-rate of 0.1 mm/min. Figure 3.1 shows the mechanical behavior of both the SS304 and SS316 specimens.

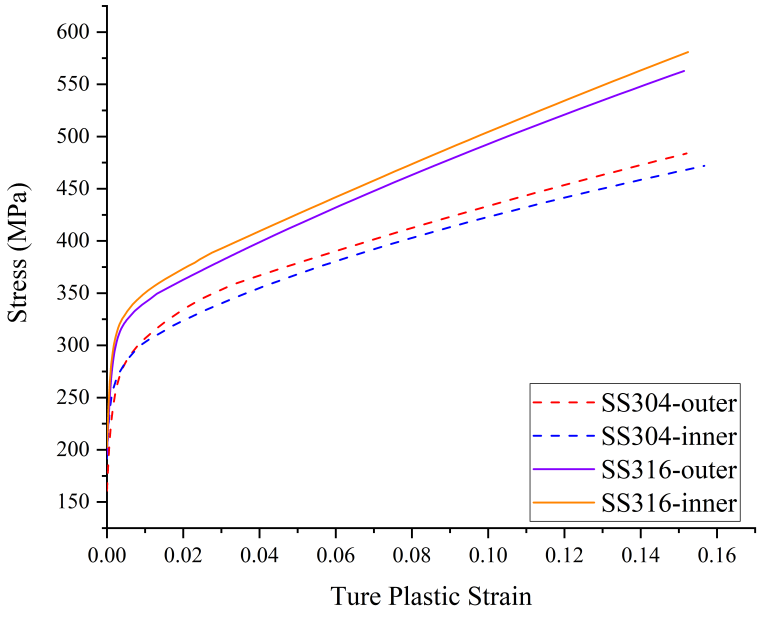

Figure 3.1: Mechanical characteristics of stainless steel

SHCC material The composition and fabrication process of the SHCC were introduced in detail by An et al. [19]. Three SHCC cylindrical samples were manufactured with diameters of 50 mm and heights of 100 mm. The end surfaces of the samples were flattened by polishing to avoid premature rupture problems caused by uneven surfaces during the compression tests. Uniaxial compression tests were conducted at an axial strain rate of 0.020 mm/min. The fitted curve was acquired by averaging the three tested curves. Figure 3.2 shows the tested curves and their best fits.

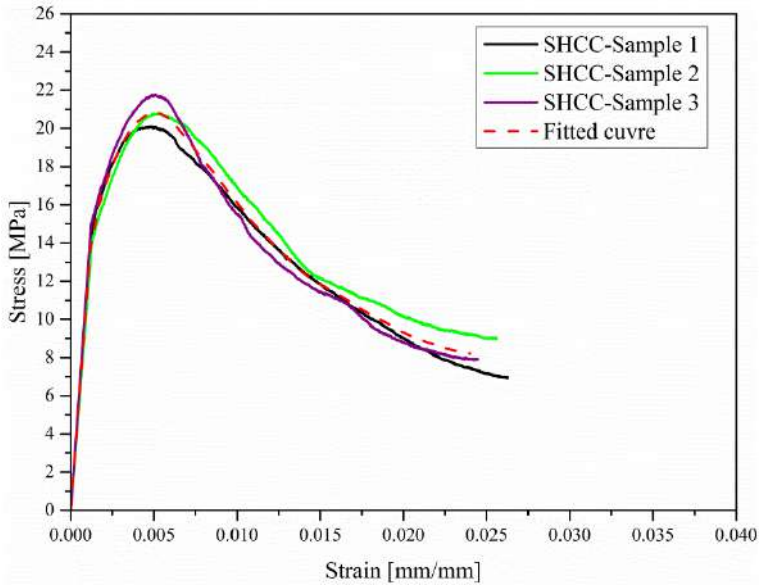

Figure 3.2: Tested strain-stress relationships and fitted curves

Collapse experiments of SP systems

Nine SPs, five SPs with SS304, and four SPs with SS316 were prepared for the collapse experiments. For SPs composed of the same stainless steel, the geometric imperfections (out-of-roundness) of the outer pipe varied for each prototype while other geometries were the same. Table 3.1 presents the geometries of the SPs and each stainless steel.

The cross section of a real pipe is not a perfect circle and its diameter varies along the circumferential direction (see Figure 3.3-a). The geometric imperfection of a pipe refers to the magnitude of its initial ovality. To measure the geometric imperfection, the cross sections of the pipe were marked along the pipe length (see Figure 3.3-c). The shapes of the cross sections at each marked point were then measured with the aid of FARO'S portable measuring arms (see Figure 3.13-b). The geometric imperfection of each cross section is given by equation 3.1. And the geometric imperfection of the pipe is defined by equation 3.2.

Table 3.1: Geometrical parameters for sandwich pipes

Prototype	Stainless steel	Prototype Length (mm)	D_3 (mm)	D_1 (mm)	t_2 (mm)	$t_1 = t_3$ (mm)	Imp_3 (%)
SP-1A	SS304	1250	203.20	148.40	23.40	2.00	0.29
SP-2A	SS304	1250	203.20	148.40	23.40	2.00	0.33
SP-3A	SS304	3370	203.20	148.40	23.40	2.00	0.57
SP-4A	SS304	2600	203.20	148.40	23.40	2.00	0.34
SP-5A	SS304	2600	203.20	148.40	23.40	2.00	0.46
SP-1B	SS316	3125	219.08	162.74	22.63	2.77	0.19
SP-2B	SS316	3000	219.08	162.74	22.63	2.77	0.50
SP-3B	SS316	3000	219.08	162.74	22.63	2.77	0.57
SP-4B	SS316	2600	219.08	162.74	22.63	2.77	0.40

$$Imp^k = \frac{D^k_{max} - D^k_{min}}{D^k_{max} + D^k_{min}}; \qquad k = B, C...H \tag{3.1}$$

$$Imp = max\{Imp^k; \quad k = B, C...H\} \tag{3.2}$$

where Imp^k is geometric imperfection of a pipe at the k-th cross section, D^k_{max} is the maximum outside diameter of a pipe at the k-th cross section, D^k_{min} is the minimum outside diameter of a pipe at the k-th cross section, and Imp is the geometric imperfection of a pipe.

The prototypes were put inside a hyperbaric chamber with welded lids to close the ends. Then, the hyperbaric chamber was filled with water. The pressure was increased at a rate of 60 psi/min by pumping water into the chamber. The experiments were concluded when a sudden drop of pressure occurred, which implied the collapse of the SP prototype.

Table 3.2 lists the collapse pressures of all prototypes. As shown, for most cases, the prototypes with bigger geometric imperfection showed lower collapse pressures. The prototypes composed of SS316 usually showed higher collapse pressures, since the rough surface of SS316 increased the inter-layer friction between the layers of the SPs, thus representing a boundary condition more restrained than that of SPs composed of SS304.

Table 3.2: Collapse pressures of sandwich pipes

Prototype	P_{co} (MPa)	Prototype	P_{co} (MPa)
SP-1A	37.68	SP-1B	38.71
SP-2A	35.96	SP-2B	34.29
SP-3A	35.23	SP-3B	37.57
SP-4A	37.18	SP-4B	39.05
SP-5A	36.92		

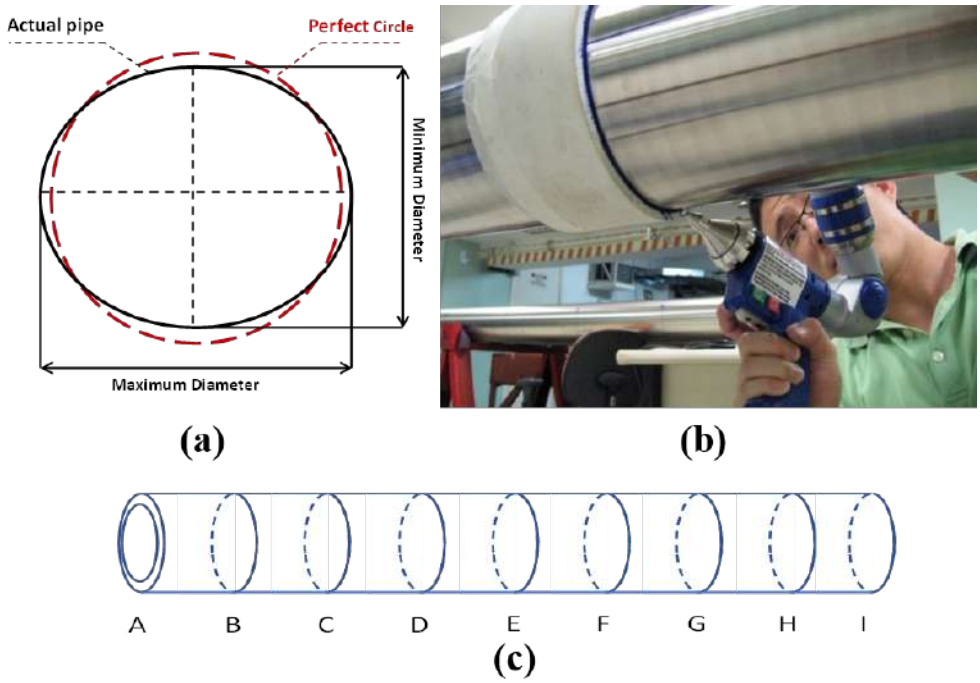

Figure 3.3: Measurement of the geometric imperfection of a pipe: (a) Illustration of geometric imperfection; (b) Measuring pipe shape with FARO arm; (c) Mark the cross sections along the length

3.1.2 Finite Element Model

The finite element (FE) method was adopted to build a set of quasi 2D models that represent the cross-section of a sandwich pipe, assuming an infinite length. The modeling used ABAQUS CPE8, 8-nodes biquadratic plane strain quadrilateral, with the 2D element. Symmetry conditions reduced the problem to a quarter of a ring, as shown in Figure 3.5. Based on mesh sensitivity studies, an FE mesh consisting of 40 elements along the circumferential direction was considered adequate to capture the characteristic behavior with good accuracy, see Figure 3.4-a. Since the thickness of each layer would vary in the parametric study, no specific number of elements was established. The software ABAQUS was used to automatically decide the number of elements through the radial direction. A mesh sensitivity study showed that the element number at the radial direction has no significant impact on the simulation results, see Figure 3.4-b.

In order for the numerical models to capture the actual response of the system, geometric imperfections were assumed. A geometric imperfection, assumed as an initial ovality, was applied to the pipe cross section. Ovality positions for both the inner and outer pipes were assumed to be coincident. The radial displacement due to the geometric imperfection is defined as:

$$\omega_i(\theta) = Imp_i \times r_i \times cos2\theta, \qquad i = 1, 3 \tag{3.3}$$

where $\omega_i(\theta)$ is the imperfection induced radial displacement of the i-th layer, and r_i is the outside radius of the i-th layer.

To verify the numerical model against the experimental results, the geometric imperfection of the inner pipe is assumed equal to that of the outer pipe. In the parametric study, different geometric imperfections were applied to each layer.

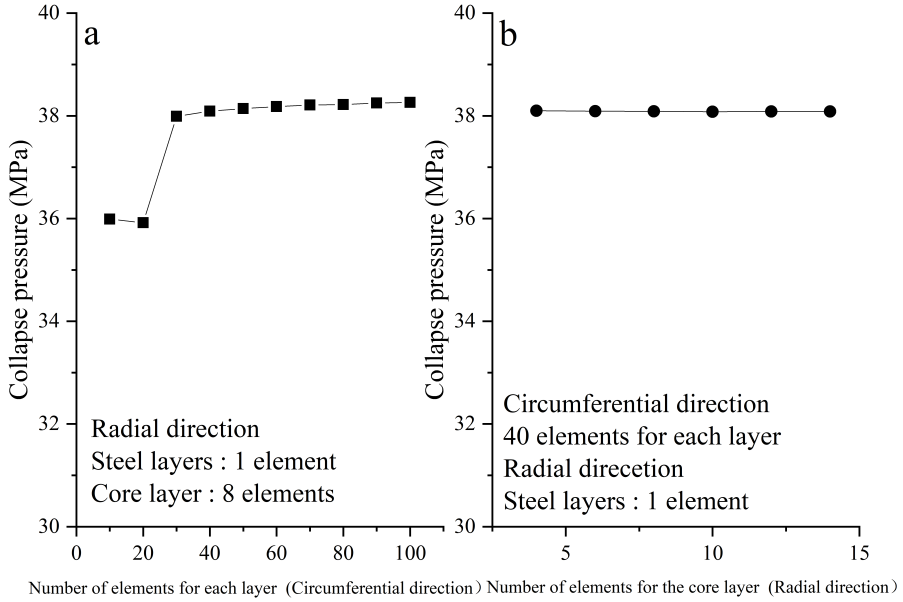

Figure 3.4: Mesh sensitivity study

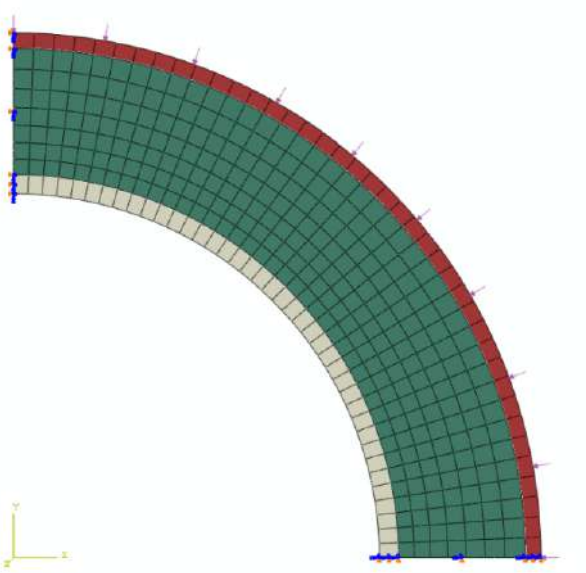

Figure 3.5: 2D finite element model for the SP system

Material properties

The outer and inner tubes of the SPs used SS304 or SS316 stainless steels. Elastic properties with a Young's modulus of 200GPa and a Poisson's ratio of 0.3 were

assumed for both SS316 and SS304. The plastic properties of the stainless steels were obtained from the experimental results, as displayed in Figure 3.1. Based on the experimental data, the steel layers were modeled by Hooke's law in the elastic regime and the potential flow J2 was associated with isotropic hardening and von Mises yield criteria in the plastic regime.

For the SHCC layer, a Young's modulus of 11.41GPa and a Poisson's ratio of 0.2 were assumed. The Drucker-Prager yield criterion, which is widely used for equivalent pressure dependent materials like soil and concrete, was selected to model the behavior of the SHCC layer. The criterion states that the plastic flow of a material begins when the second invariant of the deviator tensor and the first invariant of the Cauchy stress tensor reach a critical combination [117]. A linear Drucker-Prager model defined by equations 3.4, 3.5, and 3.6 was used for the yielding prediction of the SHCC [48].

$$T = I_1 \times tan\beta + d \tag{3.4}$$

$$T = \frac{1}{2}\sigma_{vm}\left[1 + \frac{1}{K} - \left(1 - \frac{1}{K}\right)\left(\frac{J_3}{\sigma_{vm}}\right)^3\right] \tag{3.5}$$

$$d = \left(1 - \frac{1}{3}tan\beta\right)\sigma_c \tag{3.6}$$

where I_1 is the first invariant of the Cauchy stress tensor, β is the friction angle of the material, d is the cohesion of the material, K is the flow stress ratio, J_3 is the third invariant of the deviator stress tensor, σ_{vm} is the Mises equivalent stress, and σ_c is the yield stress of the uniaxial compression.

The friction angle of the SHCC for the Mohr-Coulomb model was proved to be 35° with details in one of the study at LTS [118]. According to the matching relation between the Mohr-Coulomb model and the Drucker-Prager model defined by ABAQUS user manual [48], a friction angle (β) of 45° was determined for the Drucker-Prager model. A cohesion factor (d) of 10.73 MPa was determined using the compression experiment data. A default value in the ABAQUS is used for the flow stress ratio (K). For the plasticity behavior, a hardening model was employed using the stress-strain relationship from Figure 3.2.

Load and boundary conditions

The ultimate structural strength of a sandwich pipe subjected to external pressure was investigated by employing the Riks method (arc length method). External pressure was applied to the outer pipe through the surface load, as shown in Figure 3.5. The symmetry boundary conditions were employed on the x-z and y-z planes.

The setting of the maximum pressure increment significantly affects the simulation results. A large pressure increment can lead to inaccurate collapse pressure while a small pressure increment might result in, for models with high structural stiffness, a displacement near to zero which causes convergence problem. The numerical settings were carefully adjusted to avoid these two problems.

Inter-layer adhesion modeling

The adhesion behavior between the core layer and the outer/inner pipes has significant influences on the collapse pressure of a sandwich pipe. Similar to the work that An [19] conducted for an SP system with an SHCC core, the surface-based contact interaction model involving a strict master-slave algorithm was applied to the interface of the steel tube and core material. When simulating the physical situation, the master surfaces were the inner surface of the outer steel pipe and the inner surface of the core layer. The contact pressure model was set to normal behavior and the Coulomb friction model was set to tangential behavior. There are three types of interface conditions. 1) For partial friction, the "Hard Contact" relation and "Allow separation after contact" were applied to the surface normal direction. The "penalty" method was applied along the tangential direction, where the friction coefficient was adjusted to match the experimental data. 2) For frictionless, the normal behavior remained the same while "Frictionless" was selected for the tangential behavior. 3) For fully bonded, the "Hard Contact" relation and "Not allow separation after contact" were applied to the normal behavior. Friction coefficient was set to 1 for tangential behavior. Note that the "penalty" method is the Coulomb friction model in the software ABAQUS where the maximum allowable frictional (shear) stress across an interface is proportional to the contact pressure between the contacting bodies.

Model verification

Using the geometric parameters of the experimental prototypes, numerical simulations were carried out using the ABAQUS software. The collapse pressures of the SP system under different inter-layer adhesions were obtained. Figures 3.6 and 3.7 compare the numerical and experimental results. For all prototypes, the measured collapse pressures remained between the results given by the fully bonded FE model and frictionless FE model, which agrees with the fact that the actual sandwich pipe with SHCC material had a partially bonded interface condition. The adjustment of the friction coefficient can reflect the inter-layer adhesion strength. Since the experimental collapse pressure of the prototype SP-2B was detected as a probable error, it was not used for the adjustment of the friction coefficient. For prototypes

with SS304 steel, the simulation results better match the experimental data with a friction coefficient equal to 0.1. The average error is 1.88%. For prototypes with SS316 steel, the friction coefficient was adjusted to 0.2 to fit the experimental data. The average error is 2.39%. The reason that the two groups need different friction coefficients for the FE model to match the measured collapse pressure is that the surface of the SS304 steel was polished and that of the SS316 steel was not. Therefore, the SS316 can provide higher friction at the interface. The good agreement between the numerical simulation results and the experimental data shows that the FE model is capable of providing accurate results.

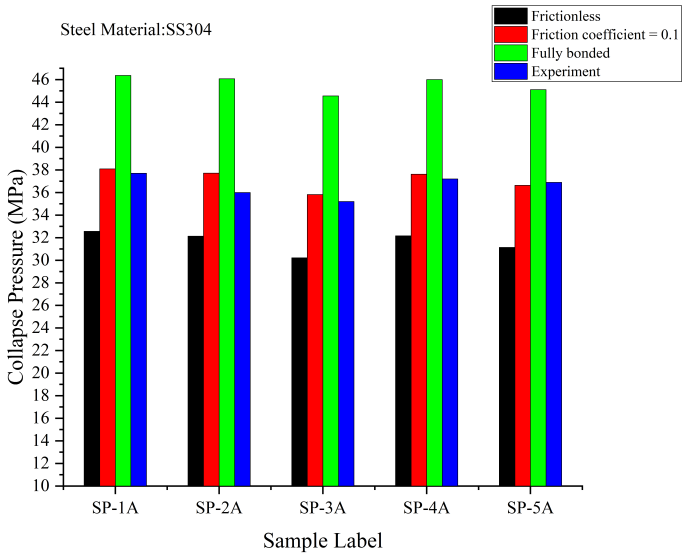

Figure 3.6: Comparison of numerical results and experiments for prototypes using SS304

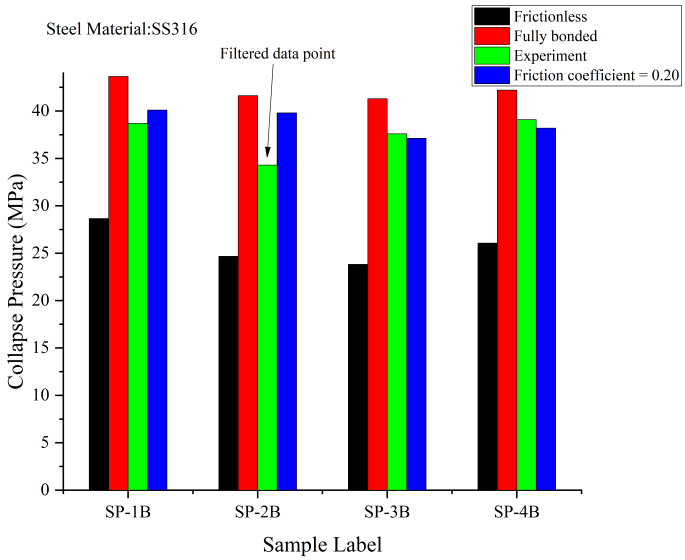

Figure 3.7: Comparison of numerical results and experiments for prototypes using SS316

3.1.3 Parametric Study

Parameter range

With the calibrated numerical model, the collapse pressure and post-buckling behavior were studied through a comprehensive parametric study. No adhesion was assumed for the inter-layer condition for a conservative estimation. Since it was observed in both this work and previous studies [10, 45] that the stress-strain curve's profile of steel after the yield stress has a small influence on the collapse pressure of the sandwich pipe, the elastic perfectly plastic condition was assumed for the steel tube. The same steel grade was considered for both the inner and outer pipes. The collapse pressure of the sandwich pipe with an SHCC core can then be expressed as:

$$P_{co} = f\left(E_p, t_1, r_1, t_3, r_3, \nu_p, \sigma_p, Imp_1, Imp_3\right) \tag{3.7}$$

The Poisson's ratio (ν_p) of the steel was taken to be 0.3. The thickness-to-radius ratio (t_i/r_i) defines the steel tube configuration. To focus on the practical design of the SP system, API 5L standard was used as a reference to define t_i/r_i. Figure 3.8 shows the applicable limits of the pipeline dimension and the commercially available dimensions for steel pipes. Since the principle behind the SP concept is to reduce the amount of steel compared with the single-wall pipe, steel tubes with high t_i/r_i were avoided in the parametric study. The upper and lower limits of t_i/r_i for the sandwich pipe were taken to be 0.08 and 0.02. This range lies inside the applicable limits and is commercially available.

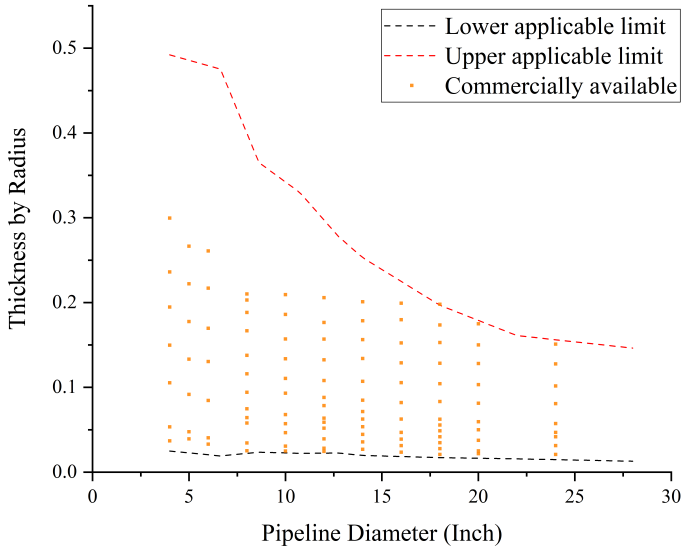

Figure 3.8: Applicable limits and commercially available dimensions for steel pipes

Three steel grades of X60, X80, and X100 were chosen and the respective yield stresses were defined by the API standard. The ratio between the radius of the inner and outer pipes (r_1/r_3) was selected to define the thickness of the core layer.

0.65 was taken as its lower bound, since an SP system with SHCC cores in this configuration already reaches extremely high ultimate structural strength. 0.82 was set as the upper bound since it is not adequate for a practical SP system to have an extremely thin core layer. According to the API 5L standard, 1.5% was set to the upper bound of the geometric imperfection of the pipeline. The major axes of the inner and outer pipes were assumed to be consistent. Table 3.3 summarizes the parameter ranges.

Table 3.3: Parameter ranges for the parametric study

t_1/r_1	t_3/r_3	r_1/r_3	Imp_1	Imp_3	Steel grade
0.02	0.02	0.65	0.20%	0.20%	X60
0.03	0.03	0.70	0.60%	0.60%	X80
0.05	0.05	0.73	1.10%	1.10%	X100
0.06	0.06	0.76	1.50%	1.50%	
0.08	0.08	0.82			
Note: 1 for inner steel layer; 3 for outer steel layer					

The parameters in Table 3.3 make up 6000 combinations for the parametric study. A Python code was written to manage the large number of simulations in the ABAQUS software.

Results and Discussion

The behavior of the SHCC material in the plasticity regime and the frictionless inter-layer condition increased the complexity of the collapse mechanism of the SP system. Therefore, the effects on the collapse pressure of some parameters are not independent. In other words, the variation tendency of some parameters for the collapse pressure of the SP system depends on other parameters. For example, the variation of the collapse pressure with respect to the thickness-to-radius ratio of the outer steel pipe (t_3/r_3) can be influenced by other parameters like the core thickness (r_1/r_3). In this section, the effects of each parameter on the collapse pressure of the SP system are fully examined to capture the collapse behavior of the SP system for different configurations. Post-buckling behavior is also discussed.

The effect of the thickness-to-radius ratio of the outer steel pipe (t_3/r_3)
The thickness-to-radius ratio is a critical design parameter for the SP system that affects the ultimate structural strength, cost, and immersed weight. The influence of the thickness-to-radius ratio of the outer steel pipe on the ultimate structural strength of the SP system is thoroughly discussed below.

Figure 3.9 shows the variations of the collapse pressure of the SP configurations with different core thicknesses and inner pipe dimensions ($r_1/r_3, t_1/r_1$) with respect

to the outer pipe dimensions (t_3/r_3). The variation tendency of P_{co} with respect to t_3/r_3 can be altered depending on the inner pipe dimensions (t_1/r_1) ratio and the core thickness (r_1/r_3). For an SP system with a thick core (Figure 3.9-a), P_{co} increases along with t_3/r_3 when the inner pipe is relatively thin ($t_1/r_1 \leq 0.03$). This correlation between P_{co} and t_3/r_3 reverses when t_1/r_1 is higher than 0.03, leading to P_{co} decreasing with increases of t_3/r_3. For an SP system with a moderately thick core (Figure 3.9-b), an increase of t_3/r_3 causes a decrease of P_{co} until t_3/r_3 reaches 0.05; thereafter, P_{co} increases. This variation tendency seems more obvious when $t_1/r_1 \geq 0.05$. For an SP system with a thin core (Figure 3.9-c), P_{co} constantly increases with the increase of t_3/r_3.

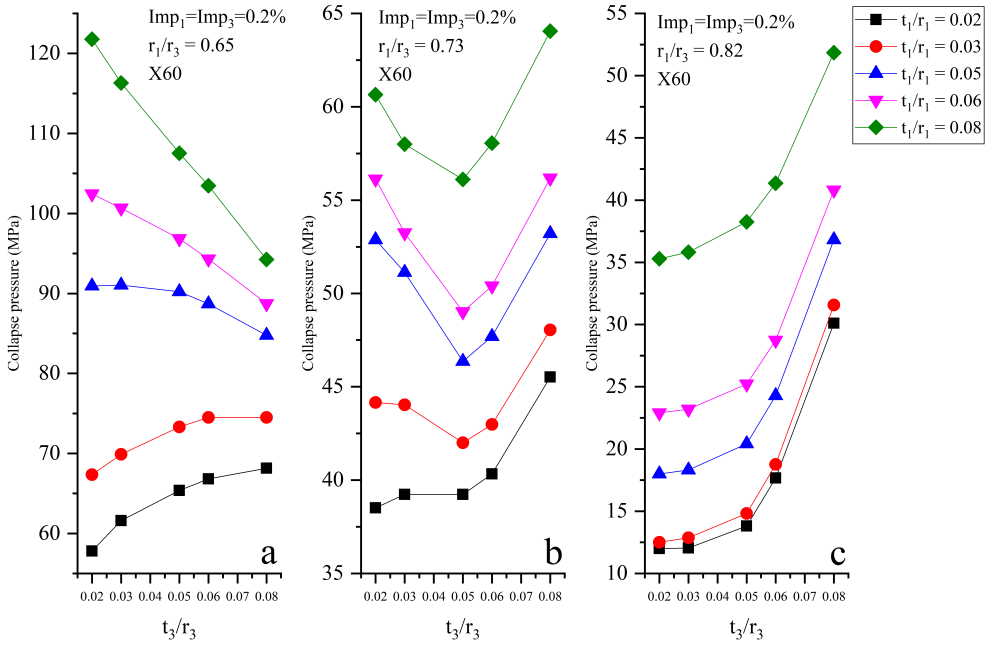

Figure 3.9: Effect of outer pipe thickness-to-radius ratio on the collapse pressure of the SP system: (a) SP with thick core $r_1/r_3 = 0.65$; (b) SP with moderately thick core $r_1/r_3 = 0.73$; (c) SP with thin core $r_1/r_3 = 0.82$;

Usually, one expects higher collapse pressure for a SP with a thicker outer steel pipe. The decrease of P_{co} with the increase of t_3/r_3 observed in some cases is counterintuitive. A typical group of SPs (Table 3.4) that represents this tendency was thoroughly analyzed to explain the reason behind this observed behavior.

Table 3.4: Parameters for different SP configurations

Case label	Steel grade	t_3/r_3	t_1/r_1	r_1/r_3	Imp_1	Imp_3	P_{co} (MPa)
SP-a	X60	0.02	0.05	0.73	0.20%	0.20%	52.88
SP-b	X60	0.03	0.05	0.73	0.20%	0.20%	51.14
SP-c	X60	0.05	0.05	0.73	0.20%	0.20%	46.36
SP-e	X60	0.06	0.05	0.73	0.20%	0.20%	47.69
SP-d	X60	0.08	0.05	0.73	0.20%	0.20%	53.21

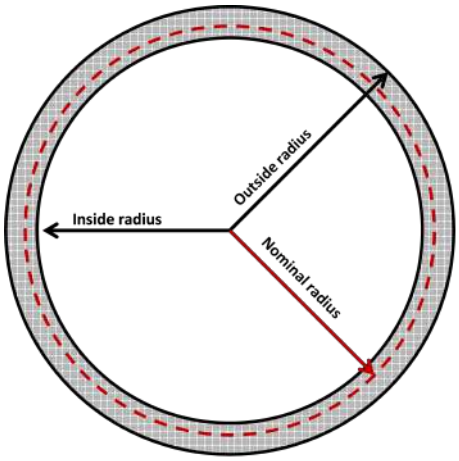

Figure 3.10: Illustration of different definitions for the pipe radius

(1) The definition of radius for the study There are three definitions of the radius of a pipe: inside radius, nominal radius, and outside radius (Figure 3.10). According to the ASME standards, the nominal radius stays between the inside and the outside radius for pipes with diameter from 1/8 inches to 12 inches and the nominal radius equals to the outside radius for pipes with diameter above 12 inches. Since this study focused on the external collapse pressure, the outside radius was applied in the study so that SPs with the same radius but different thicknesses of the outer steel pipe would have the same interaction area with the surrounding water. Besides, for a pipeline with a diameter above 12 inches, the nominal radius is equal to the outside radius.

Because the outside radius was considered for SP systems with the same r_1/r_3, increasing t_3/r_3 increases the thickness of the outer steel layer while decreasing the thickness of the core layer, as seen in Figure 3.11. Although it is not a simple summation, the ultimate structural strength of the SP system comes from three main sources: the inner steel pipe, the core layer, and the outer steel pipe. To observe the strength variation of each layer with respect to t_3/r_3, simulations were carried out treating each layer of the SP system as a single wall pipe to investigate their individual ultimate structural strengths, as indicated in Table 3.4. As shown in Figure 3.12, increasing t_3/r_3 improves the ultimate structural strength of the SP system by increasing the structural strength of the outer pipe, but also reduces the ultimate structural strength of the SP system by decreasing the structural strength of the core layer. Regarding the entire SP structure, the ultimate structural strength decreases for $t_3/r_3 \leq 0.05$ and then increases for $t_3/r_3 > 0.05$.

Figure 3.13 illustrates the characteristic responses (pressure vs ovality) of the SP systems shown in Table 3.4. The ovality of the sandwich pipe at the corresponding pressure can be calculated as:

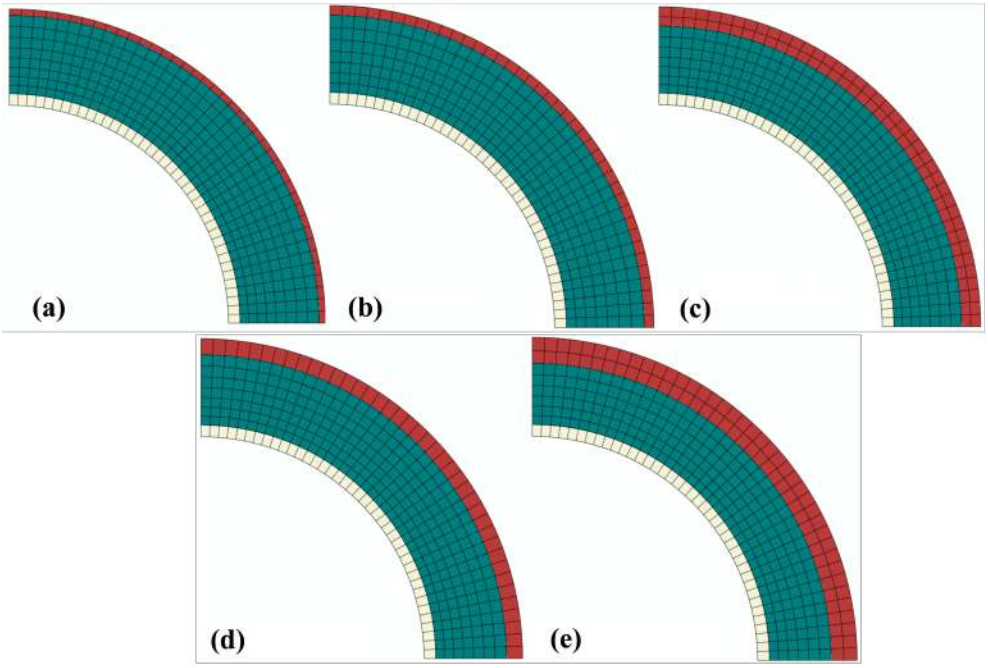

Figure 3.11: SP configurations with the same r_1/r_3 and different t_3/r_3: (a) $t_3/r_3 = 0.02$; (b) $t_3/r_3 = 0.03$; (c) $t_3/r_3 = 0.05$; (d) $t_3/r_3 = 0.06$; (e) $t_3/r_3 = 0.08$

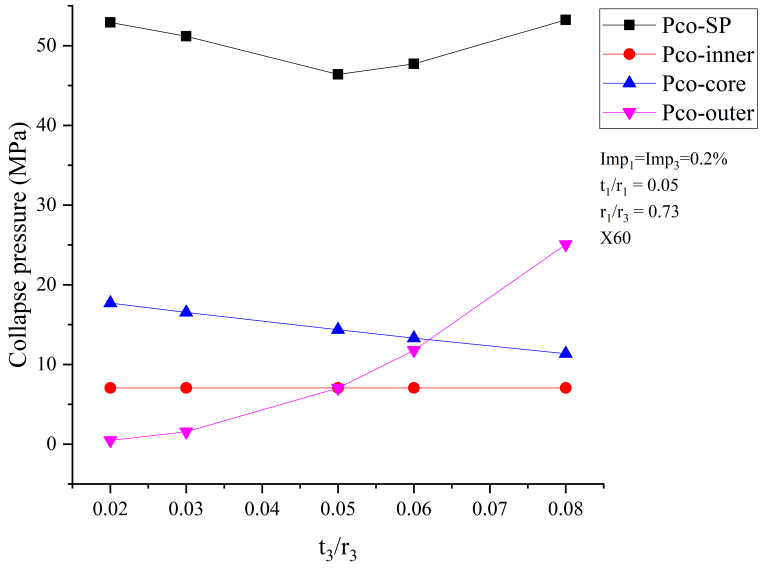

Figure 3.12: P_{co} of the SP system and P_{co} of each layer in the SP system with respect to t_3/r_3

$$\Delta(P) = \frac{D_{3,max}(P) - D_{3,min}(P)}{D_{3,max}(P) + D_{3,min}(P)} \tag{3.8}$$

where $\Delta(P)$ is the ovality of a sandwich pipe under external pressure P, $D_{3,max}(P)$ is the maximum outside diameter of the outer steel pipe at pressure P, and $D_{3,min}(P)$ is the minimum outside diameter of the outer steel pipe at pressure P.

The moment when collapse happens was marked by a star point on each curve of

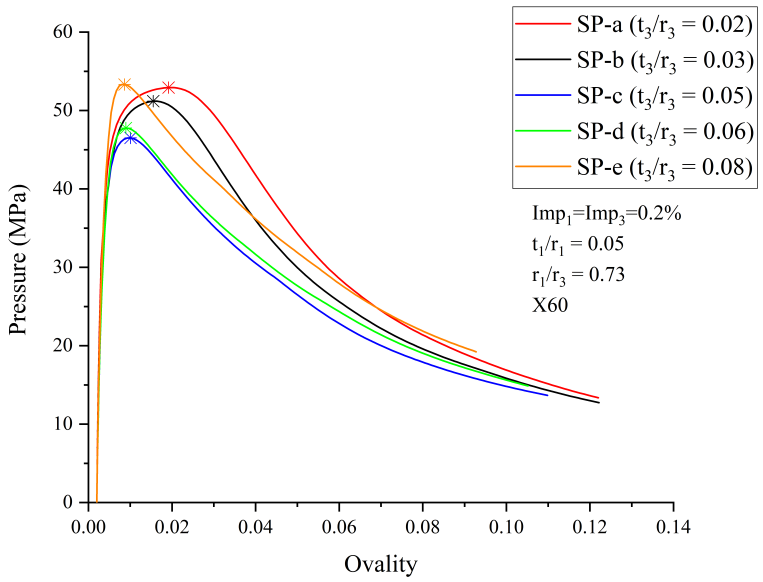

Figure 3.13: Characteristic responses of the SP systems with increasing thickness of outer steel pipe (Frictionless inter-layer condition)

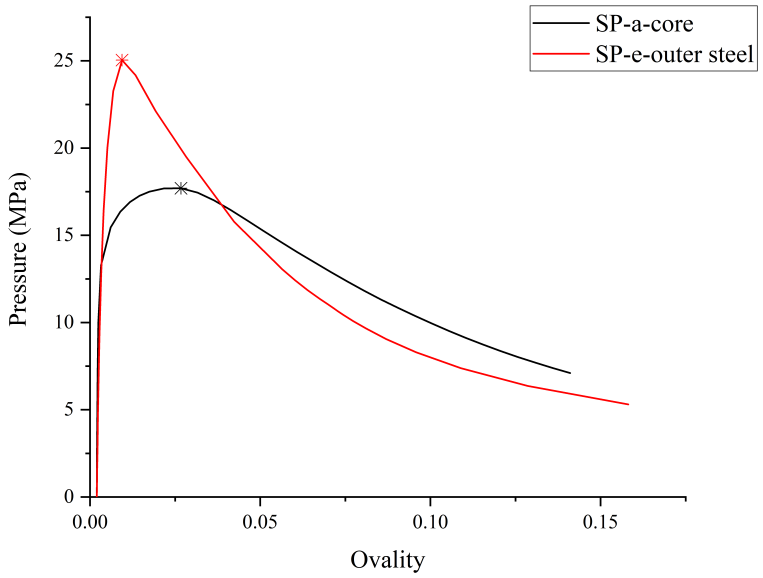

Figure 3.14: Characteristic responses of component layers of the SP: the core layer of the SP-a and outer steel layer of the SP-e

characteristic response. The ordinate of a star point represents the collapse pressure as well as the ultimate structural strength of the corresponding SP. The abscissa of a star point represents ovality of the corresponding SP at the collapse pressure. It is the ability of a SP to ovalize before collapse. The term "capacity to ovalize before collapse" is used to refer this ability of a SP for the following discussion. By varying the t_3/r_3 ratio in a range of 0.02 to 0.05, the SP system loses both capacity to ovalize before collapse and ultimate structural strength. With t_3/r_3 ratios ranging from 0.05 to 0.08, the SP system gains ultimate structural strength but continues to lose capacity to ovalize before collapse. Figure 3.14 shows the characteristic response

of the core layer of the SP-a and the outer steel layer of the SP-e, where both layers were treated as a single wall pipe for the collapse simulation. Due to the SHCC properties, the core layer displays more capacity to ovalize before collapse than the steel pipe and maintains a relatively higher strength in the post-collapse regime. As illustrated in Figures 3.12, 3.13 and 3.14, the SP system behaves similar to the core layer, showing more capacity to ovalize before collapse when the core layer has higher ultimate structural strength than that of the steel layer, as in SP-a. And the SP system exhibits behavior closer to the steel pipe, showing less capacity to ovalize before collapse when the outer steel layer is stronger than the core layer, as in SP-e. Since there was no friction between layers, the ultimate structural strength of the SP system was not proportional to the summation of the ultimate structural strength of the components. The response of the SP system seems to be dominated by the strongest layer among its components. Therefore, varying t_3/r_3 ratios in a range of 0.02 to 0.05 increases the summation of the collapse pressures of the component layers but decreases the ultimate structural strength of the entire SP because the ultimate structural strength of the dominating layer decreases, which in these cases is the core layer. With t_3/r_3 ratios ranging from 0.05 to 0.08, the dominating layer shifts from the core layer to the outer steel layer. Thus, the ultimate structural strength of the entire SP increases with an increasing t_3/r_3 ratio.

(2) Frictionless inter-layer bonding Previous researchers found that the bonding condition between layers has a significant influence on the ultimate strength of the SP system. As discussed before, the ultimate structural strength of the SP system with frictionless condition is more relevant to the strength of the strongest layer than to the strength summation for all layers. To observe the influence of inter-layer bonding, the SP configurations in Table 3.4 were simulated with the fully bonded inter-layer condition. Figure 3.15 shows the characteristic responses of the SP system with fully bonded layers. The pressure capacity of the SP systems with fully bonded layers increased with increasing t_3/r_3. This behavior has been observed in most previous research, where the ultimate structural strength of SP systems has been related to the ultimate structural strength summation of all layers rather than the ultimate structural strength of the strongest layer. Therefore, the inter-layer bonding condition affects not only the ultimate structural strength of the SP system, but also the behavior of the SP system according to the variation of the t_3/r_3 ratio.

(3) Different behaviors of the core layer To gain insight into the characteristic responses of SP systems with different t_3/r_3 values, the contour plots of von Mises stress and equivalent plastic strain at the collapse state are shown in

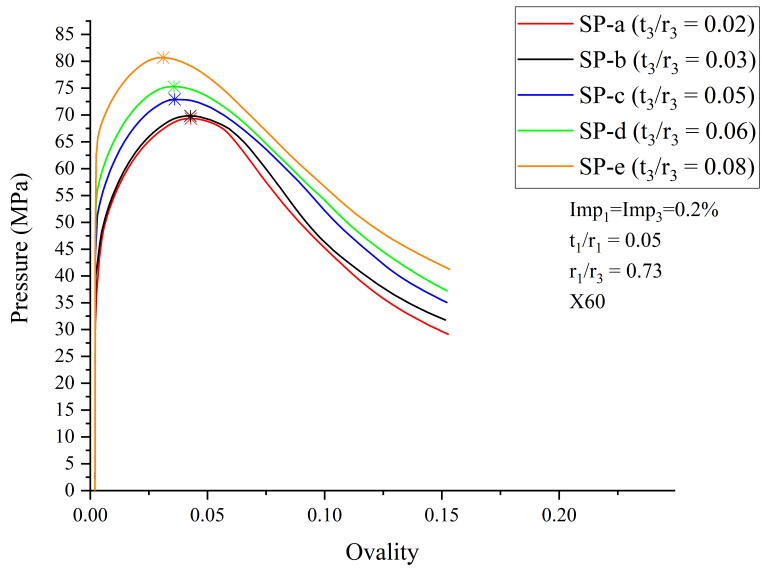

Figure 3.15: Characteristic responses of the SP systems with increasing thickness of outer steel pipe (Fully bonded inter-layer condition)

Figures 3.16 and 3.17. The configurations of the SP systems are indicated in Table 3.4. As shown in Figure 3.16, the maximum stress appears in the steel pipe for each SP. As the t_3/r_3 ratio increases, the von Mises stress of the core layer considerably decreases. When t_3/r_3 equals 0.02, the maximum von Mises stress in the core layer reaches stress values ranging from 79.74 MPa to 113.3 MPa. When t_3/r_3 equals 0.05, the maximum von Mises stress in the core layer decreases to a range from 46.5 MPa to 81.2 MPa. For a SP system with t_3/r_3 ratio of 0.08, the maximum von Mises stress in the core layer further decreases to a range from 11.62MPa to 46.19 MPa. In other words, the contribution of the core layer to the ultimate structural strength of the SP system decreases as the t_3/r_3 ratio increases. A similar phenomenon was observed in the contour plot of the equivalent plastic strain (see Figure 3.19). For SP systems with t_3/r_3 ratios of 0.02 and 0.03, plastic deformation happened both in the core and the steel pipe layers. In contrast, SP systems with t_3/r_3 ratios of 0.05, 0.06, and 0.08 have plastic deformations only in small areas associated with the maximum and the minimum diameters of the steel pipes. This means that the SP-a and SP-b are more efficient at utilizing the strength of the core layer, as the core experienced higher plastic strain and stress at the collapse state. However, SP-c, SP-d, and SP-e have lower efficiencies at utilizing the core layer, since the core experienced elastic deformation with smaller stress responses at the collapse state.

The parametric study shows a counterintuitive phenomenon in which the collapse pressure of the SP system decreases with an increasing t_3/r_3 ratio. For an SP system with frictionless inter-layer relations, both the ultimate structural strength and the post-buckling behavior of the SP system are more related to the strongest layer rather than to the summation of all layers. Using the outside radius in the

parametric study resulted in a reduction of the thickness of the core layer when the t_3/r_3 ratio increases. In some cases, as shown in Table 3.4, the strongest layer of the SP system gradually switched from the core layer to the outer steel pipe with an increasing t_3/r_3 ratio. Because of this, the collapse pressure of the SP experienced a reduction at the beginning, followed by an increase later. At the same time, the curves of characteristic response show that the SP displayed more capacity to ovalize before collapse when the dominating layer was the core and behaved similarly to the steel pipe when the outer steel pipe was thick enough to dominate the entire system. The contour plots of the von Mises stress and equivalent plastic strain show that the SP system dominated by the core layer for a low t_3/r_3 had higher efficiency at utilizing the core layer strength. In this case, the core layer experienced higher plastic strain and stress at the collapse pressure. Figure 3.9-c helps to illustrate this mechanism when an SP system has a thin core layer ($r_1/r_3 = 0.82$). This figure shows that SPs with relatively weak core layers displayed behavior dominated by the outer steel pipe layer. In contrast, in Figure 3.9-a, the P_{co} of SPs with thick core layers ($r_1/r_3 = 0.65$) kept decreasing with the increase of the t_3/r_3 ratio, since the core layer was too thick and dominated the buckling behavior.

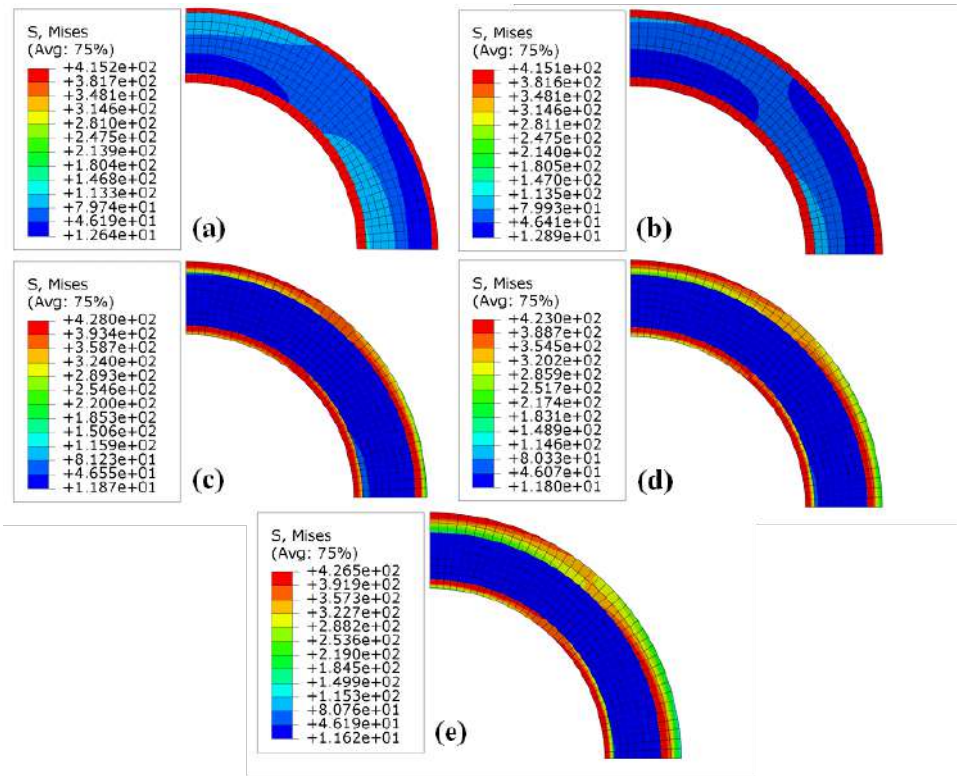

Figure 3.16: Von Mises stress and the cross-section deformation of SPs with the frictionless inter-layer condition at the collapse pressure: (a) $t_3/r_3 = 0.02$; (b) $t_3/r_3 = 0.03$; (c) $t_3/r_3 = 0.05$; (d) $t_3/r_3 = 0.06$; (e) $t_3/r_3 = 0.08$

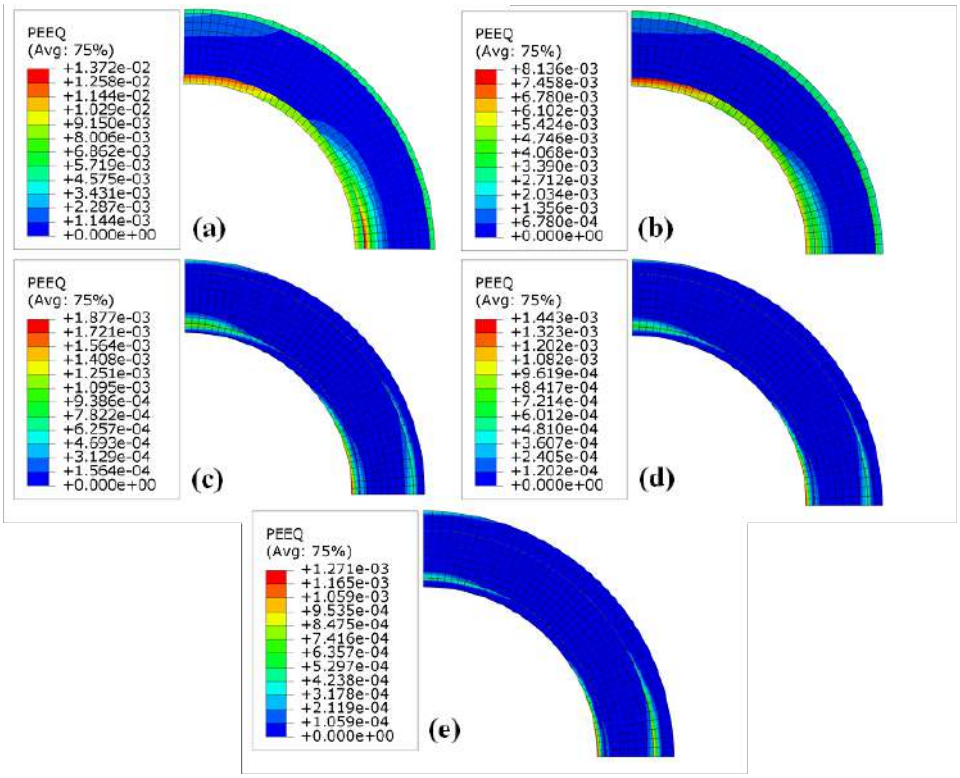

Figure 3.17: Equivalent plastic strain and the cross-section deformation of SPs with the frictionless inter-layer condition at the collapse pressure: (a) $t_3/r_3 = 0.02$; (b) $t_3/r_3 = 0.03$; (c) $t_3/r_3 = 0.05$; (d) $t_3/r_3 = 0.06$; (e) $t_3/r_3 = 0.08$

The effect of the thickness-to-radius ratio of the inner steel pipe (t_1/r_1) The thickness-to-radius ratio of the inner steel pipe also is a key design parameter for an SP system. Similar to the analysis in the previous section, the influence of the t_1/r_1 ratio was analyzed for SP systems with thick ($r_1/r_3 = 0.65$), moderately thick ($r_1/r_3 = 0.73$), and thin ($r_1/r_3 = 0.82$) core layers. As shown in Figure 3.18, the collapse pressure of the SP system is positively correlated with the t_1/r_1 ratio. Since increasing the t_1/r_1 ratio only changes the thickness of the inner steel pipe, which has no influence on the core layer or the outer steel pipe, the ultimate structural strength of an SP system increases as its inner steel layer becomes stronger, without losing the other layers' strength. Note that increasing the t_1/r_1 ratio has different effects on the ultimate structural strengths of SP systems with different r_1/r_3 and t_3/r_3 ratios. For SPs with thick core layers (Figure 3.18-a), an increase of the t_1/r_1 ratio improves the SP ultimate structural strength more efficiently for SPs with lower t_3/r_3. Figures 3.18-b and 3.18-c show that the increase of the collapse pressure of the SPs by the augment of the t_1/r_1 ratio is nearly independent of the t_3/r_3 ratio. It is important to keep in mind that the transformation of the dominating layer also affected the behavior of the SPs, as shown in Figure 3.18, since the figure includes the variation of t_3/r_3 values.

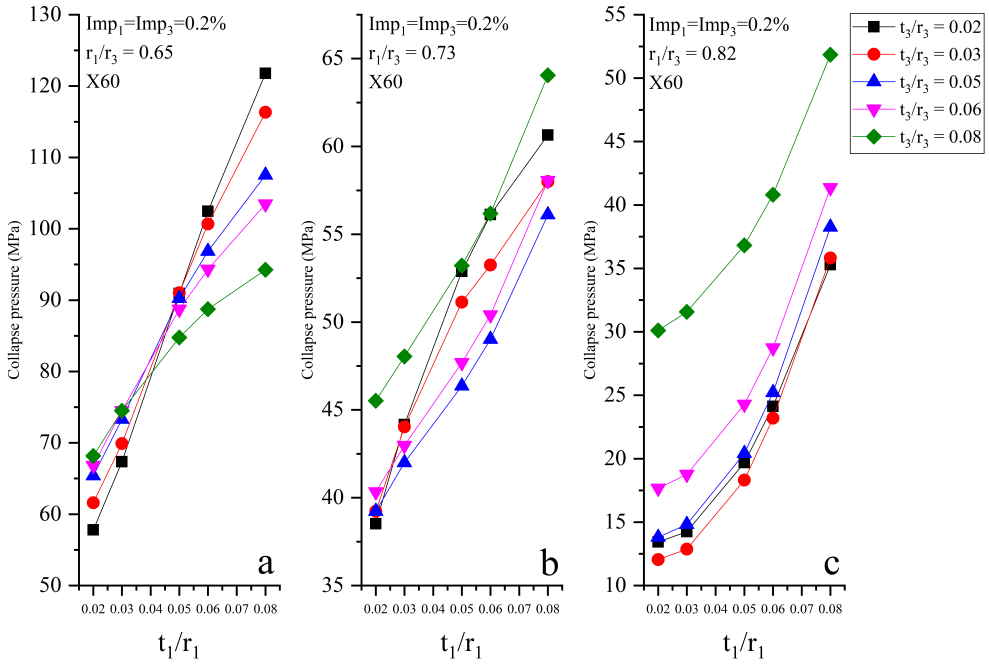

Figure 3.18: Effect of inner thickness-to-radius ratio on the collapse pressure of the SP system: (a) SP with thick core $r_1/r_3 = 0.65$; (b) SP with moderately thick core $r_1/r_3 = 0.73$; (c) SP with thin core $r_1/r_3 = 0.82$

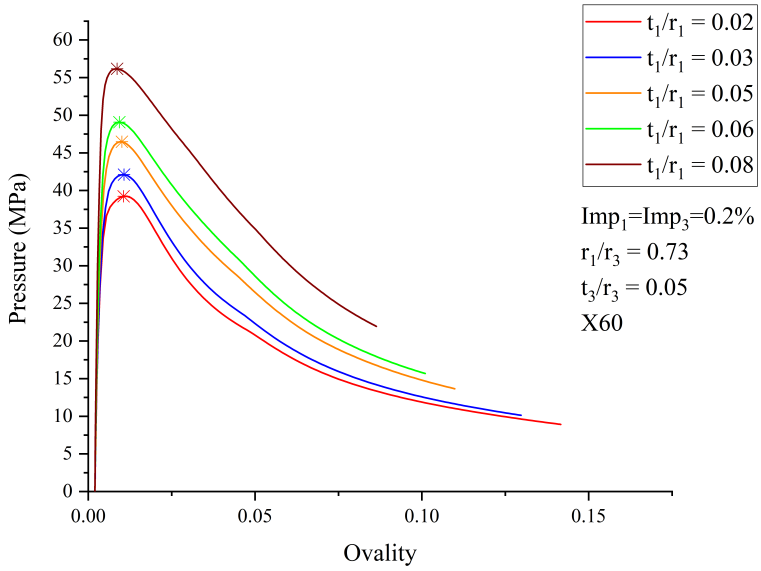

Figure 3.19: Characteristic responses of the SP systems with increasing thickness of inner steel pipe(Frictionless inter-layer condition)

The effect of core thickness The core layer is the most critical part of an SP system, as it provides both thermal insulation and ultimate structural strength. Figure 3.20 shows the characteristic responses of SPs with different core layer thicknesses. The ultimate structural strength improves as the core layer becomes thicker. However, the capacity to ovalize before collapse of the SP system barely changes, since the thicknesses of the steel pipes was fixed.

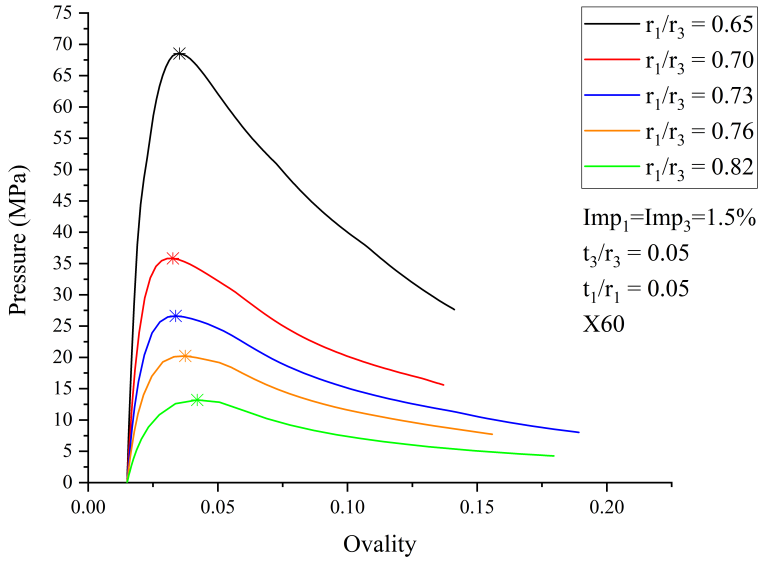

Figure 3.20: Characteristic responses of SP systems with different core thicknesses (Frictionless inter-layer condition)

The effect of geometric imperfection Normally, geometric imperfection resulting from the manufacturing process is assumed for design considerations. The parametric study included the geometric imperfection to observe its impact on the structural behavior of SP systems. As seen in Figure 3.21-a, the geometric imperfection of the inner pipe (Imp_1) was fixed at 0.2% and the influence of geometric imperfection of the outer pipe (Imp_3) on the collapse pressure was observed. Figure 3.21-b shows the influence of Imp_1 on the collapse pressure with a fixed Imp_3. As shown, the increase of the geometric imperfection on the steel pipes reduced the ultimate structural strength of the SP system. Note that Imp_1 had a nearly identical influence on the SPs as did Imp_3. Figure 3.22 shows the characteristic responses of the SPs with variations in geometric imperfection. It can be seen that the influence of Imp_3 on the pressure capacity of the SP was almost the same as that of Imp_1. The variation in the geometric imperfection barely changed the capacity to ovalize before collapse of the SP system.

The effect of the steel grade The influence of the steel grade on the ultimate structural strength of SP systems depends on the wall thicknesses. As shown in Figure 3.23, steel grade barely affects the pressure capacity of an SP system when the structure possesses a thin core ($r_1/r_3 = 0.82$) and has a relatively low collapse pressure. Still, using higher-grade steel results in greater ultimate structural strength when the SP has a thick core ($r_1/r_3 = 0.65$). Elastic buckling usually happens to SPs with lower collapse pressure that is associated with a thin sandwich pipe. In this case, the steel pipe stays in the elastic deformation region during the collapse deformation. Since the major difference of the steel grade is the yield stress, which

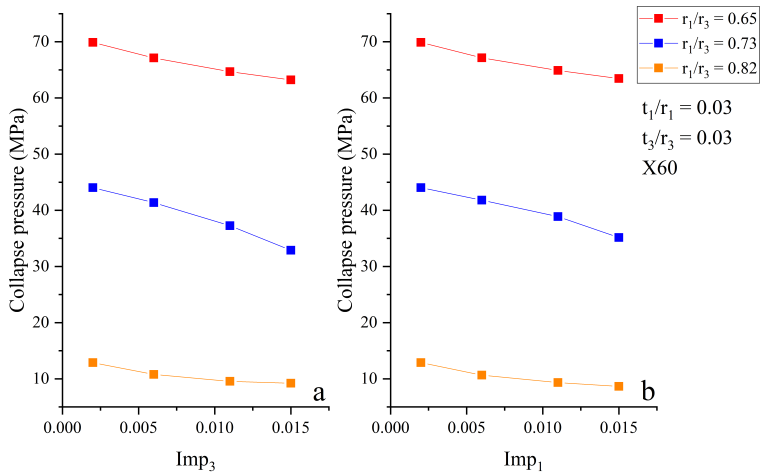

Figure 3.21: Geometric imperfection vs Collapse pressure: (a) SP with $Imp_1 = 0.2\%$; (b) SP with $Imp_3 = 0.2\%$

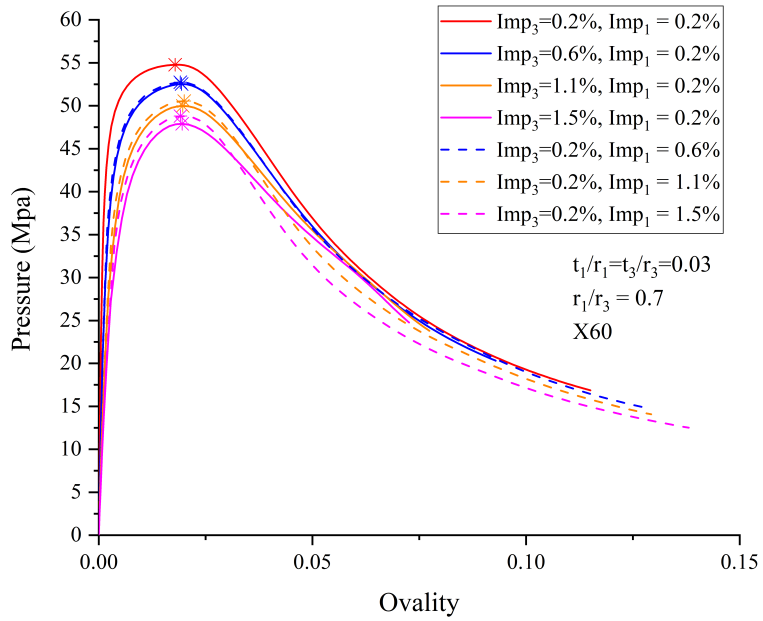

Figure 3.22: Characteristic responses of SPs with different geometric imperfection

does not affect the elastic region, variations in steel grade do not impact the ultimate structural strength of SPs with low collapse pressures.

3.2 A suitable prediction equation

The parametric study found that the effects of some parameters on the collapse pressure are not independent. In other words, the variation in the collapse pressure of the SP with respect to the parameters depends on other parameters. Due to the SP's weak inter-layer adhesion and relatively hard core, the collapse pressure and the characteristic response of an SP with an SHCC core are more relevant to its

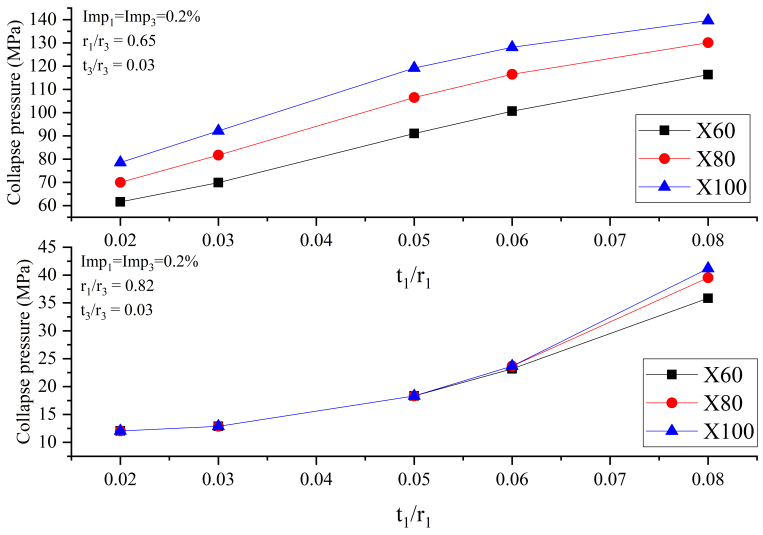

Figure 3.23: Influence of steel grade on the collapse pressures of SPs

strongest layer than to the summation of all the layers. All the existing prediction models for the SP collapse pressure missed this particular collapse behaviour of an SP with an SHCC core. Thus, applying those prediction models may lead to significant deviations. Based on this observation, efforts have been made in this section to develop a prediction equation that can capture the features of an SP with an SHCC core.

3.2.1 Analytical solution

Sato et al. [31] first developed the elastic buckling solution for sandwich pipes. Based on the work by Sato et al. [31], Arjomandi et al. [32] proposed an analytical solution for the collapse pressure of sandwich pipes with a frictionless interlayer condition by letting the shear stress at the boundary equal to zero. Their solutions were presented with details in appendix A and were solved under the MATLAB environment. For verification purposes, the results by both solutions were compared with the experimental data shown in Table 3.5.

As shown, both analytical solutions over predicted the collapse pressure of the SPs. Since both analytical solutions assume a fully elastic core layer, a higher Young's modulus of the core would result in a higher prediction of the collapse pressure. The SHCC core layer has a relatively high Young's modulus (E_c =11410 MPa), which partially explains the higher collapse pressure from the analytical solutions. The analytical solutions could perform better for a sandwich pipe with a softer core layer. To further test the performance of the analytical solutions, the experiments data on the collapse of a sandwich pipe with a polypropylene (PP) core (E_c =1000 MPa) published in Estefen et al.[6] were also used to compare with the analytical solutions, see Table 3.6.

Table 3.5: Comparison between collapse pressures by Sato and Arjomandi with experimental results

Prototype	Imp_3 (%)	Experiment results (MPa)	Sato P_{co} (Mpa) (harmonic number) [fully bounded]	Arjomandi P_{co} (Mpa) (harmonic number) [frictionless]
SP-1A	0.29	37.68	422.98 (n=21)	354.33 (n=21)
SP-2A	0.33	35.96		
SP-3A	0.57	35.23		
SP-4A	0.34	37.18		
SP-5A	0.46	36.92		
SP-1B	0.19	38.71	504.44 (n=21)	427.23 (n=21)
SP-2B	0.5	34.29		
SP-3B	0.57	37.57		
SP-4B	0.4	39.05		

Table 3.6: Comparison between collapse pressures by Sato and Arjomandi with experimental results by Estefen et al. [6]

Prototype	Tubes	Diameter (mm)	Thickness (mm)	Imperfec -tion (%)	P^{*}_{co} (MPa) (mode num- ber)	P^{**}_{co} (MPa) (mode num- ber)	P^{***}_{co} (MPa) (mode num- ber)
PIP.M2. G1.I02	Inner	49.64	1.68	0.456	37.64	115 (n=9)	97.64 (n=9)
	Outer	75.4	1.62	0.301			
PIP.M2. G1.I03	Inner	49.76	1.62	0.186	31.14	114.64 (n=9)	97.25 (n=9)
	Outer	75.19	1.61	0.255			
PIP.M2. G2.I01	Inner	49.94	1.7	0.364	20.31	81.21 (n=2)	59.39 (n=2)
	Outer	62.1	1.46	0.801			
PIP.M2. G2.I02	Inner	50.03	1.69	0.547	17.13	82.115 (n=2)	60.02 (n=2)
	Outer	62.4	1.49	0.552			

P^{*}_{co} - Experimental results; P^{**}_{co} - Results by Sato's solution;
P^{***}_{co} -Results by Arjomandi's solution.

As shown in Tables 3.5 and 3.6, the analytical solutions perform better when the sandwich pipe has a softer core layer (relatively smaller Young's modulus). However, even for lower Young's modulus, significant prediction errors still exist compared to the experimental collapse pressure. The reasons for the analytical solutions over predict the collapse pressure can be summarized below:

- A fully elastic mechanism has been assumed in the analytical predictions not able to detect the failure mechanism for plastic buckling, which is the case for the experimental models.

- No pipe imperfection was introduced in the analytical models characterizing a typical bifurcation elastic failure mode, which is not the case in the experi-

mental models.

- A linear kinematic relation was assumed for the core layer, which can lead to prediction error, as discussed by Hashemian et al. [33, 34].

3.2.2 Empirical solution

As demonstrated in the previous section, the analytical solution is not suitable to predict the SP collapse pressure on a broad range of configurations. Aiming at developing a proper prediction equation for the collapse pressure of SHCC SP, this section is dedicated to improving the prediction accuracy based on extensive simulation results obtained in section 3.1.

Equation forms for training

Since this study focused on the unbonded SP system with an SHCC core, the collapse pressure of the SP is a function of only pipeline geometry and steel material property:

$$P_{co} = F(t_1, r_1, t_3, r_3, Imp_1, Imp_3, \sigma_p) \tag{3.9}$$

The function $F(t_1, r_1 ... \sigma_p)$ is so complex that it must be described in several equations and solved by the finite element method. However, numerical modeling and simulation can be time-consuming when large number of SPs are considered. The purpose of the prediction equation is to develop a direct relationship between the SP parameters and the collapse pressure of the SP.

$$P_{predict} = G(t_1, r_1, t_3, r_3, Imp_1, Imp_3, \sigma_p) \tag{3.10}$$

$$P_{co} - P_{predict} = \varepsilon_{error} \tag{3.11}$$

The prediction of the collapse pressure of a given SP system could be performed if the function $G(t_1, r_1 ... \sigma_p)$ was well defined and the prediction error ε_{error} was small enough. Normally, there are two steps involved in defining $G(t_1, r_1 ... \sigma_p)$. Defining the equation form is the first step, which includes the selection of the equation form from types such as polynomial, trigonometry, exponential, natural logarithm and so on. The arrangement of the variables is also critical in this step. For example, using t_3/r_3 might better represent the outer steel pipe than using t_3 and r_3 separately. With the same data bank and regression techniques, different equation forms can lead to huge differences in terms of accuracy. The second step is to train the unknown parameters in the equations by feeding a large number of examples to the learning algorithm.

In this section, several equation forms (Table 3.7) were selected for comparison purposes. Then, each equation form was trained by machine learning techniques with the data bank acquired from the parametric study. Finally, all the trained equations were evaluated by their performance in terms of prediction accuracy.

A polynomial equation is commonly used in linear regression. The ordinary form of a polynomial equation is:

$$Y = \theta_0 + \theta_1 x_1 ... + \theta_n x_n + \theta_{n+1} x_1^2 + ... + \theta_{2n} x_n^2 + \theta_{(m-1)n+1} x_1^2 + ... \theta_{mn} x_n^2 \quad (3.12a)$$

$$X^T = \left[1, x_1, x_2, ...x_n, x_1^2, x_2^2, ...x_1^m, ...x_n^m\right] \quad (3.12b)$$

$$\theta^T = [\theta_0, \theta_1, ...\theta_{n+1}, \theta_{mn}] \quad (3.12c)$$

The learning features are X^T. The unknown parameters θ^T are determined by minimizing the cost function.

$$J(\theta) = \frac{1}{2} \sum_{j=1}^{S} \left(\theta^T X^{(j)} - P_{co}^{(j)}\right)^2 + \frac{\lambda}{mn} \sum_{i=1}^{mn} \theta_i^2 \quad (3.13)$$

where $\frac{\lambda}{mn} \sum_{i=1}^{mn} \theta_i^2$ is the regularisation term to prevent overfitting, S is the number of training examples, m is the maximum power index of a polynomial equation, n is the number of first-order features of a polynomial equation, and λ is the tuning factor.

The maximum power index m should be determined by the performance of the trained equation on the cross-validation data.

In Table 3.7, Equations (a) and (b) are in polynomial form. The only difference between them is the different arrangement of the learning features.

$$X_{(a)}^T = \left[1, \frac{t_1}{r_1}, \frac{t_3}{r_3}, \frac{r_1}{r_3}, Imp_1, Imp_3, \sigma_p, \frac{t_1}{r_1}^2 ...\sigma_p^2 ... \frac{t_1}{r_1}^m ...\sigma_p^m\right] \quad (3.14)$$

$$X_{(b)}^T = [1, x_1, x_2, x_3 ... x_1^m, x_2^m, x_3^m] \quad (3.15a)$$

$$x_1 = \sigma_p \frac{t_3}{r_3}(1 - Imp_3); \quad x_2 = \sigma_p \frac{t_1}{r_1}(1 - Imp_1); \quad x_3 = \frac{t_2}{r_c}(1 - Imp_c) \quad (3.15b)$$

Note that Imp_c is the average imperfection of the core layer $Imp_c = (Imp_1 + Imp_3)/2$, and r_c is the average radius of the core layer $Imp_c = (r_1 + r_3)/2$.

Like Equation 3.14, Equation (a) treated every variable in the parametric study as a feature, which is the basic application of polynomial regression. On the other hand, Equation (b) rearranged those variables to form three principal features. As shown in Equation 3.15, each feature is composed of the variables of a specific layer

of the SP system. This arrangement is inspired by the analytical solution, in which t_i and r_i always appear together as $\frac{t_i}{r_i}$, and the fact that each layer of the SP contributes to the structural strength of the entire system.

Applying the same idea of the variable arrangement but to a different equation form, Equation (c) also grouped the variables of each layer into a single term that represents the strength of the corresponding layer. To have more flexibility in the equation, the exponential index of each variable was not fixed to an integer, as in the polynomial equation, but was considered an unknown constant, which was trained by the learning algorithm.

Equation (d) was proposed based on the structure of Equation (c) since it shows good accuracy, as shown in a later discussion. As an attempt to improve the performance of Equation (c), modifications were made to Equation (c) to form Equation (d), which was inspired by an observation in the parametric study of section 3.1.

Equation (c):

$$P_{co} = \theta_0 + \theta_1(\sigma_p)^{\theta_2}\left(\frac{t_3}{r_3}\right)^{\theta_3}(1-Imp_3)^{\theta_4} + \theta_5(\sigma_p)^{\theta_6}\left(\frac{t_1}{r_1}\right)^{\theta_7}(1-Imp_1)^{\theta_8} + \theta_9\left(\frac{t_2}{r_c}\right)^{\theta_{10}}(1-Imp_c)^{\theta_{11}}$$

Equation (d):

$$P_{co} = \theta_0 + \left[\theta_1\left(\frac{t_3}{r_3}\right)^{(\theta_5+\theta_6\frac{t_2}{r_c})}(1-Imp_3)^{\theta_7} + \theta_8\left(\frac{t_1}{r_1}\right)^{(\theta_9+\theta_{10}\frac{t_2}{r_c})}(1-Imp_1)^{\theta_{11}}\right] \times (\sigma_p)^{(\theta_2\frac{t_3}{r_3}+\theta_3\frac{t_1}{r_1}+\theta_4\frac{t_2}{r_c})} + \theta_{12}\left(\frac{t_2}{r_c}\right)^{(\theta_{13}+\theta_{14}\frac{t_2}{r_c})}(1-Imp_c)^{\theta_{15}}$$

As observed in the parametric study, the influences of t_1/r_1 and t_3/r_3 on the P_{co} of the SP are not independent. The core thickness (t_2/r_c) also has an impact on the variation in P_{co} with respect to t_1/r_1 or t_3/r_3 (see Figures 3.9 and 3.18). In order to capture this behaviour, the exponential indexes of t_1/r_1 and t_3/r_3 were changed from θ_i in Equation (c) to $\theta_i + \theta_{i+1}\frac{t_2}{r_c}$ in Equation (d). This same modification was made to t_2/r_c to have more flexibility in the equation. Except for the strengths of all layers, the P_{co} of the SP with the frictionless inter-layer condition is also a result of the interactions between all layers. Equation (d) can achieve a better approximation of this fact by adding the term $\theta_{i+1}\frac{t_2}{r_c}$ to the exponential indexes of t_1/r_1, t_3/r_3 and t_2/r_c. For some SP configurations, the difference in steel yield stress σ_p barely impacts the P_{co} of the SP while the steel layers experience elastic buckling

(see Figure 3.23). The three parameters t_1/r_1, t_3/r_3 and t_2/r_c mainly determine whether the SP will have elastic or plastic buckling. Therefore, the impact of σ_p in the equation should be relevant to t_1/r_1, t_3/r_3 and t_2/r_c. With this observation, the exponential index θ_i of σ_p in Equation (c) was changed into $\theta_i \frac{t_3}{r_3} + \theta_{i+1} \frac{t_1}{r_1} + \theta_{i+2} \frac{t_2}{r_c}$ in Equation (d). The same term $(\sigma_p)^{(\theta_2 \frac{t_3}{r_3} + \theta_3 \frac{t_1}{r_1} + \theta_4 \frac{t_2}{r_c})}$, representing the yield stress, was used for both terms representing the inner and outer pipes to reduce the complexity of the equation.

In addition to the equation forms proposed by the thesis, three equation forms proposed by previous researchers were included for comparison. Since some characteristics of the SP, such as the imperfection and inter-layer condition, are different among researches, the previous equation forms were slightly modified to suit the SP in this study. Equation (e) is proposed by Gong et al. in their research on the buckle propagation pressure [49]. It considers the structural strength of the SP as the enhancement based on the strength of the outer steel pipe. The variables of the inner pipe and the core layer were arranged in a power-law form. Note that the original equation by Gong et al. was for the buckle propagation pressure of an SP without imperfection. The initial ovality and the collapse pressure of the outer steel pipe were included in Equation (e) of this study. Equation (f) was proposed by He et al. [45] as they focused on the prediction of an SP with a PP core. Taheri et al. [10, 43, 44] applied two equation forms trying to provide equations that can predict the collapse pressure of SPs with different core materials. One of the equations is very similar to the one proposed by He et al. [45]. Therefore, only one equation from the work by Taheri et al. [43] was used to inspire Equation (g), in which the initial ovality was added to the original equation.

The above equation forms proposed by researchers were all, to some extent, based on the physical background. The equation forms were created trying to mimic the mechanism underlying the physical process. However, one cannot ensure that the equation form with the best performance among them can provide a prediction with minimum error. The fact is that a large amount of equation forms have not been tested yet. Therefore, the automatic machine learning software EUREQA [115, 116] was employed to expand the search area. Given a data bank, the software is able to automatically search for equations that better fit the data and thus acquire higher prediction accuracy. In this work, the software operated for 262 hours (CPU: 4 Intel cores with 3.60 GHz). The equation with the best fitness among all the equations tested was selected for the comparison study.

Note that the unknown constants in all the equations shown in Table 3.7 are expressed as $\theta^T = [\theta_0, \theta_1, \theta_2, \theta_3 ...]$. These unknown parameters were determined by applying a regression algorithm to a large data set from the parametric study.

Table 3.7: Summary of all the equation forms tested.

Type	Equation form	Equation number
Proposed by the thesis	$P_{predict} = \theta_0 + \theta_1 {t_3}/{r_3} + \theta_2 {t_1}/{r_1} + \theta_3 {r_1}/{r_3} + \theta_4 Imp_3 + \theta_5 Imp_1 + \theta_6 \sigma_p$ $\theta_7 \left({t_3}/{r_3}\right)^2 + ... \theta_{12} {\sigma_p}^2 + ... \theta_{n-5} \left({t_3}/{r_3}\right)^m + ... \theta_n {\sigma_p}^m$	(a)
	$P_{predict} = \theta_0 + \theta_1 x_1 + ... \theta_3 x_3 + \theta_4 {x_1}^2 + .. \theta_6 x_3^2 + ... \theta_{n-2} x_1^m + ... \theta_n x_3^m$ $\mathrm{x}_1 = \sigma_p {t_3}/{r_3} 1 - imp_3; \quad \mathrm{x}_2 = \sigma_p {t_1}/{r_1} 1 - imp_1; \quad \mathrm{x}_3 = {t_2}/{r_c} 1 - imp_c$	(b)
	$P_{predict} = \theta_0 + \theta_1 (\sigma_p)^{\theta_2} (\frac{t_3}{r_3})^{\theta_3} (1 - imp_3)^{\theta_4} + \theta_5 (\sigma_p)^{\theta_6} (\frac{t_1}{r_1})^{\theta_7} (1 - imp_1)^{\theta_8}$ $+ \theta_9 (\frac{t_2}{r_c})^{\theta_{10}} (1 - imp_c)^{\theta_{11}}$	(c)
	$P_{predict} = \theta_0 + \left[\theta_1 \left(\frac{t_3}{r_3}\right)^{(\theta_5 + \theta_6 \frac{t_2}{r_c})} (1 - imp_3)^{\theta_7}\right.$ $\left. + \theta_8 \left(\frac{t_1}{r_1}\right)^{(\theta_9 + \theta_{10} \frac{t_2}{r_c})} (1 - imp_1)^{\theta_{11}}\right] \times (\sigma_p)^{(\theta_2 \frac{t_3}{r_3} + \theta_3 \frac{t_1}{r_1} + \theta_4 \frac{t_2}{r_c})}$ $+ \theta_{12} \left(\frac{t_2}{r_c}\right)^{(\theta_{13} + \theta_{14} \frac{t_2}{r_c})} (1 - imp_c)^{\theta_{15}}$	(d)
By Gong et al. [49]	$\frac{P_{predict}}{Min(P_{El}, P_{Pl})} = 1 + \theta_0 (\frac{t_3}{r_3})^{\theta_1} (\frac{r_1}{r_3})^{\theta_2} (\frac{t_1}{t_3})^{\theta_3} (\frac{\sigma_p}{E_p})^{\theta_4} {imp_3}^{\theta_5} {imp_1}^{\theta_6}$ $\mathrm{P}_{El} = 2 \frac{E_p}{1 - v^2} (\frac{t_3}{2 r_3})^3 \qquad \mathrm{P}_{pl} = \sigma_p \frac{t_3}{r_3}$	(e)
By He et al. [45]	$\frac{P_{predict}}{E_p} = \theta_0 \frac{t_3}{r_3})^{\theta_1} (\frac{r_1}{r_3})^{\theta_2} (\frac{t_1}{r_1})^{\theta_3} (\frac{\sigma_p}{E_p})^{\theta_4} + \theta_5 \frac{t_3}{r_3})^{\theta_6} (\frac{r_1}{r_3})^{\theta_7}$ $\times (\frac{t_1}{r_1})^{\theta_8} (\frac{\sigma_p}{E_p})^{\theta_9} {imp_3}^{\theta_{10}} + \theta_{11} \frac{t_3}{r_3})^{\theta_{12}} (\frac{r_1}{r_3})^{\theta_{13}} (\frac{t_1}{r_1})^{\theta_{14}} {imp_1}^{\theta_{15}}$	(f)
By Taheri et al. [10]	$P_{predict} = \theta_0 P_{El} (\frac{\sigma_p}{E_p})^{\theta_1} {imp_3}^{\theta_2} + (1 + \theta_3) (\frac{t_3}{r_3})^{\theta_4} (\psi_1 + \psi_2)$ $\mathrm{P}_{El} = 2 \frac{E_p}{1 - v^2} (\frac{t_3}{2 r_3})^3 \qquad \psi_1 = \theta_5 (1 - \frac{r_1}{r_3})^{\theta_6}$ $\psi_2 = \theta_7 (1 - \frac{r_1}{r_3})^{\theta_8} (\frac{t_1}{r_1})^{\theta_9} (\frac{\sigma_p}{E_p})^{\theta_{10}} {imp_1}^{\theta_{11}}$	(g)
Optimised by EUREQA	$P_{predict} = \left(\frac{r_1}{r_3}\right) \left(\frac{t_1}{r_1}\right)^{\left[3.66 + \left(\frac{r_1}{r_3}\right)\right]} + 7.09 \left(\frac{t_3}{r_3}\right)^{\left[1 + \left(\frac{r_1}{r_3}\right)\right]} \max \left[\left(\frac{t_3}{r_3}\right) \left(\frac{r_1}{r_3}\right)\right]$ $+ \frac{705 + 59.5 \left(\frac{t_1}{r_1}\right) + 59.5 \left(\frac{r_1}{r_3}\right) \left(\frac{\sigma_p}{E_p}\right)}{\left(\frac{t_3}{r_3}\right) + imp_1 + 6.53 \left(\frac{r_1}{r_3}\right) + \left(\frac{t_3}{r_3}\right) imp_3} - 59.5$	(h)

Methodologies used in the regression process

To find the best prediction performance, appropriate techniques should be carefully chosen to search for the unknown constants $\theta^T = [\theta_0, \theta_1, \theta_2, \theta_3 ...]$ in the proposed

equation forms. Here, machine learning techniques [119] were applied in the regression process. The 6000 simulation results from the parametric study were randomly divided into three parts: 4200 results (70%) for the training data set, 1200 results (20%) for the cross-validation data set, and 600 (10%) for the test data set. The training data set was fed into the regression algorithm. The cross-validation data set was used to determine some critical parameters in the equation, for instance, the highest order in the polynomial equation or the penalty factor for preventing overfitting. The prediction accuracies of the trained equations were evaluated on the test data set, with the maximum ($\varepsilon_{\max}$), average ($\varepsilon_{average}$) and minimum errors ($\varepsilon_{\min}$) defined as:

$$\begin{aligned} &\varepsilon_j = \frac{\left|P^j_{predict} - P^j_{co}\right|}{P^j_{co}},\ \text{j = 1,2,3....S}_{test} \\ &\varepsilon_{\max} = Max(\varepsilon); \quad \varepsilon_{average} = \frac{1}{k_{test}} \sum_{j=1}^{k_{test}} \varepsilon_j; \quad \varepsilon_{\min} = Min(\varepsilon) \end{aligned} \tag{3.16}$$

Note S_{test} is the number of the testing examples.

The training features have different magnitudes, which slows down the search speed. Thus, feature scaling was employed to pre-process the features to accelerate the search speed:

$$X = \frac{X - Min(X)}{Max(X) - Min(X)} + 0.5 \tag{3.17}$$

where X represents a vector composed of all the data samples of one variable in each equation. The features were arranged differently in the proposed equations. Therefore, the form of X varies for different equations. But all the features were pre-processed with feature scaling by Equation 3.17.

The determination of the unknown constants (θ^T=$[\theta_0, \theta_1, \theta_2, \theta_3....\theta_{tal}]$) can be treated as an unconstrained optimization problem with the aim of finding the global minimum of the cost function for each proposed equation, as expressed in Equation 3.18.

$$J(\theta) = \frac{1}{2} \sum_{j=1}^{S} ({P_{predict}}^{(j)} - {P_{co}}^{(j)})^2 + \frac{\lambda}{tal} \sum_{i=1}^{tal} \theta_i^2 \tag{3.18}$$

First, the minimization algorithm based on the Polack-Ribiere method of conjugate gradients [119] was employed for the search task. However, the algorithm was easily trapped in a pseudo-minimum when high search dimensions were encountered in some of the proposed equations. This problem is inevitable when the cost function is not convex. The particle swarm optimization (PSO) method [102], which works without gradient information, was also employed for the search task. Nevertheless,

the weak exploration capacity of the canonical PSO was also exposed in this high-dimensional search problem. Making efforts to find the global minimum is critical not only for fully extricating the prediction potential of each proposed equation but also for a fair comparison of the proposed equations. Several PSO variants, such as LPSO, CPSO [120], CPSOH [120], SLPSO [121], ELPSO [122], FIPSO [123] and MLPSO [124], were tested for each proposed equation. Also, the penalty factor was carefully adjusted to prevent overfitting for some equations when necessary. To illustrate the selection process of the proper optimiser and the relevant parameters involved would require a large number of figures. Since it is not the focus of this study, the results of this step are not shown for the sake of conciseness. The best result for each proposed equation among the results found by all the optimisers was saved for the evaluation process.

Evaluation of the trained equations and discussion

Accuracy is the principal criterion for the prediction evaluation. The prediction performances of all trained equations were evaluated on the test data set, with the errors defined by Equation 3.16.

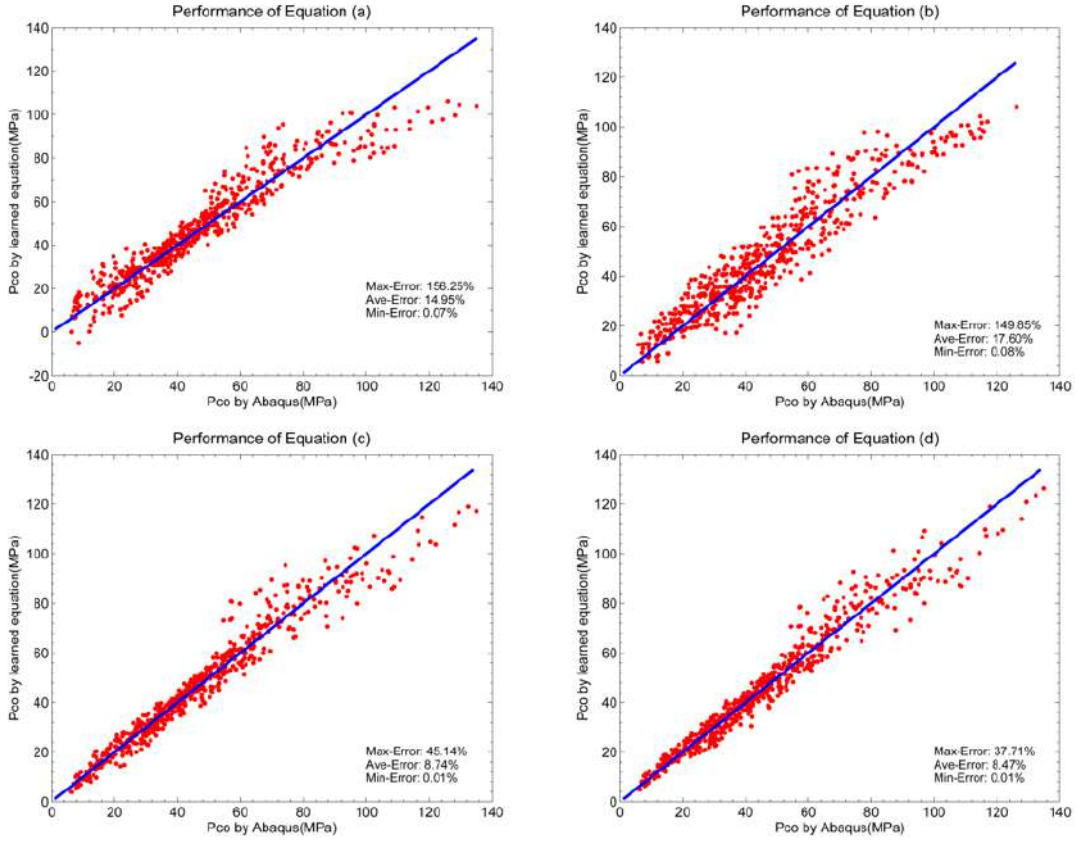

Figure 3.24: The prediction accuracies of the trained equations proposed in the thesis.

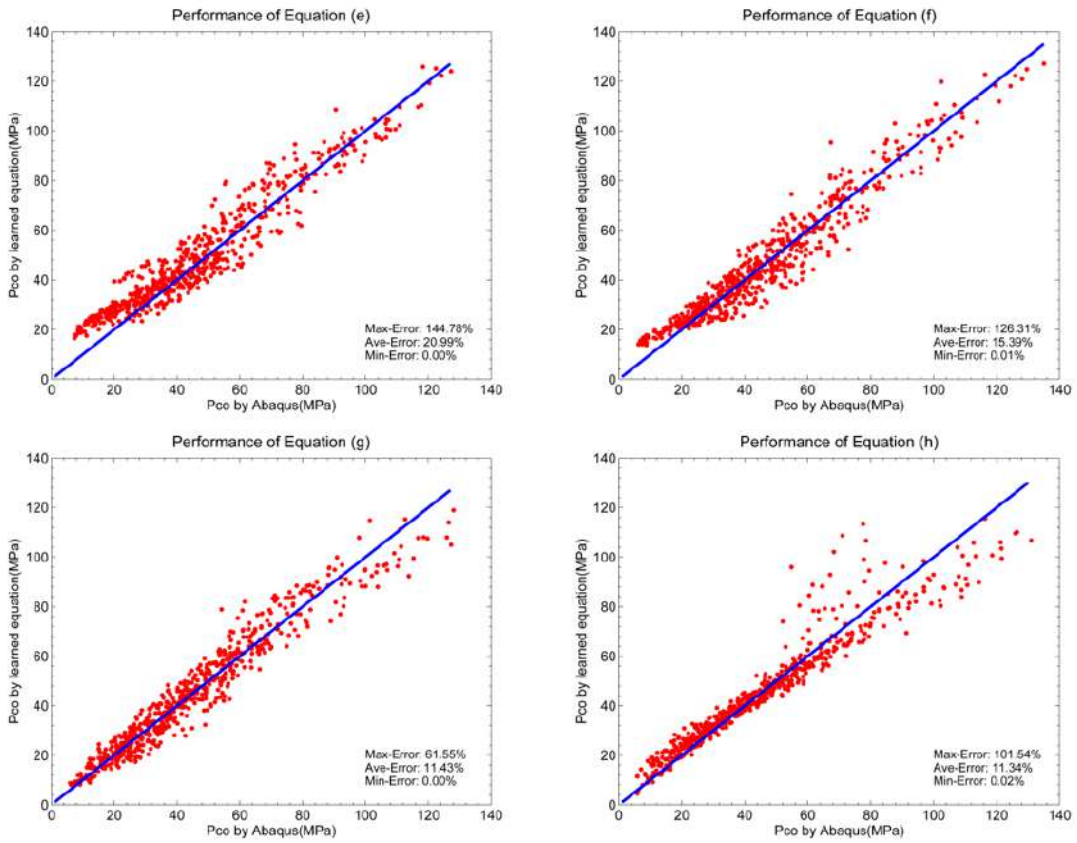

Figure 3.25: The prediction accuracies of the trained equations proposed by previous researchers and by EUREQA.

Figures 3.24 and 3.25 show the prediction performances of all the proposed equations. Equations organized in a polynomial form, such as Equations (a) and (b), are not suitable for the problem since their maximum prediction errors reach 156.25% and 149.55%, with average prediction errors of 14.95% and 17.6%. Equation (c) proposed in the thesis shows a good accuracy, with a maximum prediction error of 45.14% and an average error of 8.74%. Moreover, its enhanced version, Equation (d), shows the best performance among all the equations, with a maximum error of 37.71% and an average error of 8.47%. Since it was originally proposed for the estimation of the buckling propagation of SPs, Equation (e) provided by Gong et al. [49] performs inadequately, with 144.78% of the maximum prediction error and 20.99% of the average prediction error. Even though it was proposed for collapse pressure estimation, Equation (f) suggested by He et al. [45] barely shows an improvement in accuracy since its maximum and average errors are 126.31% and 15.39%. Equation (g) suggested by Taheri et al. [43] has the best performance among the equations provided by previous researchers, with a maximum prediction error of 61.55% and an average prediction error of 11.43%. Within the operational hours, Equation (h) was the best equation found by the EUREQA software. It gives a prediction with a maximum error of 101.54% and an average error of 11.34%.

As discussed in the parametric study, the variation in P_{co} of an SP with SHCC material and a frictionless inter-layer condition is more complex than that of an SP with a fully bonded inter-layer condition. It has been observed that the P_{co} of an SP with SHCC is related to the interaction between the layers as well as the sum of the strengths of all the layers. Also, the steel grade barely makes a difference to the P_{co} when the SP experiences elastic buckling. The polynomial form equation failed to make accurate predictions due to its simplicity. The previous equations also perform inadequately since they were not designed to capture the complex behaviour of an SP with an SHCC core. The EUREQA software is capable of fitting the data by automatically testing many different equation forms. The application of EUREQA can help researchers to test new equations outside the physical background box. However, within the operational time of EUREQA, the best equation found by EUREQA failed to give the best prediction performance due to both problem complexity and the enormous search space. Based on an insightful understanding of the physical background and the P_{co} variation observed in the parametric study, Equation (d) proposed in this work outperforms all the equations tested and accurately predicts the P_{co} of an SP with an SHCC core.

Pros and cons of Equation (d)

Figure 3.26 illustrates the advantage of Equation (d), which manages to capture the complex behaviour shown in Figure 3.9. With different core thicknesses, Equation (d) gives different P_{co} variation with respect to t_3/r_3.

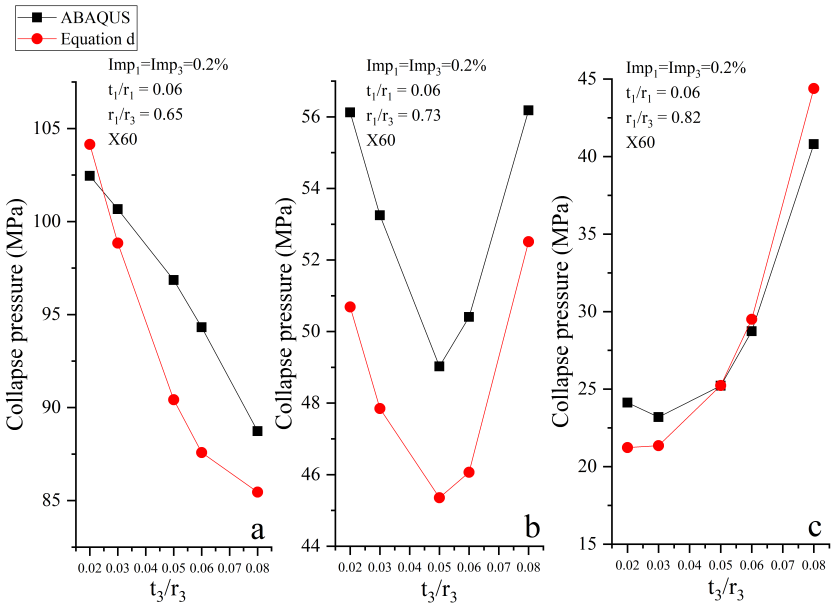

Figure 3.26: P_{co} with respect to t_3/r_3 by ABAQUS vs Equation (d): (a) thick core ($r_1/r_3 = 0.65$), (b) moderate core ($r_1/r_3 = 0.73$), and (c) thin core ($r_1/r_3 = 0.82$).

For a safe application of Equation (d), it is critical to discuss the SP configura-

tions in which Equation (d) shows a relatively large prediction error. It was observed that there are two areas in which Equation (d) fails to predict P_{co} accurately. First, when the P_{co} of the SP is relatively small (below 15 MPa), the equation is likely to over-predict P_{co} for an SP with high steel grade. Table 3.8 shows some typical SP configurations in which Equation (d) over-predicts P_{co}. As shown, SPs with large imperfection and thin layers tend to experience elastic buckling, which makes P_{co} independent to the steel grade. Even though Equation (d) was specially modified to decrease the error caused by different buckling mechanisms, it still over-predicts the P_{co} for SPs with X80 and X100 for the elastic buckling case.

Table 3.8: Prediction error and SP configurations

Steel type	t_3/r_3	t_1/r_1	r_1/r_3	$Imp_3(\%)$	$Imp_1(\%)$	P_{co} ABAQUS (MPa)	P_{co} equation (d)	Prediction error (%)
X60	0.03	0.03	0.82	1.1	1.1	7.53	8.09	7.42
X80	0.03	0.03	0.82	1.1	1.1	7.53	9.49	**25.93**
X100	0.03	0.03	0.82	1.1	1.1	7.53	10.38	**37.71**
X60	0.03	0.05	0.82	1.1	1.1	11.72	13.04	11.27
X80	0.03	0.05	0.82	1.1	1.1	12.18	14.94	**22.66**
X100	0.03	0.05	0.82	1.1	1.1	12.39	16.13	**30.12**
X60	0.03	0.05	0.82	1.5	1.1	11.2	12.25	9.34
X80	0.03	0.05	0.82	1.5	1.1	12.09	14.08	**16.41**
X100	0.03	0.05	0.82	1.5	1.1	12.36	15.23	**23.16**

Equation (d) also performs inadequately when the SP has a thick core ($r_1/r_3 = 0.65$) and a thin steel layer ($t_3/r_3 \leq 0.03$,$t_1/r_1 \leq 0.03$). Table 3.9 shows the typical SP configurations in which Equation (d) over-predicts P_{co}. The failure of Equation (d) for these SP configurations is caused by the sudden change in the variation tendency of P_{co} with respect to t_3/r_3 when t_1/r_1 is below 0.03 (see Figure 3.9-a). This failure shows that Equation (d) is not capable of capturing all the complex behaviours of the P_{co} variation of an SP with SHCC. Therefore, the relatively large prediction error should be noted when the trained Equation (d) is applied to an SP with a thick core ($r_1/r_3 = 0.65$) and a thin steel layer ($t_3/r_3 \leq 0.03$,$t_1/r_1 \leq 0.03$).

Data of SP collapse experiments from An et al. [19] and the experimental data in this thesis were compared to the equation (d). Note that only the data of experiments on SPs with SHCC core were collected for the comparison (See Figure 3.27).

As shown, the collapse pressures given by equation (d) are lower than the experimental results. It is mainly because that equation (d) was proposed conservatively assuming a frictionless inter-layer adhesion. And friction exists in the actual SHCC SP. For a fair comparison, the prediction by equation (d) should be multiplied by a

Table 3.9: Prediction error and SP configurations

Steel type	t_3/r_3	t_1/r_1	r_1/r_3	$Imp_3(\%)$	$Imp_1(\%)$	Pco-ABAQUS (MPa)	Pco-equation (d)	Prediction error (%)
X60	0.03	0.02	0.65	1.1	0.2	57.11	78.44	37.36
X60	0.03	0.02	0.65	0.2	1.1	57.35	78.64	37.12
X60	0.03	0.02	0.65	1.5	0.6	54.53	70.71	29.68
X60	0.02	0.03	0.65	1.1	1.1	59.77	76.18	27.45
X80	0.03	0.02	0.65	0.2	0.2	70	88.28	26.11
X60	0.03	0.03	0.65	0.6	0.6	64.88	81.5	25.62
X100	0.02	0.02	0.65	1.5	0.2	66.2	82.86	25.17

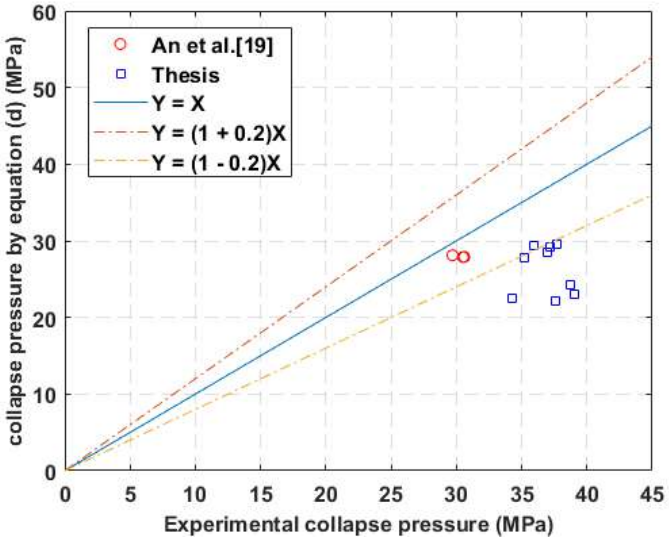

Figure 3.27: Experimental test versus Equation (d)

coefficient considering the inter-layer friction effect.

For SP with SS304, which has a smooth surface, Figure 3.6 shows that the ratio between experimental collapse pressure and the collapse pressure of SPs with frictionless condition is around 1.15. For SP with SS316, which has a rough surface, Figure 3.7 shows that the collapse pressure ratio is around 1.4. Based on this observation, the prediction results by equation (d) were multiplied by 1.15 for the SPs with SS304 and 1.4 for the SPs with SS316. As shown in Figure 3.28, a good correlation between the experiments and the modified results of the equation (d) was achieved.

It should be emphasized that equation (d) was developed conservatively assuming a frictionless condition. The correlation between the experimental data and the results by equation (d) shows that a coefficient can be multiplied to the equation (d) when actual inter-layer condition has to be included. This coefficient is 1.15 for steel pipes with smooth surface (SS304) and is 1.4 for steel pipes with rough surface

(SS316).

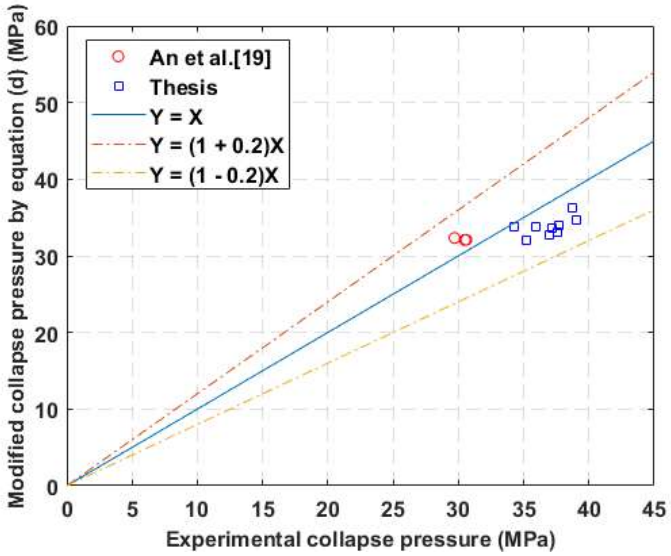

Figure 3.28: Experimental test versus modified results by Equation (d)

Trained parameters for Equation (d)

Fortunately, the two areas in which Equation (d) predicts with relatively larger errors are not the areas of design interest. Usually, the water depth for SP applications varies from 1500 to 3000 meters, which is an area (15 to 30 Mpa) in which Equation (d) performs well. The trained constants for Equation (d) are listed in Table 3.10.

Table 3.10: The trained constants for Equation (d).

θ_0	θ_1	θ_2	θ_3	θ_4	θ_5	θ_6	θ_7
-5.8433	7.65762	-0.0226	-0.0877	0.42328	3.24046	-0.6458	0.56457
θ_8	θ_9	θ_{10}	θ_{11}	θ_{12}	θ_{13}	θ_{14}	θ_{15}
14.115	0.72154	0.8829	0.36618	23.4687	4.2532	-0.7719	0.29961

Note that feature scaling was employed for the training process. Therefore, the same data processing should be conducted before applying Equation (d). Feature scaling is expressed in Equation 3.17. The corresponding parameters and features for Equation (d) are listed in Table 3.11. It is noteworthy to point that the safe parametric ranges of application of Equation (d) are the ranges listed in Table 3.11. The prediction accuracy of the collapse pressure of a SP with parameters outside of safe parametric ranges by Equation (d) was not evaluated. It is because the

parametric ranges we selected almost cover the whole design area of a sandwich pipe for deep water application.

Table 3.11: Parameters used for the feature scaling for Equation (d).

Features	Minimum value	Maximum value
σ_p	415	690
t_3/r_3	0.02	0.08
$1 - Imp_3$	0.985	0.998
t_1/r_1	0.02	0.08
$1 - Imp_1$	0.985	0.998
t_2/r_c	0.11	0.4
$1 - Imp_c$	0.985	0.998

3.3 Summary

This chapter involved a comprehensive study on SPs with SHCC cores that incorporated experiments and parametric study. Efforts have been made to search for a suitable prediction equation of the SHCC SP collapse pressure. The conclusions are as follows:

(1) A large-scale parametric study on the P_{co} of SPs with SHCC cores was conducted by varying, in the practical range, the three layers' thicknesses, geometric imperfections, and steel grades. The frictionless inter-layer condition was adopted to better represent the actual situation. As observed in Figures 3.9 and 3.18, the influence of the thickness of each layer on P_{co} is not independent. The variation tendency of P_{co} with respect to thickness of one layer changes with different combinations of the other layers' thicknesses shows that the P_{co} of SPs with SHCC cores is a result of interactions between layers that are more complex than a simple summation.

(2) The study on the effect of t_3/r_3 on the P_{co} of the SHCC SP revealed that the P_{co} decreases, in some cases, with increases of t_3/r_3. This counterintuitive phenomenon was carefully investigated with the SP configurations listed in Table 3.4. Because of the outside radius setting (Figure 3.10), an increase of t_3/r_3 means a thicker outer steel layer and a thinner core layer (Figure 3.11). Thus, as the t_3/r_3 increases, the strength of the outer steel layer increases and that of the core layer decreases. As a result, the strength of the strongest layer of an SP first decreases and increases later, while the strongest layer of the SP shifts from the core layer to the outer steel layer (Figure 3.12). Interestingly, the P_{co} of the whole SP system showed the same variation as that of the strongest layer of the SP. Further, the characteristic response of the SP is similar to that of the strongest layer, showing more capacity to ovalize before collapse when the core layer is strongest and less capacity to ovalize

before collapse when the strongest layer shifts to the outer steel layer (Figures 3.13 and 3.14). The ultimate structural strength and characteristic response of an SP seem to be dominated by its strongest layer. The transition of the dominating layer from the core to the outer steel layer explains the observed counterintuitive phenomenon. This behavior disappeared when the inter-layer condition was changed from frictionless to fully bonded (Figure 3.15). The same behavior has never been reported in previous studies, since SPs with PP cores have the fully bonded inter-layer condition and low core layer stiffness. Therefore, the behavior first reported in this work is unique to SPs with weak inter-layer adhesion and high stiffness of the core layer, such as SPs with SHCC cores.

(3) Figures 3.16 and 3.17 show that SPs with thinner steel layers are more efficient at utilizing the strength of the core layer by having it experience higher plastic strain and stress at the collapse state. The observation is important for efficient SP design; however, corrosion allowance must be considered.

(4) In an effort to propose a quick and accurate prediction of the P_{co} of an SP, eight equation forms were trained and evaluated. For a scientific evaluation, 6000 data points were separated into training data (70%), cross-validation data (20%) and testing data (10%). Due to the complex behaviour observed in the parametric study, the equations proposed by previous researchers as well as the polynomial equations proposed in this study failed to predict P_{co} accurately. Large prediction errors were found in the evaluation process. By grouping the variables of each layer into an exponential constant, Equation (c), which is composed of three parts representing respectively the strengths of each layer, showed a great improvement in prediction accuracy. Further improvement was achieved by Equation (d) by applying terms to Equation (c) mimicking the interaction between the layers and the different collapse models. The superior performance of Equation (d) indicates how to form equations for the P_{co} prediction of SP systems, which is representing the strength of each layer and then adding interaction terms to the equation.

(5) The automatic machine learning software EUREQA was employed to expand the search area in case that better equation forms exist outside of the examined range. Equation (h) is the best result found by EUREQA in 262 hours of operation (CPU: 4 Intel cores with 3.60 GHz). However, inadequate prediction performance was found with a maximum error of 101.54% and an average error of 11.34%. It reflects the difficulties to capture the complex behaviour of the P_{co} of an SP in a huge search area without the guidance of the physical background. On the other hand, the application of EUREQA demonstrates that finding an equation that performs better than Equation (d) may need additional efforts.

(6) Figure 3.26 shows that Equation (d) is able to capture the behavior of transition of the dominating layer of an SP with an SHCC core found in this work.

However, there are two areas in which Equation (d) fails to predict P_{co} accurately. When P_{co} of the SP is relatively small (below 15 MPa), the equation is likely to over-predict the P_{co} of an SP with high steel grade. In addition, the relatively large prediction error should be noted when the trained Equation (d) is applied to an SP with a thick core ($r_1/r_3 = 0.65$) and a thin steel layer ($t_3/r_3 \leq 0.03$,$t_1/r_1 \leq 0.03$). Additional efforts were made to solve the identified weakness of Equation (d). However, the change in the equation triggers other unexpected prediction errors and increases the complexity of the equation. Probably it is not feasible to capture all the types of behaviour with only one equation.

(7) Fortunately, the two areas in which Equation (d) predicts with relatively larger errors are not areas of design interest. Usually, the water depth of SP applications varies from 1500 to 3000 meters, which is an area (15 to 30 MPa) in which Equation (d) performs well. The trained constants were listed for a conceptual design of an SP with an SHCC core.

Chapter 4

Thermal analyses of SP

In addition to the structural strength, the insulation performance in both steady-state and shut-in conditions are critical design requirements of the SP. Comparing to the PP, the SHCC has higher thermal conductivity. Thus, the PP SP should outperform the SHCC SP in terms of thermal insulation. This chapter first evaluated the insulation performance of the SHCC SP using the software OLGA. Based on the results, the relationship between the volumetric heat capacity (VHC) of the SP core layer material and the insulation performance of the SP was discussed, which demonstrated that an integrated optimal design of the SP is critical to exploiting the efficiency of the SP fully. Then, a mathematical model for the heat transfer analysis in an SP was developed, which was employed for the SP optimization in Chapter 5.

4.1 Insulation performance of the SHCC SP

In order to comprehensively evaluate the insulation capacity of the SHCC SP, a case study was conducted on a subsea production system with water depth at two thousand and two hundred meters. First, structural configurations were designed for scenarios using the SHCC SP, the SW, the PIP, and the flexible pipe (FP). Then, thermal analyses for each scenario were carried out for both steady-state and shut-in working conditions.

4.1.1 Subsea production system and pipeline geometry

The subsea production system is composed of twelve production wells, two cluster manifolds (A1 and A2), and one FPSO (Figure 4.1). Each cluster manifold is connected to six production wells. For each cluster manifold, the distances from the manifold to the wellheads are equal. For a comparison study, a long pipeline was set for Cluster A1 while a short pipeline was set for Cluster A2. The pipeline lengths

and diameters are shown in Table 4.1.

Using out-of-roundness 1%, 0.85 for fabrication factor and medium safety class, the wall thickness for the SW was defined by DNV code [125]. Collapse and buckling propagation were used as design criteria. Internal design pressure was set as 280 bars for all pipeline designs. For the PIP design, the method proposed by [13] was employed where the design U-value was set as 1 $W/m^2.K$. For the SP design, 3 mm was assumed for the thickness for both inner and outer steel layers, and the SHCC core layer thickness was increased until the SP meets the structural requirement, which is the required collapse pressure. Finite element analysis was carried out by the Abaqus software to obtain the SP configuration. The pipeline configurations are shown in Table 4.2.

Polyurethane foam (PUF) was used as the insulation material in the core layer of the PIP. The flexible pipe is actually composed of several layers which provide different functions. For an insulation study, those layers were simplified as one composite layer with uniform thermal properties. In the following study, when the SP, SW and FP were not capable of meeting the insulation requirement, an extra insulation layer would be applied on their outside surface. Table 4.3 shows the properties of the insulation layer.

The heat transfer in the pipeline is a two-dimensional problem. In the axial direction of the pipe, the maximum step length for the pipeline was set to 100 m. A small step length (30 m) was set for the riser as the temperature and pressure change more frequently in the riser. In the radial direction, as for the wall layer thickness setting, the change in thickness (Δth), between two neighbouring layers was restrict to $0.2 \leq \Delta th\,(i)\,/\Delta th\,(i-1) \leq 5$.

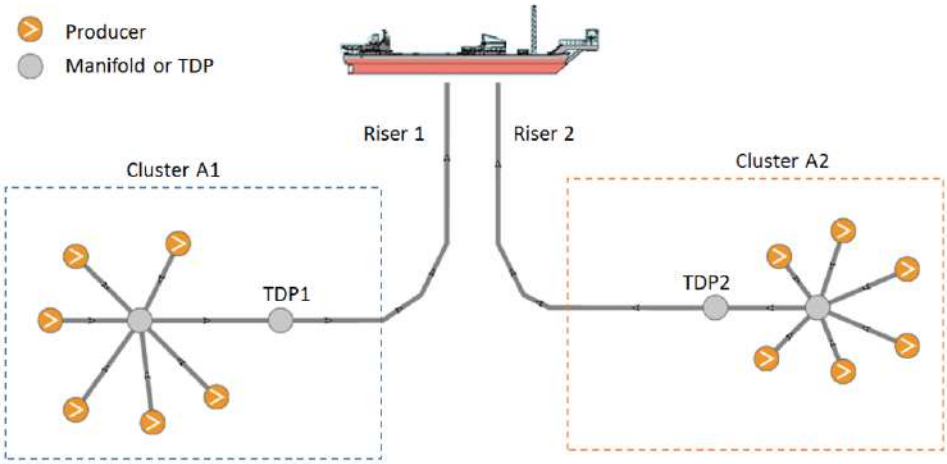

Figure 4.1: Subsea production system

Table 4.1: Subsea pipeline lengths

Pipeline location	Pipeline from wellhead to manifold	
Pipeline geometry	Length (m)	Innermost Diameter (inch)
Cluster A1	1200	4
Cluster A2	600	4
Pipeline location	Pipeline from manifold to TDP	
Pipeline geometry	Length (m)	Innermost Diameter (inch)
Cluster A1	9500	8
Cluster A2	1100	8
Pipeline location	Riser	
Pipeline geometry	Length (m)	Innermost Diameter (inch)
Cluster A1	3000	8
Cluster A2	3000	8

Table 4.2: Subsea pipeline configurations

Type	Innermost diameter (inch)	Layer	Wall thick-ness(mm)	Material	ρ (kg/m^3)	c (J/(kg.K))	k (W/(m.K))
SP	Inner steel layer		3	Steel	7850	500	50
	4	Core	15	SHCC	1473	880	0.28
	8		31				
	Outer steel layer		3	Steel	7850	500	50
PIP	4	Inner	5	Steel	7850	500	50
		Core	20	PUF	30	1500	0.025
		Outer	7	Steel	7850	500	50
	8	Inner	9.9	Steel	7850	500	50
		Core	21	PUF	30	1500	0.025
		Outer	13	Steel	7850	500	50
SW	4	-	5.5	Steel	7850	500	50
	8	-	10.5				
FP	4	Composite layer	24.7	Composites	3933.5	1000	10.39
	8	Composite layer	37.4	Composites	3794.8	1000	9.95

Table 4.3: Properties of the insulation material

Material	ρ (kg/m^3)	c (J/(kg.K))	k (W/(m.K))
Synthetic polypropylene	1040	1220	0.16

4.1.2 Flow assurance analyses

Two insulation requirements were applied: 1. In the steady-state condition, the temperature of the whole production system is kept beyond wax appearance temperature (WAT); 2. in shut-in condition, the required cool-down time is 8 hours before the precipitation of any depositions.

59.5 ℃ was the temperature for all wellheads and the flow rate at the wellhead was 8000 bbl/day (18 kg/s). The pressure at FPSO was set as 30 bars. Using the OLGA software, steady-state simulations were carried out to simulate the normal working condition. The pressure and temperature curves of the whole production system were compared with the critical curves of wax and hydrate formation (Figures 4.2 and 4.3). Only the insulation configurations that keep the system stay at the safe region and require minimum insulation thickness are shown.

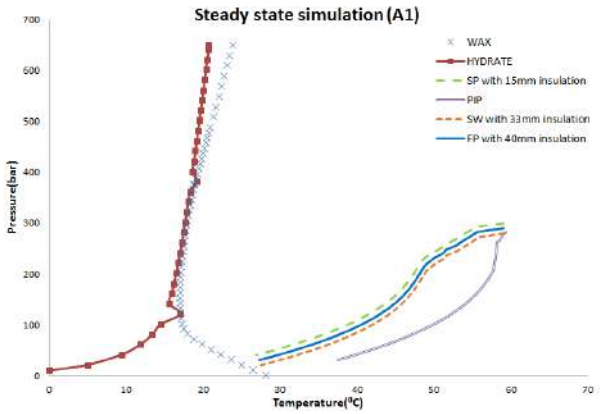

Figure 4.2: Pressure versus Temperature (Steady-state, Cluster A1)

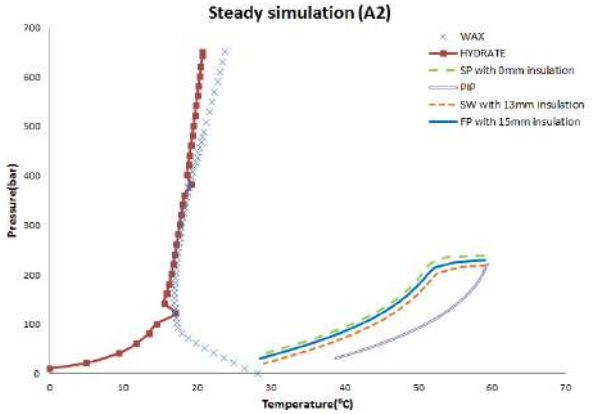

Figure 4.3: Pressure versus Temperature (Steady-state, Cluster A2)

In Figures 4.2 and 4.3, the PT curves for the SP, the SW and the FP overlapped since they are designed to maintain the same minimum temperature. In order to avoid this overlapping, the PT curve of the SP was moved upward by 10 bars

and that of the SW was moved downward by 10 bars. As shown in Figure 4.2, the SP, the FP and the SW need different extra insulation thickness to achieve a qualified insulation performance for Cluster A1. The SP needed the smallest insulation thickness (15mm). The PIP was designed to achieve U-value as 1 $W/m^2.K$ which gave it the best insulation performance. The FP needed the largest insulation thickness (40mm).

The total pipeline length of cluster A2 is smaller than that of cluster A1. Therefore, pipelines of cluster A2 needed less extra insulation to meet the requirement than that of cluster A1. In Figure 4.3, the SP was capable of meeting the insulation requirement without insulation while the FP needed 15mm insulation and the SW needed 13mm. With U-value at 1 W/m^2, the PIP kept the temperature far from the critical region.

Transient simulations were carried out to get the temperature distribution after 8 hours of shut-in operation. The PT curves of the whole system are shown in Figures 4.4 and 4.5.

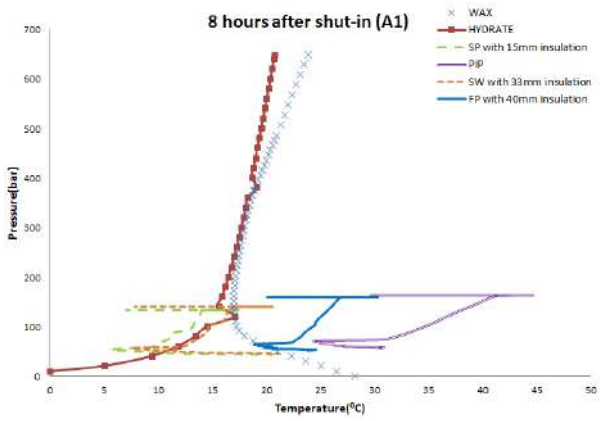

Figure 4.4: Pressure versus Temperature (Shut-in, Cluster A1)

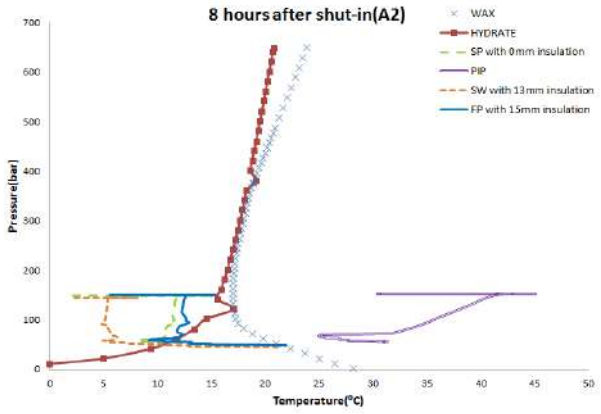

Figure 4.5: Pressure versus Temperature (Shut-in, Cluster A2))

As shown, the insulation configurations for the SP, the SW and the FP which

ensure flow in the steady-state condition were not able to meet the thermal insulation requirement in the shut-in condition. The major part of the PT curves for the SP and the SW entered the critical region where hydrate and wax would precipitate in the pipeline. For Cluster A1, a small part of the PT curve for the FP contacts the wax critical curve, which implies that wax will appear in some part of the system. However, scenario using FP in Cluster A2 would have serious flow assurance problems. For both clusters, scenario using PIP had no flow assurance problem during 8 hours of the shut-in operation.

In order to develop qualified insulation scenarios, the insulation thicknesses for the SP, the SW and the FP were increased until they could provide 8 hours of cool-down time (see Figures 4.6 and 4.7).

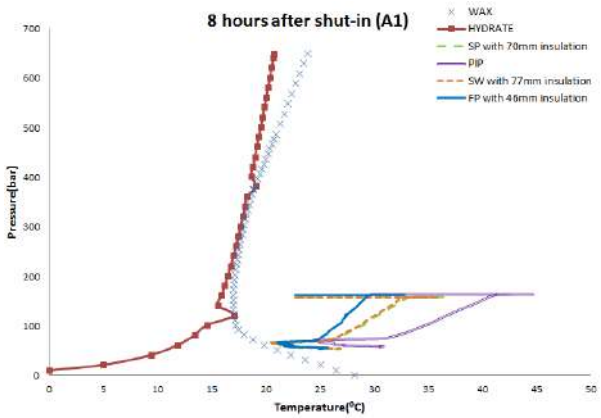

Figure 4.6: Pressure versus Temperature (Shut-in, Cluster A1)

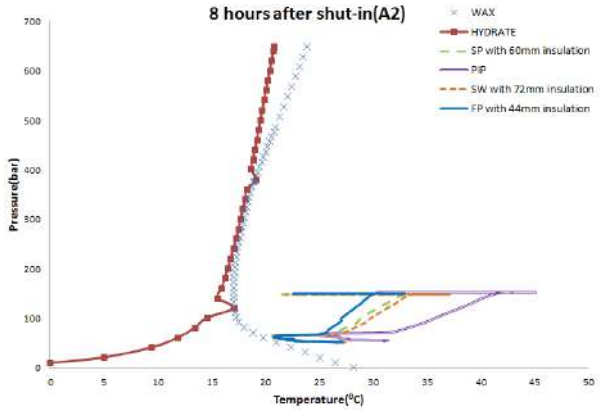

Figure 4.7: Pressure versus Temperature (Shut-in, Cluster A2))

The insulation thickness for the SP increased from 15mm to 70mm in cluster A1 and 0mm to 60mm in cluster A2. The insulation thickness for the SW increased from 33mm to 77mm in cluster A1 and 13mm to 72mm in cluster A2. As for FP, insulation thickness was slightly raised from 40mm to 46mm in cluster A1 and 15mm to 44mm in cluster A2.

4.1.3 Volumetric heat capacity and energy storage

The required insulation thicknesses for each scenario in the steady-state and transient simulations are shown in Figure 4.8.

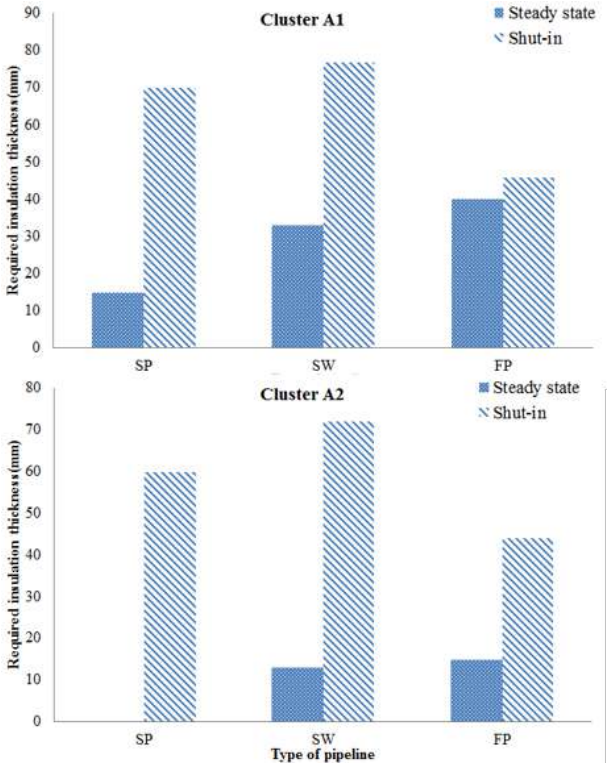

Figure 4.8: Required insulation thickness for the SP, the SW and the FP

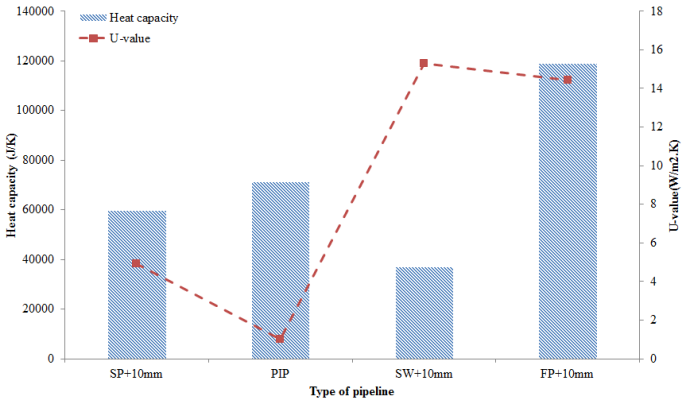

Figure 4.9: U-values and heat capacities of SP, SW, FP and PIP

As shown, the SP requires small extra insulation in the steady-state condition. However, it performs inadequately in the shut-in condition. This is mainly because the SP has a good U-value but a low heat capacity (Figure 4.9). The U-value has influence on the heat flow rate. The lower U-value results in a lower heat flow rate. The heat capacity, on the other hand, has the influence on how much heat energy is stored in the pipeline. In the shut-in condition, the heat loss process of the pipeline

is similar to a leaking barrel (Figure 4.10). The amount of water in the barrel is the thermal energy stored in the pipeline. The water outflow (Q_{out}) has an analogy with the heat transferred from the pipeline to the sea water.

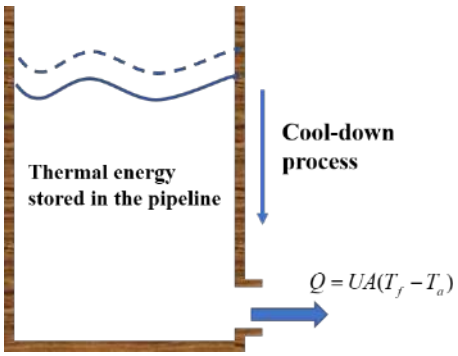

Figure 4.10: Leaking barrel as an analogy with pipeline heat loss in the shut-in condition

As shown in Figures 4.9 and 4.10, the SP has a smaller leaking flow rate (U-value) than that of both the SW and the FP, which makes it perform better than the SW and the FP in the steady-state condition. However, both the SP and the SW have rather smaller barrels (heat capacity) than that of the FP, which explains why the FP has a better insulation performance in the shut-in condition. Attention should be paid to the performance of the PIP. Its heat capacity is also smaller than that of the FP. However, its U-value is small enough to enable the PIP to outperform the FP in the shut-in condition. By combining the fluid flow conservation equations and heat conduction equations, Barrera [71, 126] built a numerical model to simulate the cool-down process of a subsea pipeline. Their simulation results also show that the thermal capacity of the pipeline wall has a significant influence on the cool-down time and higher thermal capacity of the pipeline wall results in a longer cool-down time.

Even though the SP has a relatively low U-value and needs a small amount of extra insulation in the steady-state condition, it needs a huge amount of extra insulation in the shut-in condition due to its small heat capacity, which finally results in a thick insulation layer for the SP. Further, the overall thermal properties of the SP system are greatly influenced by the core layer material. As an attempt to test the SP performance with the different core layer material, a parametric study on thermal properties of the SP core layer material was carried out using 63 combinations of different thermal conductivity and volumetric heat capacity (VHC). The SP configuration remains the same, as shown in Table 4.2. For each group of thermal conductivity and VHC, the required insulation thicknesses for the SP to attend the thermal insulation requirements in the steady-state and the shut-in conditions are shown in 4.11 and 4.12, respectively. Note that Cluster A1 was

employed for the parametric study.

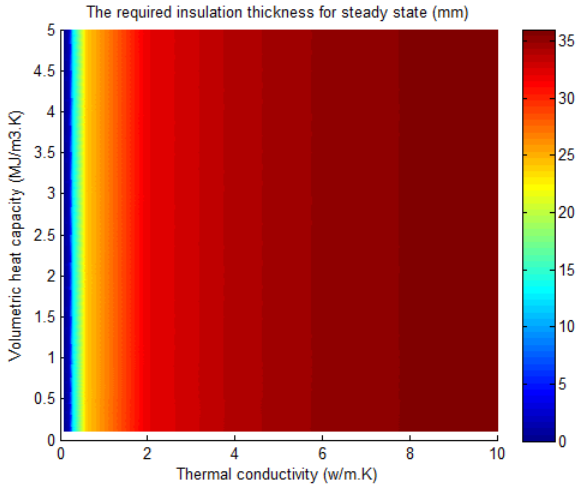

Figure 4.11: Required insulation thickness for the SP in the steady-state condition(Cluster A1)

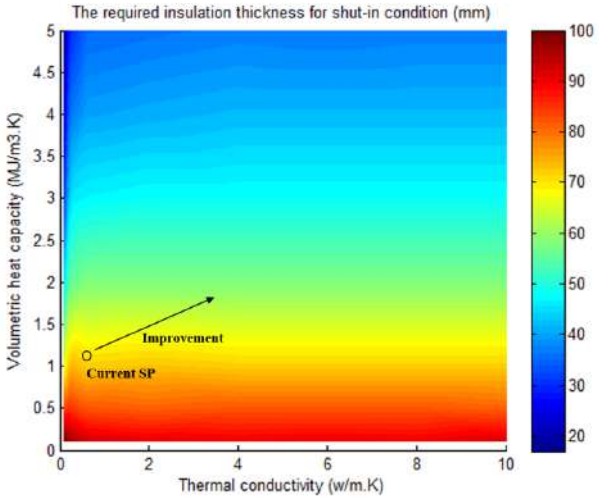

Figure 4.12: Required insulation thickness for the SP in the shut-in condition(Cluster A1)

As shown in Figure 4.11, the VHC barely influences the required insulation thickness in the steady-state condition while the thermal conductivity governs the performance. Special attention should be paid to Figure 4.12. With the same VHC, the variation of thermal conductivity barely changes the required insulation thickness in the shut-in condition. This is because the required insulation thickness for the shut-in condition is large enough to provide a low U-value, which makes the variation of thermal conductivity in the core layer material less vital to the heat transfer flow rate. The most preferred combination for the core layer material is a low thermal conductivity and a high VHC, which would result in the minimum extra insulation thickness. However, for a certain material, its density normally has

a positive correlation with thermal conductivity. A material with a lower thermal conductivity usually possesses a lower density, which may decrease its structural strength and the VHC. A wise improvement is to choose a material with higher VHC. Though the thermal conductivity has to be increased to get a higher VHC, the overall insulation performance of the sandwich pipe can be improved by reducing the required insulation thickness for both steady-state and shut-in conditions.

The VHC of the SHCC is 1.29 ($MJ/m^3.K$). As shown in Table 4.4, the volumetric heat capacities of commonly used insulation material are below 1.5 ($MJ/m^3.K$).

Table 4.4: Thermal properties of commonly used insulation materials

Insulation material	k (W/m.K)	$\rho(kg/m^3)$	c (J/kg.K)	VHC($MJ/m^3.K$)
Polyurethane	0.195	800	1800	1.44
Syntactic Foam	0.135	765	1950	1.49
Polypropylene Foam	0.17	700	1920	1.34
Polypropylene Reinforced	0.08	650	1750	1.14
Polyureathane Foam	0.03	700	1800	1.26
Polyureathane Syntactic	0.14	719.5	1500	1.08
Polyureathane Glass Syntactic	0.145	720	1700	1.22
Calcium Silicate Pipe Insulation	0.96	230	710	0.16
Cellular Glass	1.01	136	1400	0.19
Mineral Wool	0.925	149	840	0.13
Grooved Mineral	1.07	146	840	0.12

Figure 4.12 shows that the SP needs around 70 mm of extra insulation with a VHC of the core layer material around 1.5 $MJ/m^3.K$. Thus, Thus, selecting a core layer material with a higher VHC than that of the common insulation materials is critical to improving the insulation performance of SPs. However, the VHC of solid materials does not vary widely. There exists a noticeable inverse correlation between a solid's density and its specific heat capacity on a per-mass basis.

The Dulong-Petit law [127] states that the heat capacity of one mole of a solid substance is a constant, which is 3R per Kelvin (where R is the gas constant). Based on the Dulong -Petit law, the magnitude VHC of a solid substance mainly depends on the number of atoms per unit volume. For certain material, the specific heat per mass, density, and VHC can be expressed as:

$$\begin{aligned} VHC &= c \times \rho = num \times \tfrac{3S}{N} \\ \rho &= \tfrac{num \times M}{N}; \qquad c = \tfrac{3S}{M} \end{aligned} \tag{4.1}$$

Where c is the specific heat per mass, M is the molar mass, $3S$ is the constant for molar specific heat, ρ is the density, N is Avogadro's number, num is the number of atoms per unit volume.

Under the applicable rang of Dulong-Petit law, Equation 4.1 shows that the

atomic size of a substance has a great influence on the VHC. According to [128], there is an approximate tendency of atoms of most elements to be about the same size, despite much wider variations in density and atomic weight. Therefore, the VHC of solid substance has a small variation range from 1.2 to 3.5 $MJ/m^3.K$.

Based on the above knowledge, there are two possible options to increase the VHC of the SP core layer material:

1. A higher VHC can be achieved by incorporating the phase change material (PCM) in the core layer. As discussed in section 2.1, the PCM possesses a heat storage capacity that is far greater than normal insulation materials.

2. Increase the inner steel layer.

The investigation of the core layer material incorporated PCM is beyond the scope of the thesis. The discussion focuses on the second option. It turns out that the steel has a high VHC among solid substances (around 3.5 $MJ/m^3.K$), and it can be used to improve the insulation performance of the sandwich pipe. Steel is commonly used to provide structural strength for the subsea pipeline and is never considered as a material to provide thermal insulation. However, in the case of the sandwich pipe, there are several advantages of utilizing the steel to store thermal energy. First, the inner steel wall directly contacts with the produced fluid which keeps the temperature of this steel part at the highest temperature compares to the other layer. With the same VHC, steel can store more thermal energy than other materials due to its ideal location in the pipeline. Second, a thicker inner steel layer can offer not only a better insulation performance in the shut-in condition but also a higher structural strength. Thus, within a proper range, a slightly thicker inner steel layer would reduce the thicknesses of both the core layer and the extra insulation layer. A comparison study is carried out between the original SP configuration and a new scenario with a thicker inner steel layer to evaluate this strategy. See Table 4.5.

Table 4.5: Layer thicknesses for Scenario 1 and 2

	Configuration 1	Configuration 2
Material	Layer thickness (mm)	Layer thickness (mm)
Inner steel layer	3	13
SHCC	31	21
Outer steel layer	3	3
extra insulation	72	50

Configuration 1 is the SP used in the previous study (see Table 4.2), and configuration 2 is the SP with 10 mm thicker steel wall and 10 mm thinner SHCC layer.

Simulation in OLGA shows that configuration 2 can decrease the extra insulation from 72 mm to 50 mm. Nevertheless, increasing the inner steel layer would increase the cost and submerged weight of the SP, which should be considered carefully for a balanced SP design.

With the knowledge that the inner steel layer also influences on the insulation performance of the sandwich pipe, the design process of the SP becomes quite interesting. On the aspect of structural design, the variation on the inner steel layer influences the thicknesses of the core layer and outer steel layer. In terms of insulation design, the thicknesses of the extra insulation and the core layers are not the only two that affect the SP insulation performance. The inner steel layer can be more efficient than the extra insulation to prolong the cool-down time. Besides, since the core layer provides both structural resistance and insulation capacity, the variation in the thickness of the core layer affects the insulation performance of the sandwich pipe too. Thus, the SP should be considered as an integrated system for an efficient design. An optimum design method combing both strength and thermal insulation is requested.

4.2 A thermal analysis model for SPs

To simplify the model while capturing the main features of the physical problem, the following assumptions were made:

- Single phase flow with constant properties was assumed. This assumption is valid when fluid pressure is higher than the saturation pressure of the produced fluid;
- The variations of kinetic energy and potential energy were neglected for the fluid energy conservation equation;
- The heat conductions along the axial direction of the pipeline for both fluid and SP wall were small enough to be neglected;
- The perfect thermal contact was assumed for the inter-layer surfaces of the SP;
- No heat generation and phase change exist in any of the layers;
- The solid layers are isotropic with respect to heat conduction;
- Material properties of all solid layers are constant.

As illustrated in Figure 4.13, the fluid energy conservation equation can be written by Equation 4.2:

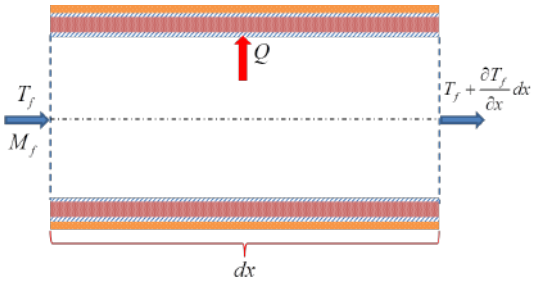

Figure 4.13: Sketch illustrating the energy conservation of the fluid in an SP element

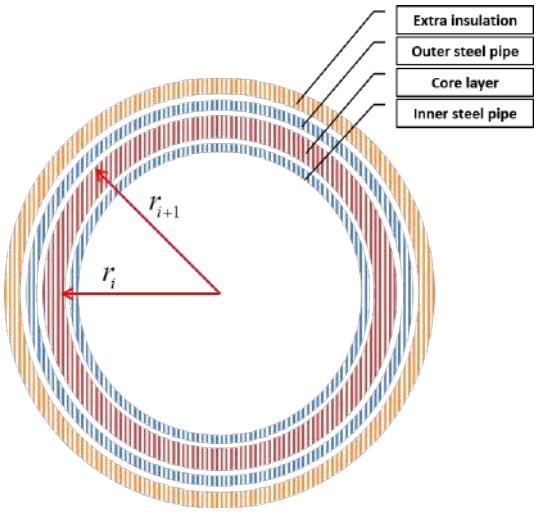

Figure 4.14: Cross section area of the SP pipeline

$$M_f c_p T_f - M_f c_p (T_f + \frac{\partial T_f}{\partial x}\Delta x) - Q = \pi r_0^2 \Delta x \rho_f c_p \frac{\partial T_f}{\partial t} \tag{4.2}$$

where M_f is the mass flow rate (kg/s), c_p is the fluid specific heat (J/kg. ℃), T_f is the fluid temperature (℃), ρ_f is the fluid density (kg/m^3), Q is the heat transfer rate from fluid to the ambient environment (w), t is time variable (s), and $r_0 = r_1 - t_1$ is the inside radius of the inner steel pipe (m).

The heat conduction equation for the SP layers in the radial direction is:

$$\frac{\partial}{r\partial r}\left(k_i r \frac{\partial T_i}{\partial r}\right) = \rho_i c_{pi} \frac{\partial T_i}{\partial t}, \qquad r_{i-1} \leq r \leq r_i \tag{4.3}$$

where k_i is the thermal conductivity of the i-th layer (w/m. ℃), ρ_i is the density of the i-th layer (kg/m^3), c_{pi} is the specific heat of the i-th layer (J/kg. ℃).

Steady-state model

Under the steady-state condition, the heat loss of the fluid can be expressed by overall heat transfer coefficient:

$$Q{=}2\pi r_0 dx U(T_f - T_a) \tag{4.4}$$

$$U = \frac{1}{\frac{1}{h_1} + \sum_{i=1}^{n} \frac{r_0}{k_i} \ln \frac{r_i}{r_{i-1}} + \frac{r_0}{r_{nl}} \frac{1}{h_a}} \tag{4.5}$$

where U is the overall heat transfer coefficient for multilayer pipe ($w/m^2.$), T_a is the ambient temperature (℃), h_1 is the inner heat transfer coefficient between the produced fluid and the SP inner surface ($w/m^2.$), r_{i-1} is the inside radius of the i-th layer (m), r_i is the outside radius of the i-th layer (m), nl is the total number of layers of the SP and h_a is the outer heat transfer coefficient between the ambient fluid and the SP outer surface ($w/m^2.$).

Since the fluid temperature is time independent in the steady-state condition, the Equation 4.2 becomes:

$$M_f c_p \frac{dT_f}{dx} = -2\pi r_0 U (T_f - T_a) \tag{4.6}$$

$$\text{with the boundary condition:} \qquad T_f|_{(x=0)} = T_{in} \tag{4.7}$$

where T_{in} is the inlet fluid temperature (℃).

The temperature distribution along the SP under steady-state condition becomes:

$$T_f(x) = (T_{in} - T_a) e^{-\frac{2\pi r_0 U x}{M_f c_p}} + T_a \tag{4.8}$$

Similarly, the time dependent term in Equation 4.3 vanishes in the steady-state condition:

$$\frac{d}{rdr}\left(-k_i r \frac{dT_i}{dr}\right) = 0 \tag{4.9}$$

With the boundary and the perfect thermal contact inter-layer condition:

$$h_1(T_f - T_1) = -k_1 \frac{\partial T_1}{\partial r} \quad \text{at} \quad r = r_0 \tag{4.10}$$

$$k_i \frac{\partial T_i}{\partial r} = k_{i+1} \frac{\partial T_{i+1}}{r}; \quad \text{and} \quad T_i = T_{i+1} \quad \text{at inter-layer contact surface} \tag{4.11}$$

$$h_a(T_{nl} - T_a) = -k_{nl} \frac{\partial T_{nl}}{\partial r} \quad \text{at} \quad r = r_{nl} \tag{4.12}$$

The temperature distribution through the SP layers at the steady-state condition can be obtained analytically with Equations 4.9, 4.10, 4.11, and 4.12.

Transient model

Since the SP wall temperature changes in the transient condition, the heat transfer from fluid to SP wall (Q) in the Equation 4.2 should be defined as:

$$Q = 2\pi r_0 dx h_1 (T_f(t) - T_1(r_0, t)) \tag{4.13}$$

Substituting Equation 4.13 into 4.2 and simplifying:

$$\frac{\partial T_f}{\partial t} + v_f \frac{\partial T_f}{\partial x} = -\frac{2h_1(T_f - T_1(r_0, t))}{r_0 \rho_f c_p} \tag{4.14}$$

where

$$v_f$$

is the fluid flow velocity (m/s).

In the shut-in condition $v_f = 0$, the spatial derivative in equation 4.14 was eliminated and the equation was solved explicitly by finite difference method. The pipe wall temperature at the contact surface of liquid and pipe ($T_1(r_0)$) was obtained by solving the Equation 4.3. The Equation 4.3 was solved implicitly by finite difference method with a second-order-accurate scheme. Applying the boundary conditions, Equations 4.10, 4.11, and 4.12, for pipe layers in the transient simulation reduces the accuracy of simulation results since the model neglects the thermal capacity of the pipe wall elements that locate at the boundary. Therefore, energy conservation equations were established for these elements to improve the accuracy of the transient model.

Empirical equations for heat transfer coefficient

For the inner heat transfer coefficient (h_1), both forced and natural convection were considered. The Nusselt number (Nu) for laminar flow and transition state [126]:

$$Nu = 3.66 \quad \text{while} \quad \text{Re} < 2000 \tag{4.15}$$

$$Nu = 0.01056\text{Re} - 17.46 \quad \text{while} \quad 2000 < \text{Re} < 2500 \tag{4.16}$$

The Nusselt number for turbulent flow [129]:

$$Nu = 0.023\text{Re}^{0.8} Pr^{0.3} \quad \text{while} \quad 2500 < \text{Re} \tag{4.17}$$

$$\text{Re} = \frac{2\rho_f v_f r_0}{\mu_f} \tag{4.18}$$

$$\mathrm{Pr} = \frac{\mu_f c_p}{k_f} \tag{4.19}$$

where Re is the Reynolds number, Pr is the Prandtl number, v_f is the fluid flow velocity (m/s), μ_f is the fluid viscosity (Pa.s), and k_f is the thermal conductivity of the fluid (w/m.℃).

Regarding the natural convection, the Nusselt number is approximated by the Olivier's correlation [126]:

$$Nu = 1.75\left[\mathrm{Re}\,\mathrm{Pr} + 0.0083(Gr\,\mathrm{Pr})^{0.75}\right]^{\frac{1}{3}} \tag{4.20}$$

$$Gr = \frac{(2r_0)^3 \rho_f^2 g \beta_f \left|\Delta T\right|}{\mu_f^2} \tag{4.21}$$

where g is the gravitational acceleration (m/s^2), β_f is the thermal expansion coefficient of the fluid, and $|\Delta T|$ is the temperature difference between the fluid and the inner surface of the pipe.

Equation 4.20 is effective when $Gr/\mathrm{Re}^2 > 1$ that means the natural convection is more dominant than the forced convection. The inner heat transfer coefficient is calculated using the Nusselt number:

$$h_1 = \frac{k_f Nu}{2r_0} \tag{4.22}$$

Assuming the temperature of the outermost surface of the SP equals sea water temperature, a large value was assumed for the outer heat transfer coefficient (h_a) [130].

Validation of the thermal model

The thermal model was constructed with certain assumptions and correlations for convection coefficient. The validation of the thermal model is critical for a solid base of this study. Therefore, the professional multiphase computational software OLGA was employed to compare the simulation results with the developed model.

Table 4.6: SP configuration for model validation

Pipeline length (m)	3000
Innermost diameter of the SP (inch)	8
Thickness of inner steel layer (mm)	4
Thickness of the core layer (mm)	20
Thickness of outer steel layer (mm)	4
Thickness of extra insulation thickness (mm)	10

Table 4.7: Related thermal properties

Material	k (w/m.℃)	c (J/kg.℃)	ρ (kg/m^3)
Steel tube	50	500	7850
SHCC core	0.28	880	1473
Insulation material	0.16	1220	1040
Fluid (water)	0.606	4186	1000

Table 4.8: Temperature and flow rate information

Sea water temperature (℃)	2
Inlet temperature (℃)	60

The fluid temperature distributions along the pipeline calculated by software OLGA and the thermal model are displayed in Figure 4.15. As shown, a good agreement is acquired for temperature distributions in the steady-state condition given by the model and OLGA.

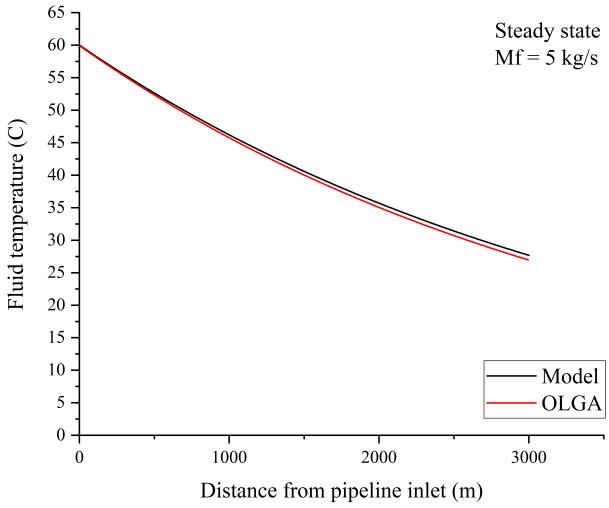

Figure 4.15: Temperature distributions calculated by the model and OLGA

The validation of the thermal model was evaluated by comparing the temperature variation at x = 3000 m in the shut-in condition. Two mass flow rates, 5 kg/s and 15 kg/s, were simulated.

Figure 4.16 shows that the temperature calculated by the thermal model is slightly higher than the results by OLGA. However, the comparison shows that the thermal model can perform with adequate accuracy in the transient simulation. The simulated results comparison between the model and software OLGA shows that the model is reliable for a horizontal laid SP where the fluid has no significant phase change.

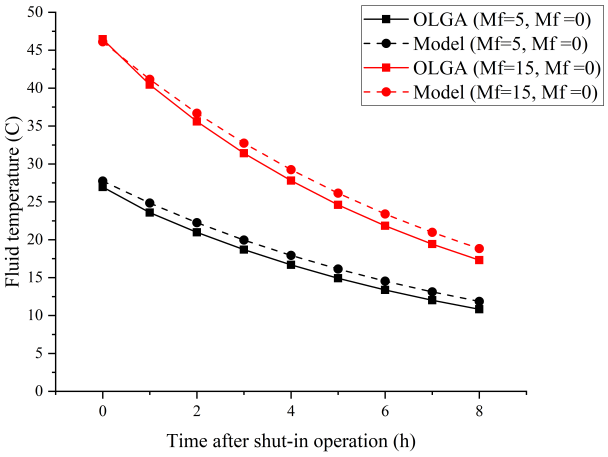

Figure 4.16: Temperature variation with time in the shut-in condition at x = 3000m

4.3 Summary

This chapter numerically investigated the insulation performance of the SHCC SP. A comparative study between the SP, the SW, the PIP and the FP was conducted. A mathematical model for the heat transfer analysis of the SP was developed. Several conclusions are summarized:

1. The SP outperformed the SW and the FP in the steady-state condition, but it did not perform well in the shut-in condition. A relatively low volumetric heat capacity (VHC) of the SHCC is part of the reason that explains the inadequate insulation performance of the SP in the shut-in condition.

2. The parametric study presented in section 4.1.3 shows that increasing the VHC of the core layer material results in the reduction of the required extra insulation thickness for the SP. However, due to the natural limitation, it is difficult for the VHC of a solid material to reach the required value to improve the insulation performance of the SP.

3. Since the steel has a greater VHC than common insulation materials, the numerical simulation shows that increasing the thickness of the inner steel layer can effectively decrease the required insulation thickness of the SP in the case study. However, increasing the thickness of the inner steel layer changes the structural strength of the whole system. Further, the effectiveness of an SP with thicker inner steel layer and thinner extra insulation layer needs to be evaluated based on the cost function. Thus, an integrated optimal SP design model combined with both structural and thermal insulation requirements is of utmost importance for an efficient application.

4. A mathematical model for the heat transfer analysis in the SP was developed.

A good agreement between the model and the OLGA software was achieved. The model will be incorporated into the SP optimization model in chapter 5.

Chapter 5

An optimization model for the SP

With the collapse pressure prediction model presented in chapter 3 and the thermal analysis model developed in chapter 4, this chapter focuses on the development of an optimal SP design model. Initially, an MINLP model is presented to minimize the SP cost. Then, a case study was conducted to compare the SP configurations obtained by the MINLP model and the design procedure by Castello et al. [9]. Considering four typical pipeline locations, a parametric study is carried out to discuss the optimal SP configurations for different scenarios. Based on the results, insightful understandings on how to design an SP and how to improve the SP performance are discussed. Besides, an optimization model of SWs is also developed to discuss the cost ratios of the optimal SPs and the optimal SWs for different working conditions. The preferred working conditions of SPs were emphasized.

5.1 An MINLP model for SP optimal design

5.1.1 Problem description

As the innermost diameter of a subsea pipeline is usually determined by the fluid velocity, which is a predetermined parameter for the thermal insulation and structural requirements, the SP design model includes the decision of the thickness and material for each layer. Typically, the configuration of a sandwich pipe can be defined by a vector $(t_1, t_2, t_3, \alpha_1, \alpha_2)$. Further, an extra insulation layer can be applied to sandwich pipes when high thermal insulation is required. Thus, thickness t_4 and the material parameter α_3 of the extra insulation layer should be included to fully define the configuration of a sandwich pipe $(t_1, t_2, t_3, t_4, \alpha_1, \alpha_2, \alpha_3)$, see Figure 1.2.

The design constraints of sandwich pipes can be classified into three categories: structural requirements, thermal insulation requirements, and constraints of optimization variables due to manufacturing or practical applications. The structural requirements state that the sandwich pipe should keep its structural integrity un-

der various loads in the application. In this study, the collapse pressure of an SP should exceed the hydrostatic pressure of the working condition was selected as the structural requirement, which is expressed by Equation 5.1:

$$P_{co}(D_1, t_1, t_2, t_3, \alpha_1, \alpha_2) \geq \rho_{sea} g h_{wd} \times F_{safe} \tag{5.1}$$

where ρ_{sea} density of the seawater, h_{wd} is the water depth (m), F_{safe} is the structural safety factor, and $(t_1, t_2, t_3, \alpha_1, \alpha_2)$ are the decision variables.

Since the extra insulation layer barely contributes to the structural resistance of the SP system, (t_4, α_3) are not included in the decision variables of the structural constraint.

To prevent solid precipitations like wax or hydrate to form in the pipeline, the thermal insulation requirements normally require the pipeline to maintain the fluid temperature beyond a certain level in the steady-state condition and to provide enough cool-down time in the shut-in condition. The cool-down time means the time period for the fluid temperature to drop below the hydrate formation temperature after the shut-in operation. The fluid temperature distributions in a pipeline in both steady-state and shut-in conditions are related to many factors which mainly include flow rate, fluid properties, inlet temperature, pipeline diameter, pipeline length, pipeline configuration, and the surrounding seawater temperature. Since the pipeline configuration is to be designed, all other factors are treated as input parameters. The thermal insulation requirements can be expressed by Equations 5.2 and 5.3:

$$T_{\min}(t_1, t_2, t_3, t_4, \alpha_1, \alpha_2, \alpha_3) \geq T_{require} \tag{5.2}$$

$$t_{cool}(t_1, t_2, t_3, t_4, \alpha_1, \alpha_2, \alpha_3) \geq t_{require} \tag{5.3}$$

where $T_{\min}$ and $T_{require}$ are the minimum fluid temperature and the required minimum temperature in the steady-state condition (℃), and t_{cool} and $t_{require}$ are cool-down time and the required cool-down time in the shut-in condition (h).

The constraints of the decision variables mainly involve limitations from the commercial steel pipe sizes, the available core layer materials, the available insulation materials. The relations between all the input parameters, constraints, and decision variables are illustrated in Figure 5.1.

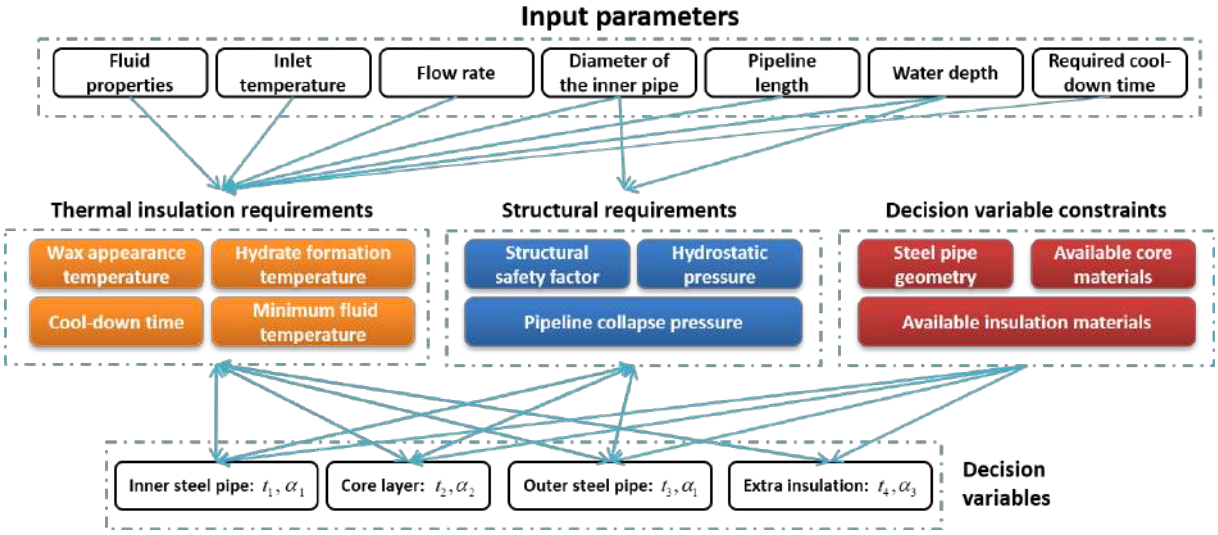

Figure 5.1: Logical relations among variables and constraints

5.1.2 Mathematical Model

Cost model of sandwich pipes

The cost model of SPs serves as the objective function in the optimization process. Building a valid cost model of SPs is the premise of a correct optimization result. The cost composition of traditional single-wall pipes can be a reference to construct the cost model of SPs. According to Kaiser [131], the material and installation services are the major cost of single-wall pipes. The cost model of SPs also can be considered similarly as shown in Equation 5.4.

$$C_{total} = C_{sp} \times N_{sp} + C_{ins} \tag{5.4}$$

$$N_{sp} = \frac{L}{L_{sp}} \tag{5.5}$$

where C_{total} is the total cost of the SP (\$), N_{sp} is the number of SP sections, C_{ins} is the pipeline installation cost (\$) L is the total length of the SP (m), and L_{sp} is the length of a SP section (m).

Sandwich pipe section cost (C_{sp})

Steel pipe cost. Two steel pipes, inner steel pipe, and outer steel pipe are included in an SP. Steel pipe cost is decided by the steel grade, diameter, wall thickness, and fabrication method. Three steel grades X60, X70, and X80 were considered in this study. A regression was developed from a database (three hundred data points generated by the software Questor [132]) that relates costs and configurations of steel pipes, see equation 5.6. The database includes prices of standard size pipes

with a diameter from 4 inches to 24 inches and different wall thicknesses. Within the collected database, equation 5.6 gives the unit length cost of steel pipes with an average error of 4.33%.

$$\begin{aligned} C_i = (&1.92 + 1.2 \times 10^5 t_i D_i + 1.97 \times 10^5 t_i {D_i}^3 - 5210 t_i \\ &- 2.45 \times 10^5 t_i {D_i}^2) \times (1 + SG); \quad i = 1, 3 \end{aligned} \tag{5.6}$$

where C_i is the cost per unit length of the i-th layer (\$/m), t_i is the wall thickness of the i-th layer (m), D_i is the outside diameter of the i-th layer (m), and SG is the price coefficient of steel grade, see Table 5.1.

Table 5.1: Price coefficient of steel grade

Steel type	SG*	SG**
X60	0.00%	0.00%
X70	2.75%	3.56%
X80	7.16%	9.30%

* for pipe with Diameter <= 14 inches
** for pipe with Diameter > 14 inches

Core layer cost. In this study, two materials, the SHCC and the PP, were considered in the core layer. Both material cost and fabrication cost were considered for the core layer. The price of the SHCC was assumed as the sum of the cost of concrete and PVA fiber. NRMCA 2018 shows that the average concrete cost is \$113 per cubic yard [133]. The fabrication of SPs with SHCC cores mainly involves injecting the concrete into the annulus between inner and outer steel pipes. Therefore, with concrete delivery and pouring, the price of concrete per cubic yard varies from \$119 to \$147 [134]. Considering the price and mass percentage of PVA fiber in SHCC [135], the cost of the SHCC layer is \$211.4 to \$247.5 per cubic meter. The average value of \$229.45 per cubic meter was used in this study. As for the PP core layer, the material cost of PP is \$1530 per cubic meter [12], and 5% of material cost was assumed for the fabrication cost factor of a PP core layer.

Extra insulation layer cost. An extra insulation layer can be applied on the external surface of the outer steel pipe to achieve better insulation performance. Four subsea insulation materials were evaluated in the optimization of SPs. Their price collected by Yang et al. [12] are listed in Table 5.2. Also, 5% of material cost was assumed for fabrication cost.

The cost per unit length of the core and the extra insulation layers can be calculated by Equations 5.7 and 5.8:

$$V_i = \pi \left[(r_{i-1} + t_i)^2 - (r_{i-1})^2 \right]; \quad i = 2, 4 \tag{5.7}$$

$$C_{\mathrm{i}} = V_i \times MC_i \times (1 + F_i); \quad i = 2, 4 \tag{5.8}$$

where V_i volume per unit length of the i-th layer (m^2), r_i is the outside radius of the i-th layer (m), MC_{i} is the material cost of the i-th layer ($\$/m^3$), and F_{i} is the fabrication cost factor for the i-th layer.

Based on Equations 5.6 to 5.8, the cost of a sandwich pipe section (C_{sp}) can be expressed as:

$$C_{sp} = \sum_{i=1}^{4} C_i L_{sp} \tag{5.9}$$

In this study, the sandwich pipe section length L_{sp} was assumed as the standard steel pipe section length 12m.

Table 5.2: Price of different insulation materials.

Material	Unit price (US \$/kg)
Syntactic PP	2.8
Rubber	1
Syntactic epoxy	4.15
PP	1.7

Installation cost (C_{ins})

In order to model the installation cost of SPs, it is necessary to determine the installation method for SPs. As discussed in section 2.3, reeling-lay could reduce the SP installation cost by avoiding offshore welding process, reeling-lay method with onshore welding process was assumed for the installation of SPs. The main concern of applying the reeling-lay method is the limitation of pipe size. In this thesis, SPs of all sizes were assumed to be installed by the reeling-lay method.

The installation cost (C_{ins}) can be considered as two parts, connection cost of the pipe section and the lay barge cost, see equation 5.10.

$$C_{\mathrm{ins}} = C_{con} \times (N_{sp} - 1) + C_{\mathrm{vessel}} \tag{5.10}$$

where C_{con} is the pipe section connection cost per joint (\$/joint), and C_{vessel} is the lay barge cost (\$).

The lay barge cost C_{vessel} was considered independent to the SP configuration and only the connection cost C_{con} was included in the objective function. The assumption is based on two reasons:

- Since the welding process depends on the SP configuration, the connection cost is directly related to the SP configuration.

- The lay barge cost is largely decided by the total working time of the lay barge and its day rates [131]. The total working time is decided by the pipeline length, water depth, weather condition, lay rate, and vessel mobilization time. Among them, the lay rate is influenced by pipeline configurations when offshore welding of pipes is necessary [50, 136]. Since the offshore welding is avoided by the assumed installation method of SPs, the total working time could be considered independent to the SP configuration. The day rate of a lay barge is related to the vessel specification. Indeed, different SP configuration may result in different vessel specifications with different day rate. However, for a fixed innermost diameter, the variation among different SP configurations that meet the same design requirements may not be significant. To simplify the cost model, the lay barge cost was assumed independent of the SP configuration.

Connection cost using onshore welding. The onshore welding cost is decided by the welding length, pipe thickness, and the welding filler material. A comprehensive welding cost model proposed by Fekete et al. [137] was employed to calculate the onshore welding cost for SPs. E8010 electrode with a cost at 3.89 \$/lb [137] was assumed as the filler metal for pipes of all steel grades. The welding cost per joint, which includes the welding for inner and outer steel pipes, can be expressed by Equations 5.11 and 5.12.

$$Cir_i = 2\pi(r_{\mathrm{i}} - t_i/2); \quad i = 1, 3 \tag{5.11}$$

$$C_{con} = Wel(3.28 \times Cir_1, \frac{1000t_1}{25.4}) + Wel(3.28 \times Cir_3, \frac{1000t_3}{25.4}) \tag{5.12}$$

where Cir_{i} is the perimeter of the i-th layer at $t_{\mathrm{i}}/2$ (m), and Wel is the welding cost function by Fekete et al. [137]. The input parameters were modified for dimensional compatibility of the employed units.

Based on the aforementioned equations, the cost of a sandwich pipe can be expressed by Equations 5.13:

$$C_{\mathrm{total}} = \sum_{i=1}^{4} C_i L_{sp} \times N_{sp} + C_{con} \times (N_{sp} - 1) \tag{5.13}$$

Note that the above cost function can serve as a proper objective function in the optimization of the configuration of SPs since it covers costs related to the SP configuration. However, for the cost estimation in real applications, the lay barge cost should be included in the cost function.

Thermal analyses of SPs

The established model in section 4.2 was employed to calculate the minimum fluid temperature in the steady-state condition and the cool-down time in shut-in condition for different SP configurations and input parameters.

Two materials of the core layer, the PP and the SHCC, and four subsea insulation materials were considered in the proposed optimization model. The thermal properties of the materials of the steel layers, core layer, and the extra insulation layer are shown in Table 5.3. And the fluid properties employed for all the case studies are listed in Table 5.4.

Table 5.3: Thermal properties of different materials for each layer

Layer	Material	k (W/m.K)	ρ (kg/m^3)	c (J/kg.℃)
Steel layer	Steel	50	7850	500
Core layer	SHCC	0.28	1473	880
Insulation or core layer	PP	0.22	900	1920
Extra insulation layer	Syntactic PP	0.16	765	1950
	Rubber	0.28	1300	2005
	Syntactic epoxy	0.13	850	1240

Table 5.4: Oil properties

API grade	25.5
GOR (Sm^3/m^3)	145
Average c (J/kg.℃)	2070
Average k (w/m.℃)	0.1308
Average viscosity (Pa.s)	0.0034

Structural analysis for SP

The estimation of the collapse pressure of SPs is complicated due to the interactions between the layers. By providing accurate enough results without massive simulations, the empirical equations developed based on large-scale numerical simulations are a wise choice for the optimization model of SPs. The prediction equation proposed in chapter 3 was employed to estimate the collapse pressure of the SHCC SP, see equation 5.14.

Focusing on the PP SP, He et al. [45] developed two empirical equations for the collapse pressure estimation, one for the PP SP with weak inter-layer adhesion and another for the PP SP with strong inter-layer adhesion. In real applications, it is possible to reach good adhesion between the PP core and the steel layers by applying

proper adhesive. Thus, the empirical equation with strong inter-layer adhesion was employed in this study, see equation 5.15.

$$\begin{aligned} P_{predict} = &- 5.84 + \Big[7.66\left(\frac{t_1}{r_1}\right)^{(3.24-0.65\frac{t_2}{r_c})}(1-imp_1)^{0.56} \\ &+ 14.12\left(\frac{t_3}{r_3}\right)^{(0.72+0.88\frac{t_2}{r_c})}(1-imp_3)^{0.366}\Big] \\ &\times (\sigma_p)^{(-0.0226\frac{t_1}{r_1}-0.087\frac{t_3}{r_3}+0.42\frac{t_2}{r_c})} \\ &+ 23.47\left(\frac{t_2}{r_c}\right)^{(4.25-0.77\frac{t_2}{r_c})}(1-imp_c)^{0.3} \end{aligned} \tag{5.14}$$

$$\begin{aligned} \frac{P_{predict}}{E_p} =& 31.79\left(\frac{t_3}{r_3}\right)^{3.04}\left(\frac{r_1}{r_3}\right)^{0.7}\left(\frac{t_1}{r_1}\right)^{-0.126}\left(\frac{\sigma_p}{E_p}\right)^{0.915} \\ &+ 0.059\left(\frac{t_3}{r_3}\right)^{0.163}\left(\frac{r_1}{r_3}\right)^{-0.22}\left(\frac{t_1}{r_1}\right)^{1.138}\left(\frac{\sigma_p}{E_p}\right)^{0.53} imp_3{}^{-0.136} \\ &+ 7.29\text{E-}6\left(\frac{t_3}{r_3}\right)^{0.04}\left(\frac{r_1}{r_3}\right)^{-4}\left(\frac{t_1}{r_1}\right)^{-0.32} imp_3{}^{-0.077} \end{aligned} \tag{5.15}$$

A value of 200 GPa was assumed for the elastic modulus of steel (E_p). According to the API 5L standard, the yield stresses (σ_p) of X60, X70, and X80 are 415 MPa, 485 MPa, and 555 MPa, respectively. In addition, $Imp_i, i = 1, 3$ is the initial imperfection of the i-th layer. And a value of 0.5% was assumed for all the initial imperfections.

Optimization model and Constraints

The optimization model of the SP configuration $(t_1, t_2, t_3, t_4, \alpha_1, \alpha_2, \alpha_3)$ can be concluded as following:

Given the input parameters $(T_{in}, M_f, D_1, L, h_{wd},\ T_{wax}, T_{hydrate}, t_{require})$ and the produced fluid properties, minimize the SP cost function expressed by Equation 5.16.

$$C_{\text{total}}(t_1, t_2, t_3, t_4, \alpha_1, \alpha_2, \alpha_3) = \sum_{i=1}^{4} C_i L_{sp} \times N_{sp} + C_{con} \times (N_{sp} - 1) \tag{5.16}$$

With the structural requirement as one of the constraints, see Equation 5.17.

$$\rho g h_{wd} \times F_{safe} - P_{predict}(D_1, t_1, t_2, t_3, \alpha_1, \alpha_2) \leq 0 \tag{5.17}$$

And the thermal insulation requirements, see Equations 5.18 and 5.19.

$$\text{Steady-state:} \quad \begin{cases} T_{require} - T_{\min}(t_1, t_2, t_3, t_4, \alpha_1, \alpha_2, \alpha_3) \leq 0 \\ T_{require} = T_{wax} \end{cases} \tag{5.18}$$

$$\text{Shut-in:} \quad \begin{cases} t_{require} - t_{cool}(t_1, t_2, t_3, t_4, \alpha_1, \alpha_2, \alpha_3) \leq 0 \\ T_{\min}|_{t=t_{cool}} = T_{hydrate} \end{cases} \tag{5.19}$$

And constraints of decision variables, see Equation 5.20.

$$\begin{cases} lb_1 \leq t_1 \leq ub_1,\ lb_2 \leq t_2 \leq ub_2 \\ lb_3 \leq t_3 \leq ub_3,\ lb_4 \leq t_4 \leq ub_4 \\ \alpha_1 = 1, 2, 3....,\ \alpha_2 = 1, 2, 3.... \\ \alpha_3 = 1, 2, 3.... \end{cases} \tag{5.20}$$

where T_{in} is the inlet fluid temperature, M_f is the mass flow rate, D_1 is the outside diameter of the inner steel layer, L is the whole length of the SP, h_{wd} is the water depth, T_{wax} is the wax appearance temperature, $T_{hydrate}$ is the hydrate formation temperature, and $t_{require}$ is the required cool-down time.

In Equation 5.17, a value of 1.33 was set to the structural safety coefficient F_{safe} for PP sandwich pipes and single-wall pipes. Since the equation 5.14 was proposed conservatively assuming a frictionless inter-layer condition, no safety coefficient was applied to SHCC sandwich pipes.

According to the validation area of the empirical equations 5.14 and 5.15, the bounds of t_1 and t_2 were set as $0.02 \leq \frac{t_1}{r_1} \leq 0.09$ and $0.65 \leq \frac{r_1}{r_1+t_2} \leq 0.85$, respectively. Market research shows that the ERW pipe can be fabricated with diameter from 1/2 inches to 24 inches with thickness ranging from 2 mm to 22 mm [138]. Thus, 2 mm and 22 mm were selected as the bounds of the thickness of the outer steel layer (t_3). The extra insulation layer is not mandatory in the SP system. Thus, 0 mm and 100 mm were given to the bounds of the thickness of the extra insulation layer (t_4). The material parameter α_i was set as integer and each integer represents one material, see Table 5.5.

Table 5.5: Settings of materials parameters

(α_1)	Steel grade	(α_3)	Insulation material
1	X60	1	Syntactic PP
2	X70	2	Rubber
3	X80	3	Syntactic epoxy
(α_2)	Core material	4	PP
1	SHCC		
2	PP		

5.1.3 Model solving

Since the established model involves both continuous and integer variables, the optimization of SPs is a mixed-integer nonlinear problem. The penalty method was applied to deal with both structural and thermal insulation constraints with the penalty function proposed by Coath and Halgamugue [139]. Particle swarm optimization (PSO) method [102] was first employed to solve the proposed model, where the integer variables were rounded off after each iteration. Besides, several PSO variants, such as LPSO, CPSO [120], CPSOH [120], SLPSO [121], ELPSO [122], FIPSO [123], and MLPSO [124], were evaluated in solving the problem. However, Due to the complexity of the problem, the canonical PSO and the PSO variants performed unstably, giving different optimal configurations at each run. The variation of the material parameters showed significant impacts on the objective and constraint functions, which creates difficulties for the optimization algorithms. Thus, another widely used stochastic search technique, genetic algorithm (GA) [101], was tested. In genetic algorithms, each candidate solution is treated as chromosome, and the decision variables are represented as genes that are part of the chromosome. To deal with the integer variables in the proposed optimization model, the algorithm was binary coded and the length of the gene of each integer variable was controlled so that the corresponding binary string only represents integers. The application of GA displayed a promising direction by giving more stable results. Finally, the approach that combines PSO and GA proposed by Sahoo et al. [140] outperformed all the tested algorithms showing good robustness and convergence in solving the proposed model. In this GA-PSO algorithm, GA is operated first at each iteration and then the personal best solution of each particle from PSO is improved by comparing to the survived candidate solutions from GA. With the updated personal best particles, PSO is operated to finish the iteration. Figure 5.2 shows the flow chart of the employed algorithm.

The different steps of the GA-PSO algorithm are as follows:

Step-1 Set population size, maximum number of generations, probability of crossover, probability of mutation and the bounds of decision variables

Step-2 Set $t = 0$ (t represents the number of generation/iteration)

Step-3 Initialize the chromosomes/particles of the population

Step-4 Compute the fitness function for each chromosome/particle

Step-5 Find the global best chromosome/particle having the best fitness value

Step-6 Divide the chromosomes/particles into two groups, viz. $P_{GA}(t)$ and $P_{PSO}(t)$ with equal population size

Step-7 Repeat the following until the termination criterion is satisfied:

(i) Increase the value of t by unity

(ii) Conduct the evaluation on each individual of $P_{GA}(t)$and transform all individuals into binary form

(iii) Apply crossover & mutation operators on $P_{GA}(t)$ to produce new population $P_{GA}{}'(t)$

(iv) Transform individuals in $P_{GA}{}'(t)$ into real-number form and conduct the evaluation

(v) Compare the fitness value of $P_{GA}(t)$ and $P_{GA}{}'(t)$, and store better individuals to form $P_{GA}(t+1)$ using tournament selection

(vi) Conduct the evaluation for particles in $P_{PSO}(t)$ and store the personal best particle and global best particle

(vii) Improve the personal best particles in $P_{PSO}(t)$ by comparing them with the individuals in $P_{GA}(t+1)$

(viii) Compute the velocity of each particle

(ix) Obtain the new position of each particle $P_{PSO}(t+1)$

(x) Conduct the evaluation of $P_{PSO}(t+1)$ and improve the personal best particles and the global best particle

(xi) Store the overall global best solution by comparing the best individual in $P_{GA}(t+1)$ and the global best particle in $P_{PSO}(t+1)$

Step-8 Print the position and fitness of overall global best solution

Step-9 end

The related settings of the PSO-GA algorithm used in this study are as follows. The maximum iteration was 500. In GA, the population size was 50. The roulette wheel method was applied to select the individuals for the mating process. A hybrid crossover method that randomly employs single-point, double-point, or the uniform crossover was employed. The offspring size was set equal to the original population size. A value of 0.05 was set for the mutation probability. The new population was generated based on tournament selection. In PSO, 50 particles were set for the swarm. The canonical PSO was employed with the inertia coefficient gradually decreasing from 0.855 at the beginning to 0.345 at the end of the algorithm. Both social personal and social acceleration coefficients were set to 1.49445.

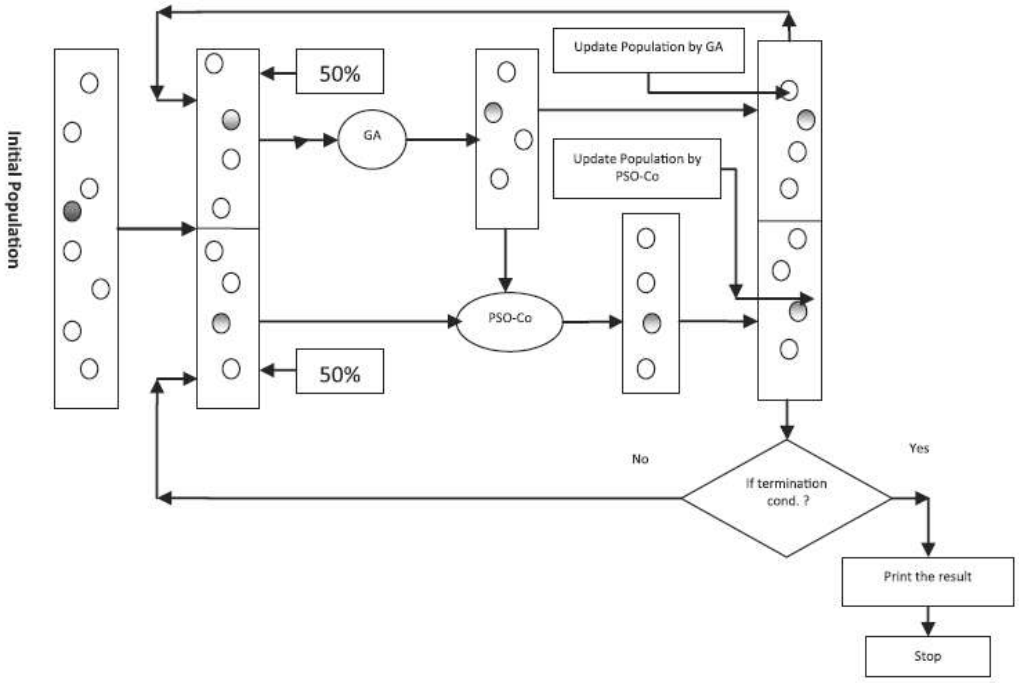

Figure 5.2: Flowchart the of the GA-PSO algorithm (adopted from [140])

5.2 Case study

A case study was conducted to evaluate the performance of the proposed optimization model. An SP of 8 inches was assumed to transport hydrocarbon fluid from a subsea manifold to a riser base. The input parameters are listed in Table 5.6. The insulation requirements were put as the SP should keep the fluid temperature beyond the wax appearance temperature in the steady-state condition and provide enough cool-down time, which is 8 hours in this case, before the fluid temperature drops below the hydrate appearance temperature in shut-in condition. As mentioned before, the fluid information shown in Table 5.4 was employed. Note that, in the real application, the appearance temperatures of wax and hydrate are related to the fluid properties. However, in this study, they were treated as input variables that are independent of the fluid properties. The proposed model was employed to obtain the optimal configuration of SPs. The GA-PSO algorithm was run five times. And good robustness and convergence were achieved, see Figures 5.3 and 5.4.

Table 5.6: Input parameters for case study

D_1 (inch)	8	$T_{hydrate}$ (℃)	25
L (m)	6000	$t_{require}$ (h)	8
h_{wd} (m)	2500	T_{sea} (℃)	2
T_{in} (℃)	55	M_f (kg/s)	60
T_{wax} (℃)	39		

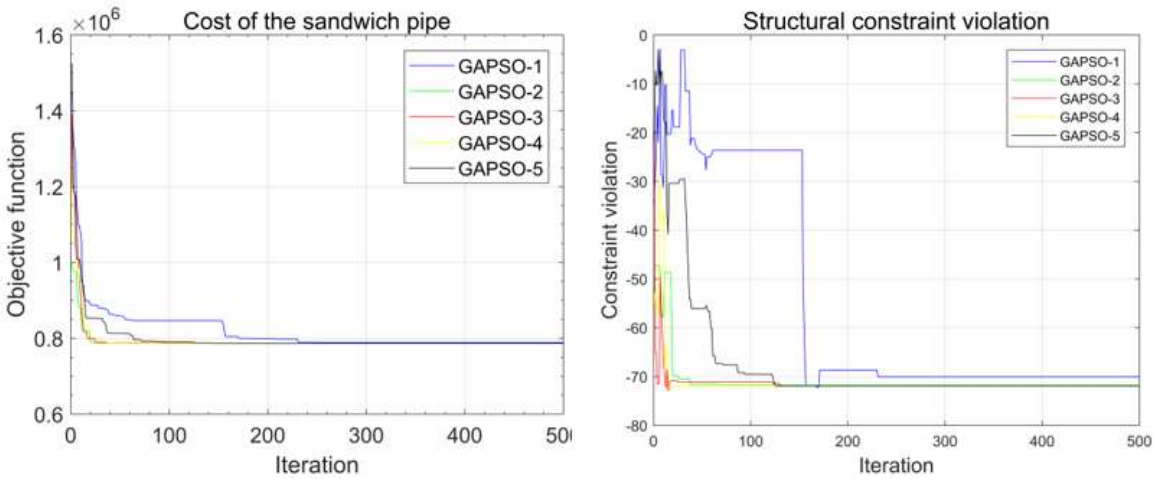

Figure 5.3: SP Cost and Structural constraint violation of each iteration

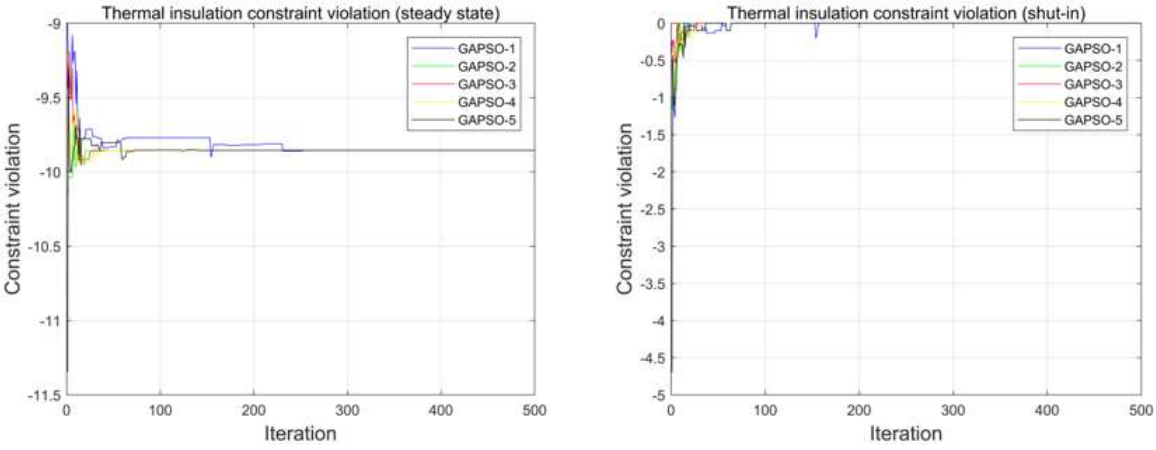

Figure 5.4: Violation of thermal insulation constraints of each iteration

As shown in Figures 5.3 and 5.4, at the late iterations of the GA-PSO, the violation of the structural constraint and that of the thermal insulation constraint in the steady-state condition are -71.8 and -9.85, which, according to the constraints defined by Equations 5.17 and 5.18, indicates that the optimal SP found by the model has the structural strength and the insulation capacity that exceed the structural requirement and the thermal insulation requirement in the steady-state condition. In this case, the collapse pressure of the optimal SP is 71.8 MPa higher than the required external pressure capacity. And the minimum temperature of the optimal SP in the steady-state condition is 9.85 ℃ higher than the required temperature. Meanwhile, the violation of the thermal insulation constraint in the shut-in condition converges to zero which means, with the present input parameters, the thermal insulation requirement in the shut-in condition is the principal requirement that controls the optimal SP configuration. To design an SP with structural strength and insulation capacity that exceeds the related requirements seem to be inefficient, which shows the complexity of the design of SPs and the necessity of a suitable

design method.

Castello et al. [9] briefly introduced their design procedure of SPs. Their design procedure is summarized as follows:

1. With the specified core material, the thickness of the core layer is determined by attending the insulation requirement in steady-state condition.

2. With the determined core layer, the thicknesses of inner and outer steel pipes are increased simultaneously until the sandwich pipe possess enough structural resistance.

3. If necessary, the thickness of the extra insulation layer is increased until the SP meets the cool-down time requirement.

Since the decision of the materials was not included in their procedure, two SP configurations were developed using SHCC and PP as core materials, respectively. X60 steel grade was assumed for the steel layers and the syntactic PP for the extra insulation layer. The results were compared with the optimized SP configuration. Furthermore, the configuration of an SW was also developed for comparison. X60 steel grade and PP were assumed for the SW materials. Using a safety factor equals to 1.33, the thickness of the steel pipe was determined by the DNV code [125]. The proposed thermal model was employed to determine the thickness of the insulation layer of the SW. The proposed cost function was modified for the cost estimation of the SW. The configurations of SPs and SW are displayed in Table 5.7.

Table 5.7: Pipeline configurations and costs

	Configurations of SPs and SW							
Label	t_1	t_2	t_3	t_4	α_1	α_2	α_3	Cost ($)
Optimal SP	2	54.7	2	25.6	1	1	1	783456.9
Castello et al. (SHCC SP)	4.2	27	4.2	37	1	1	1	1169713.2
Castello et al. (PP SP)	5.3	20.2	5.3	35	1	2	1	1392424
Single-wall	11.3	-	-	64.5	1	-	4	1309056.1

Table 5.8: Cost composition for each pipe configuration

	Cost composition			
Label	Steel layers	Core layer	Insulation layer	Welding cost
Optimal SP	41.60%	7.80%	47.40%	3.20%
Castello et al. (SHCC SP)	53.30%	2.30%	40.60%	3.80%
Castello et al. (PP SP)	55.20%	9.80%	30.80%	4.10%
Single-wall	56.50%	-	39.90%	3.60%

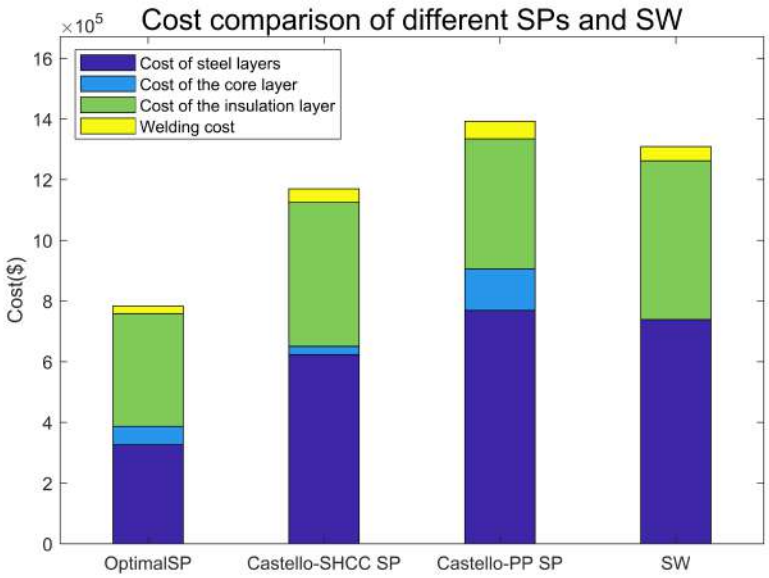

Figure 5.5: Cost comparison of SPs and SW

As shown in Figure 5.5, the optimal SP has the minimum cost. Comparing with the existing SP design procedure, the proposed optimization model is able to decrease the SP cost by 32.7% for the SHCC SP and 43.5% for the PP SP. Further, the cost of the optimal SP is only 60% compared with the SW. Table 5.8 gives the cost composition of each pipe configuration. For all the pipe configurations, the costs of the steel layers and the insulation layer account for large proportions of the total cost, which range from 41.6% to 56.5% and from 30.8% to 47.4%, respectively. In the meantime, the welding cost and the cost of the core layer account for less than 5% and 10%. Due to the low cost, the good structural, and adequate thermal insulation functionalities of the SHCC material, the optimization model selected the SHCC as the core material and increased the thickness of the core layer to the upper limit. In this way, the optimal SP configuration has the lowest cost among all the pipe configuration by reducing the costs of the steel layers, the insulation layer, and the welding process.

The optimization model showed promising performance in finding the optimal SP configuration among the wide range of thicknesses and materials. Note that, without proper design procedure, the SP solution could be more expensive than the SW solution. In this case study, the SP with PP core designed by the existing procedure is 1.06 times that of the SW.

5.3 Parametric study

5.3.1 Parameter range

The established optimization model was employed for a parametric study where the optimal SP configurations under different working conditions were discussed. Similar to the case study, T_{wax} and $T_{hydrate}$ were assumed independent of the fluid properties and the fluid properties were shown in Table 5.4. Different combinations of the input parameters $(T_{in}, M_f, D_1, L, h_{wd},\ T_{wax}, T_{hydrate}, t_{require})$ representing different working condition were established as follows.

For the parametric study to focus on the practical working conditions, the different positions of the pipelines in a subsea production system should be discussed first. Normally, the inlet flow rate M_f and the inlet fluid temperature T_{in} of a pipeline are related to the location of the pipeline in a subsea production system, see Figure 5.6. For instance, the pipelines that connect wellhead and manifold usually have higher T_{in} and lower M_f than that of the pipelines that locate between manifold and the touch down point (TDP). Further, the diameter D_1 of a pipeline is related to the flow rate M_f, which can be defined, by Palmer et al. [136], as $D_1 = \sqrt{\frac{M_f}{500}}$ where the unit for M_f is barrel per day and for D_1 is inch. Besides, the pipeline length is related to the diameter of the pipeline, since pipelines with large diameters carrying large amounts of fluid usually need to reach places further than those pipelines with small diameters. Therefore, it is rational to define these four input parameters (T_{in}, M_f, D_1, L) based on the pipeline locations in a subsea production system.

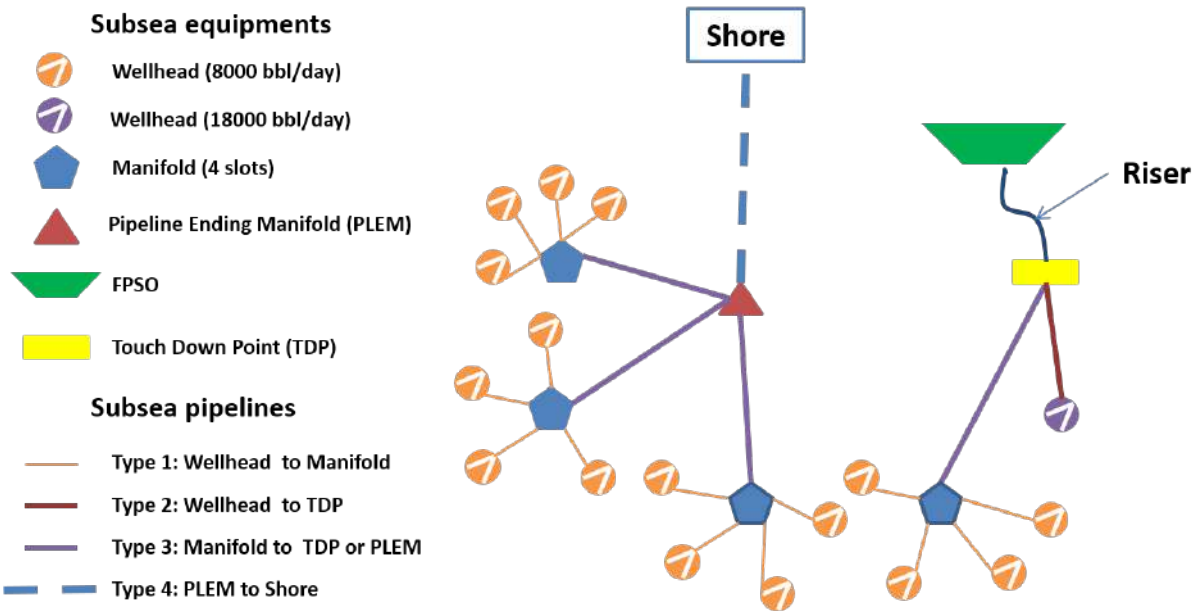

Figure 5.6: A typical subsea production system

The subsea pipelines were classified into four categories based on their locations,

which covers most subsea pipelines (Figure 5.6). 8000 bbl/day is a reasonable production rate for a subsea well, while the production rate per well can easily reach 18000 bbl/day in the pre-salt reservoir. A 4 slots manifold was assumed in the subsea production system and the three 4 slots manifolds were connected to the pipeline ending manifold (PLEM) where the fluid is transported directly to an onshore facility. The wells with 8000 bbl/day production rate were connected to the manifold and the wells with 18000 bbl/day production rate were connected to the touch down point. The wellhead temperature of all wells was assumed to 70 ℃. Considering the heat loss from wellhead to manifold, the temperature at manifold was given as 54 ℃. Likewise, the temperature at PLEM was assumed to 50 ℃. The diameters were calculated using the flow rates and the pipeline lengths were assumed based on the pipeline locations. Table 5.9 summarizes the pipeline locations and related input parameters. The rest input parameters ($h_{wd},\ T_{wax}, T_{hydrate}, t_{require}$) are independent of the locations of pipelines. Typical values representing different structural and thermal insulation requirements were assumed, see Table 5.10. The sea water temperature T_{sea} was determined by the water depth based on the thermocline of sea water in tropical area [141].

Table 5.9: Assumed input parameters and pipeline location

Locations	M_f(kg/s)	D_1(inches)	L (m)	T_{in} (C)
Type 1: Wellhead to manifold	10.4	4	1200	70
Type 2: Wellhead to Riser	23.4	6	8004	70
Type 3: 4 slots Manifold to TDP/PLEM	41.6	8	5004	54
Type 4: PLEM to Shore	124.8	14	32400	50

Note: 1 bbl/day = 0.0013 kg/s

Table 5.10: Parameter ranges for the parametric study

h_{wd} (m)	T_{sea} (℃)	T_{wax} (℃)	$T_{hydrate}$ (℃)	$t_{require}$ (h)
1000	7	39	26	8
1500	5	30	20	12
2000	4.5	21	14	16
2500	4.2			
3000	4.1			

Note: T_{sea} varies with h_{wd}

The parameters in Table 5.10 form 135 different combinations. Thus, the optimal SP configurations were calculated under 135 working conditions with different water depths and thermal insulation requirements for each pipeline location shown in Table 5.9. Totally, 540 working conditions were investigated using the established SP optimization model. For comparison purposes, the SW configurations were also developed for each working condition. For a fair comparison, a similar optimization

model of SWs was established. The structural constraint equation comes from the DNV code [125]. Other equations like cost function and thermal insulation constraint equations were obtained by simplifying the corresponding equations in the SP optimization model. The optimization model of SWs gives the SW configuration, which includes thicknesses and materials of the steel layer and the insulation layer, with minimum cost.

Note that the PIP was not included in the comparison. Due to its non-structural core layer, the PIP requires significant thickness for both its inner and outer layers to sustain loads in deep or ultra-deepwater applications. Thus, the cost for the PIP would be considerably higher than the cost of the SP or SW. In fact, the design purposes of the PIP and the SP are different. The SP was proposed to decrease the subsea pipeline cost while the PIP was proposed to provide enough thermal insulation when severe insulation requirements are encountered. Since the objective function in the established model is the pipeline cost model, it is not fair to compare the SP and the PIP in this parametric study.

5.3.2 Results and discussion

It is important to explain the method used to create the following figures, see Figures 5.7 - 5.18. The red points on each surface in these figures represent the results calculated by the SP optimization model. One of the main purposes of the parametric study is to discuss the variation tendencies of important parameters like the SP configurations and costs under different working conditions. Thus, to represent clearly the variation tendencies, linear interpolation was used to generate surfaces between the red points in 3D space under the Matlab environment [142]. Surfaces between the red points created by linear interpolation may not give the exact results but are enough to display the variation tendencies. Besides, the SP optimization model can be used to generate exact results when requested. In Figures 5.7 - 5.18, the x-axis and y-axis represent the required minimum fluid temperature ($T_{require}$) in the steady-state condition and the required minimum cool-down time ($t_{require}$) in the shut-in condition, respectively. With the z-axis represents the water depth (h_{wd}), a 3D space of the structural and thermal insulation requirements was formed representing different working conditions, where a color bar shows the value of the interested parameter like costs of the optimal SPs under corresponding working conditions. The following discussion focuses on the cases with the same hydrate appearance temperature ($T_{hydrate} = 20°C$). Thereby, the thermal insulation requirements in the shut-in condition only relate to the required cool-down time.

Note that the employed thermal requirements may not be practical for a real subsea production system. Since the temperature of the produced fluid decreases

from the upstream to the downstream in a subsea production system, the required minimum temperature for the upstream flowline (type 1, 2 and 3 pipelines) should be higher than the critical temperature (T_{wax}, $T_{hydrate}$) to avoid wax or hydrate formation in the downstream pipeline. Thus, a systematic optimization design considering the whole subsea production system is necessary for a real application.

Type 1 pipeline: Wellhead to Manifold In a subsea production system, a type 1 pipeline, connecting a wellhead and a manifold, normally has a smaller diameter, a lower flow rate, higher inlet temperature, and moderate length. Figure 5.7 shows the costs and the constraints violations of the optimal SPs at type 1 location under different working conditions. As shown in Figure 5.7-a, the cost slightly increases along with the water depth (h_{wd}). The cost remains unchanged with the increases of the required minimum temperature ($T_{require}$) while an increase of the required cool-down time ($t_{require}$) significantly increases the cost of the optimal SP. Figures 5.7-b, 5.7-c and 5.7-d explain the variation tendencies of the cost with respect to h_{wd}, $T_{require}$, and $t_{require}$ by displaying the constraint violation values. The Equations 5.17, 5.18 and 5.19 define that the constraint violation values cannot be positive. By definition, a zero violation value indicates that the designed SP can just meet the corresponding design requirement, while a negative violation value means that the designed SP is able to meet a higher design requirement. For an SP configuration with a negative constraint violation value, the adjustment of the SP configuration is not necessary until the design requirement exceeds the corresponding capacity of the SP. As shown, the violation values of the structural constraint (Figure 5.7-b) and the steady-state insulation constraint (Figure 5.7-c) remain negative. Thus, the cost and configuration of the optimal SP are not sensitive to the variations of h_{wd} and $T_{require}$. In contrast, the violation values of the thermal insulation constraint in the shut-in condition equal zero for all the cases (Figure 5.7-d). The optimal SP can just meet the required cool-down time and needs adjustment with the increase of $t_{require}$. Therefore, the cost of the optimal SP varies along with $t_{require}$. In this case, $t_{require}$ is referred as the principal design requirement.

Figure 5.8 displays the layer thicknesses of the optimal SPs under different working conditions. In Figure 5.8-a, the thickness of the inner steel layer (t_1) increases along with h_{wd} and $t_{require}$. And t_1 barely varies with respect to $T_{require}$. In Figure 5.8-b, the thickness of the core layer (t_2) stays close to its lower bound (lb_2) for most optimal SPs. It is interesting to see that the thickness of the outer steel layer (t_3) equals 2 mm, which is the lower bound, for all the cases (Figure 5.8-c). It shows that the thicknesses of the outer steel layer and the inner steel layer are not necessarily the same. In Figure 5.8-d, the thickness of the insulation layer (t_4) varies from 62.5 mm to its upper bound (ub_4). The variation of t_4 is mostly in-

fluenced by $t_{require}$. Table 5.11 shows the employment frequency of each material by the optimal SP configuration in all cases. As shown in the column of type 1 pipeline, X60 steel was employed by the optimal SP for the steel layers in 95.56% of all the working conditions while X70 and X80 steels were barely employed. For the core layer, the employment frequency of SHCC (66.67%) is two times of that of PP (33.33%). Due to its cheap price, rubber was employed by the optimal SP under 53.33% of all the investigated conditions while syntactic epoxy was not employed under any investigated conditions.

Figure 5.9 shows the cost ratio of the optimal SPs and the optimal SWs under different working condition. As shown, at 1000m of water depth, the cost ratio is higher than 1.1 indicating that the optimal SP is more expensive than the optimal SW. With the increase of water depth, the cost ratio slightly decreases. However, the cost ratios of all the investigated cases range from 0.98 to 1.12, which indicates that the replacing SWs by SPs for the type 1 pipeline cannot reduce the pipeline cost.

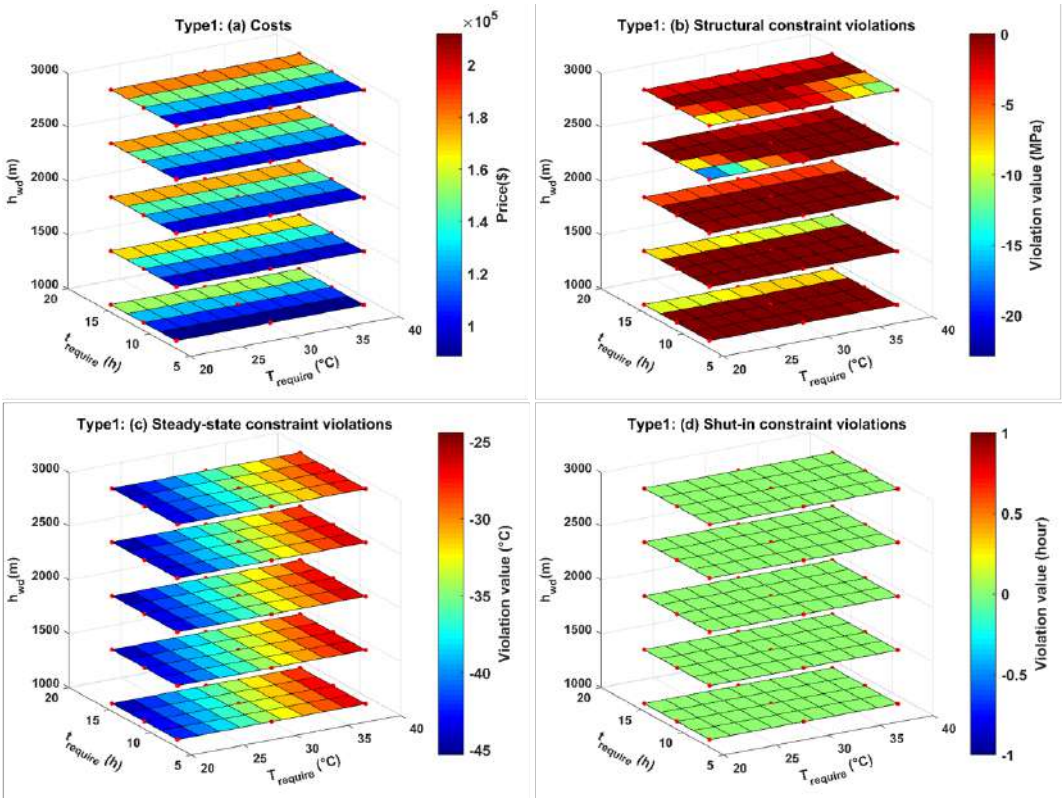

Figure 5.7: Costs and constraints violations of the optimal SPs at type 1 location under different working conditions ($T_{hydrate} = 20°C$): (a) Costs; (b) Structural violation; (c) Steady-state violation; (d) Shut-in violation

Type 2 pipeline: Wellhead to Riser For subsea wells with a high production rate, the produced fluid can be transported directly to an FPSO through a subsea

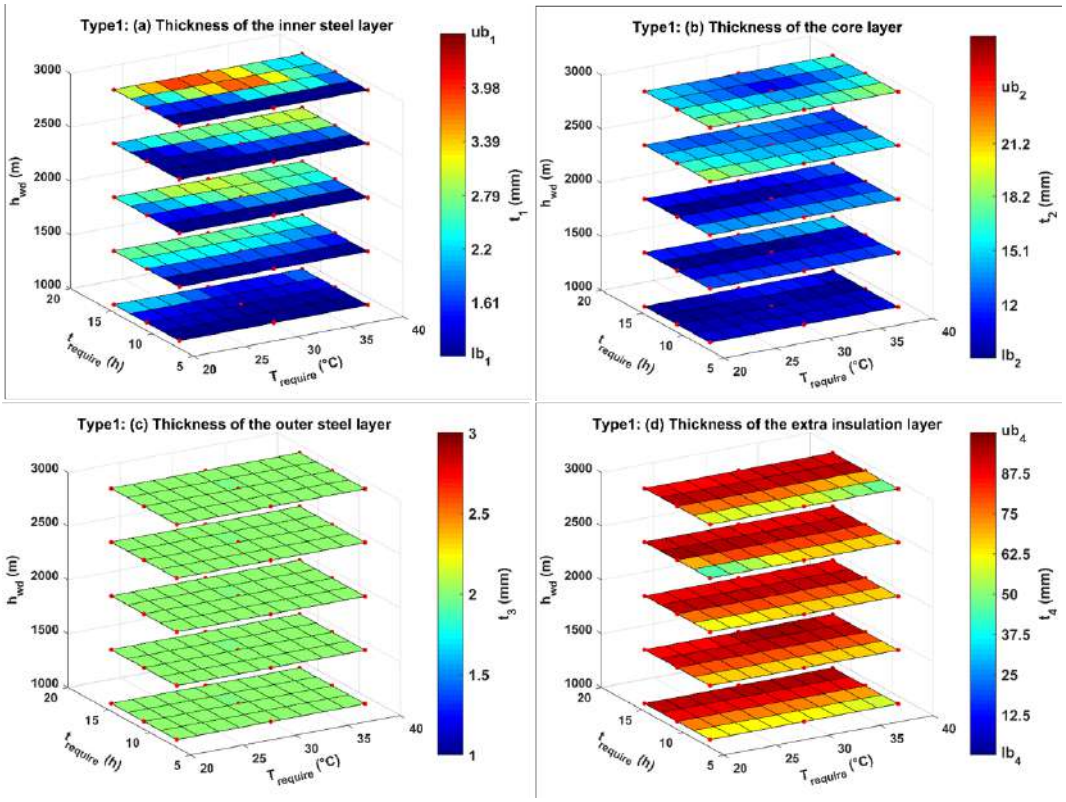

Figure 5.8: Thicknesses of each layer of the optimal SPs at type 1 location under different working conditions ($T_{hydrate} = 20°C$): (a) t_1; (b) t_2; (c) t_3; (d) t_4

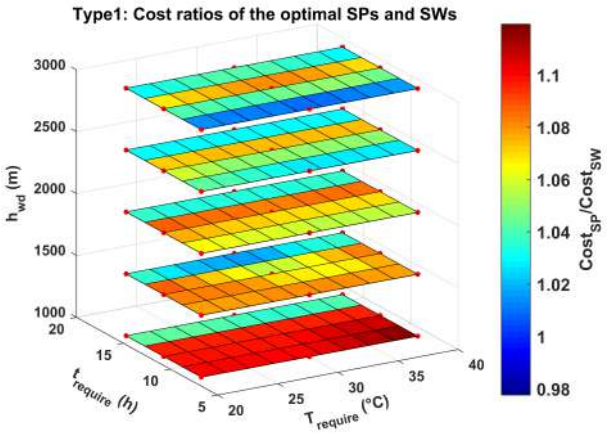

Figure 5.9: Cost ratios of the optimal SPs and the optimal SWs at type 1 location under different working conditions ($T_{hydrate} = 20°C$)

pipeline and a riser. This scenario is normal in the pre-salt reservoir of Brazil. Type 2 pipeline represents the subsea pipeline in this situation. Figure 5.10 shows the cost and the constraints violations of the optimal SP at type 2 location under different working conditions. Similar to type 1 location, $t_{require}$ is the principal design requirement and dominates the cost of the optimal SP while the influences of h_{wd} and $T_{require}$ on the cost are negligible.

Table 5.11: Employment frequency of each material in the optimal SP configurations at 4 types of location

Material parameter	Steel grade	EF (Type 1)	EF (Type 2)	EF (Type 3)	EF (Type 4)
1	X60	95.56%	100.00%	100.00%	100.00%
2	X70	4.44%	0.00%	0.00%	0.00%
3	X80	0.00%	0.00%	0.00%	0.00%
Material parameter	Core material	EF (Type 1)	EF (Type 2)	EF (Type 3)	EF (Type 4)
1	SHCC	66.67%	100.00%	100.00%	100.00%
2	PP	33.33%	0.00%	0.00%	0.00%
Material parameter	Core material	EF (Type 1)	EF (Type 2)	EF (Type 3)	EF (Type 4)
1	SPP	28.89%	71.11%	64.44%	37.78%
2	Rubber	53.33%	0.00%	0.00%	26.67%
3	Syntactic epoxy	0.00%	0.00%	0.00%	0.00%
4	PP	17.78%	28.89%	35.56%	35.56%

Note: (1) EF = Employment frequency of each material;
(2) Statistics includes all the data points at $T_{hydrate} = 20$℃

Figure 5.11 and Table 5.11 display the thickness and material of each layer of the optimal SP at type 2 location, respectively. As shown in Figure 5.11-a and 5.11-c, t_1 and t_3 of the optimal SPs stay at their lower bounds, which indicates that applying thin steel layers to SP is critical to cost-saving. In contrast, t_2 of the optimal SP varies near its upper bounds which means a thick core layer of an SP is preferable for cost reduction (Figure 5.11-b). The value of t_4 varies along with the $t_{require}$ (Figure 5.11-d) showing the main reason of the variation of cost in Figure 5.10-a. Table 5.11 shows that, for type 2 pipeline, all the optimal SPs employed X60 steel for the steel layers and SHCC for the core layer. And syntatic polypropylene and polypropylene, with 71.11% and 28.89% of employment frequency, are preferred insulation material for the optimal SPs at type 2 location.

Figure 5.12 shows the cost ratios of the optimal SPs and the optimal SWs for type 2 pipeline. It can be seen that the cost ratio decreases with the increase of h_{wd} or the decrease of $t_{require}$. The minimum cost ratio reaches 0.7 with $h_{wd} = 3000$ and $t_{require} = 8$. In general, the application of SPs for type 2 pipeline results in lower cost that the application of SWs. The cost-saving effect is small for the application of water depth at 1000m and it increases considerably with the increase of water depth.

Type 3 pipeline: Manifold to PLEM/TDP As a flow section after the subsea manifold, the type 3 pipeline is quite common in a subsea production system. Similar

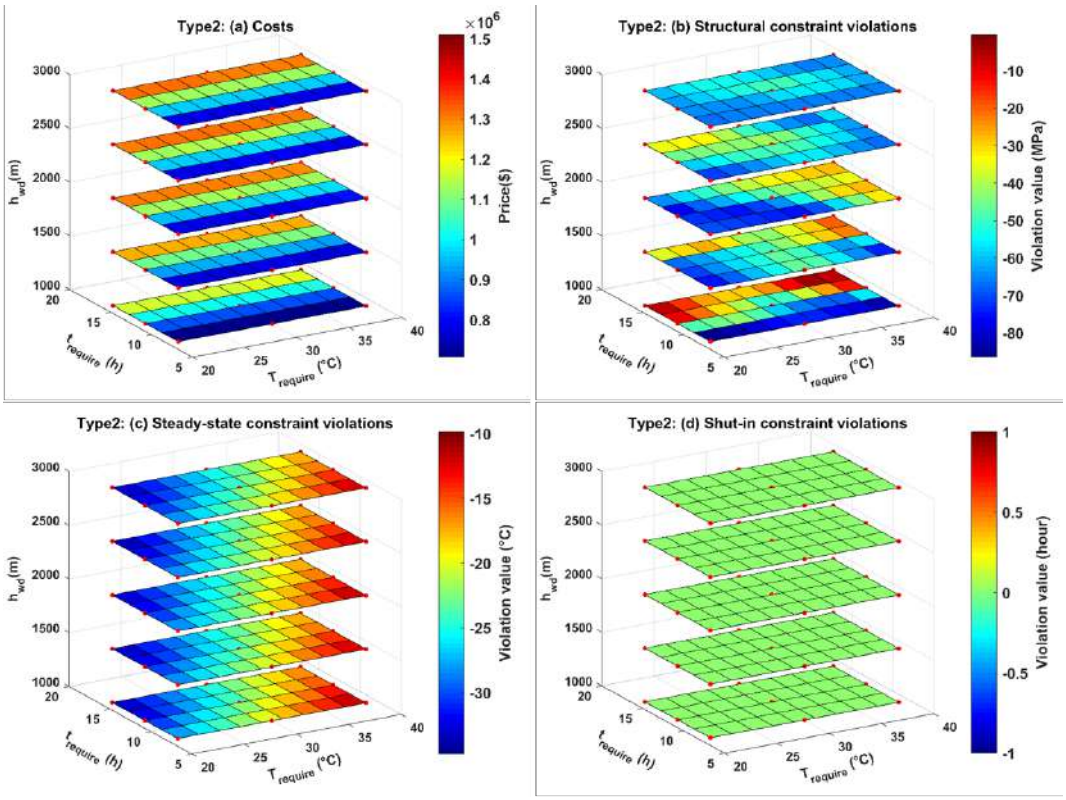

Figure 5.10: Costs and constraints violations of the optimal SPs at type 2 location under different working conditions ($T_{hydrate} = 20°C$): (a) Costs; (b) Structural violation; (c) Steady-state violation; (d) Shut-in violation

to type 1 and type 2 pipelines, the cost variation of the optimal SP is dominated by $t_{require}$ and is slightly influenced by h_{wd}, see Figure 5.13-a. Figures 5.13-b, 5.13-c and 5.13-d illustrate that $t_{require}$ is the primary design requirement which mainly decides the cost of the optimal SP.

Figure 5.14 gives the thicknesses of each layer of the optimal SPs at type 3 location. A similar pattern was observed, the thicknesses of the steel layers equal their lower bounds (Figures 5.14-a and 5.14-c) while the thickness of the core layer stays at its upper bound (Figure 5.14-b). Figure 5.14-d shows that the insulation layer thickness primarily varies along with $t_{require}$. In the type 3 column of Table 5.11, X60 steel and SHCC were employed for the steel layers and the core layer in all the optimal SPs. Syntatic polypropylene and polypropylene, with 64.44% and 35.56% of employment frequency, are the preferred insulation materials for the optimal SP at type 3 location.

By displaying the cost ratios, Figure 5.15 marks the preferred application conditions of SPs. The cost ratio of the optimal SPs and the optimal SWs varies from 0.45 to 0.83, which illustrates promising benefits of applying SPs for type 3 pipelines. With $h_{wd} = 3000$ and $t_{require} = 8$, replacing SWs by SPs for type 3 pipeline could save the pipeline cost up to 55%.

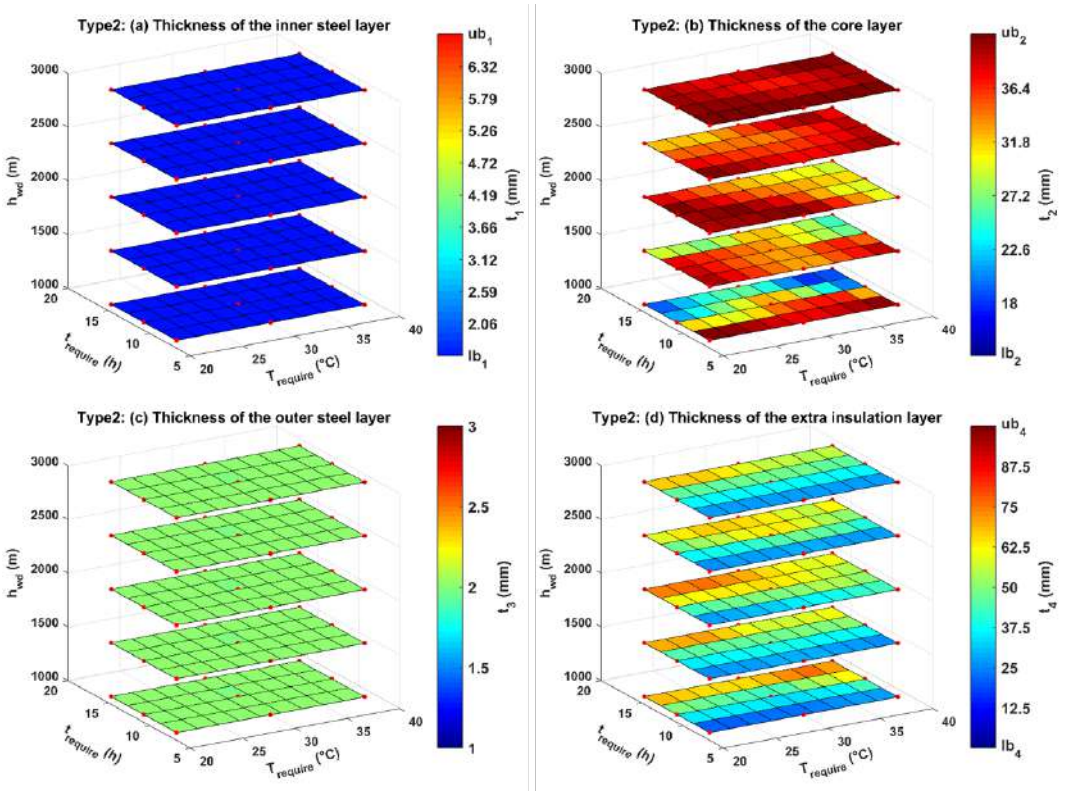

Figure 5.11: Thicknesses of each layer of the optimal SPs at type 2 location under different working conditions ($T_{hydrate} = 20°C$): (a) t_1; (b) t_2; (c) t_3; (d) t_4

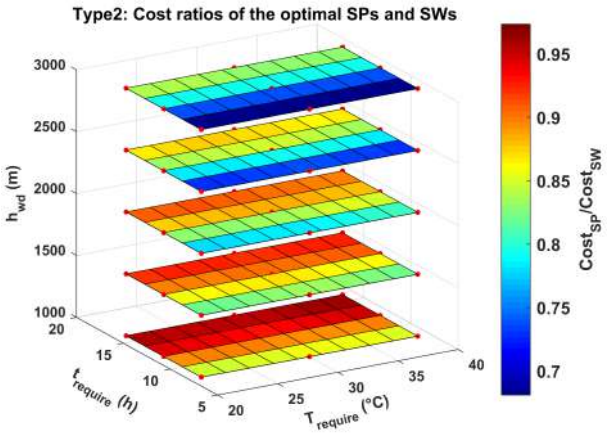

Figure 5.12: Cost ratios of the optimal SPs and the optimal SWs at type 2 location under different working conditions ($T_{hydrate} = 20°C$)

Type 4 pipeline: PLEM to Shore Type 4 pipeline is a long pipeline with a large diameter that transports a large amount of produced fluid. Type 4 pipeline can be employed in a subsea-to-shore scenario or in a common subsea production scenario where a long tieback is needed. In Figure 5.16-a, the cost of the optimal SPs slightly increases with the increase of h_{wd} or $t_{require}$. The cost of the optimal SPs increases considerably along with $T_{require}$ when $T_{require} > 30$. Figures 5.16-b, 5.16-c,

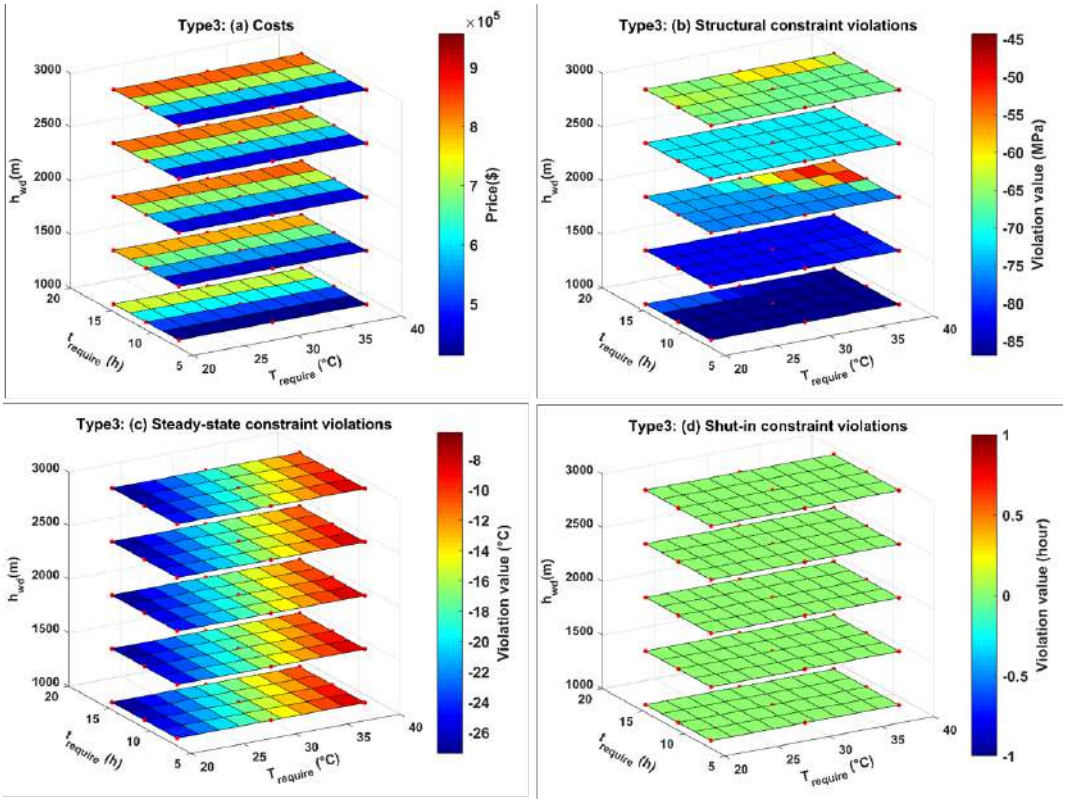

Figure 5.13: Costs and constraints violations of the optimal SPs at type 3 location under different working conditions ($T_{hydrate} = 20°C$): (a) Costs; (b) Structural violation; (c) Steady-state violation; (d) Shut-in violation

and 5.16-d explain the variation tendency of the optimal SP cost. The structural constraint violation remains negative for all the cases (Figures 5.16-b) indicates that the structural design requirement would not dominate the optimal SP configuration until the structural requirement exceed the structural strength of the current optimal SP. It is interesting to see that, unlike the previous pipeline types, $t_{require}$ is not the principle design requirement under all the working conditions. $T_{require}$ becomes the principle design requirement when $T_{require} > 30$ and dictates the optimal SP cost. The fact that type 4 pipeline has a huge length (32400 m) causes considerable heat loss of the fluid during transportation in the steady-state condition. Thus, ensuring that $T_{\min} >= T_{require}$ becomes challenging for the SP when $T_{require}$ increases.

Figure 5.17 and Table 5.11 show the optimal SP configurations under different working conditions. Again, a similar design pattern was observed, the thicknesses of the steel layers are kept to their lower bounds (Figure 5.17-a and 5.17-c) while the thickness of the core layer is kept to its upper bound (Figure 5.17-b). Figure 5.17-d shows that, when $T_{require} \leq 30$, the optimal SP needs small or no extra insulation layer. The type 4 pipeline column in Table 5.11 displays similar material choices made by the optimization model for the type 4 pipeline to that of other types of pipelines. The X60 steel for the steel layers and the SHCC for the core layer. The

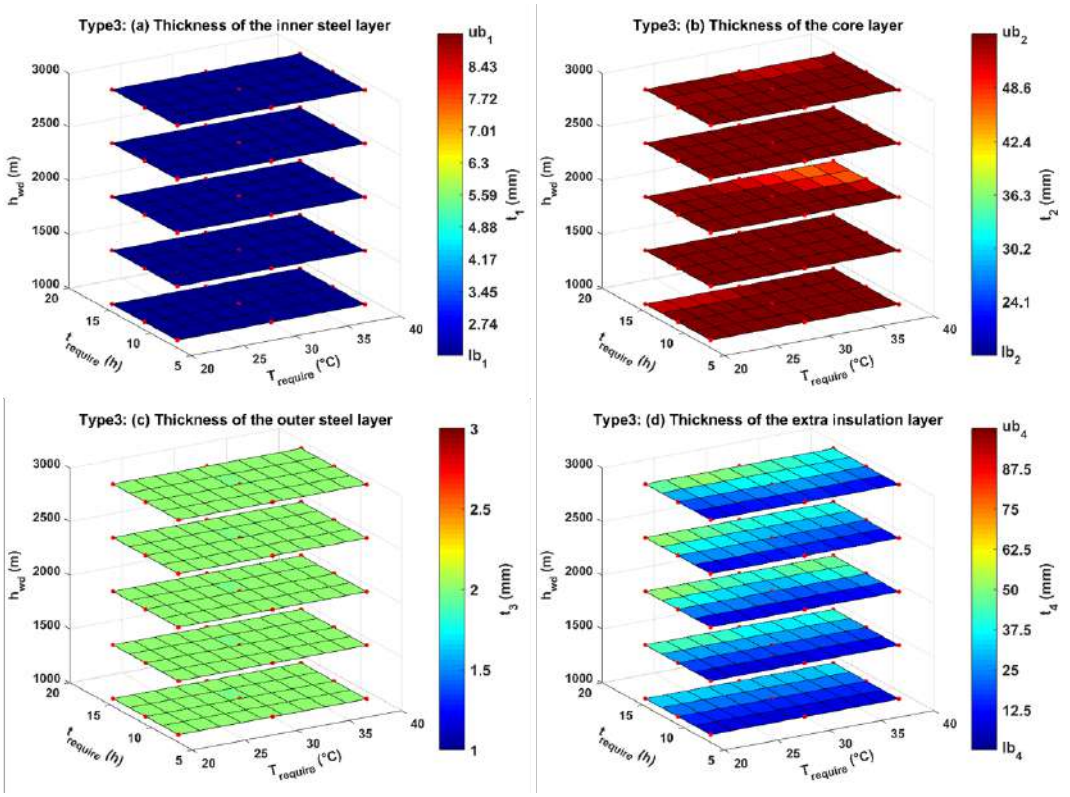

Figure 5.14: Thicknesses of each layer of the optimal SPs at type 3 location under different working conditions ($T_{hydrate} = 20°C$): (a) t_1; (b) t_2; (c) t_3; (d) t_4

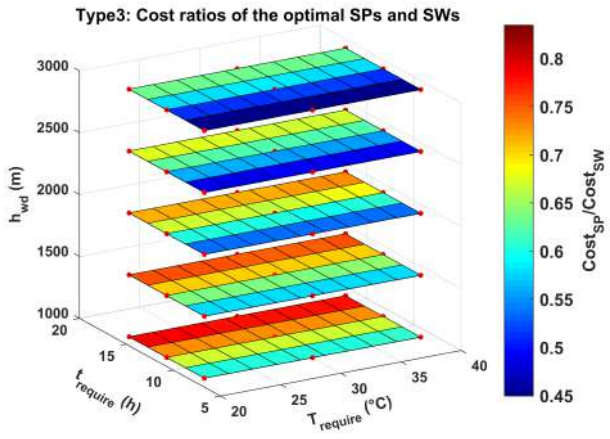

Figure 5.15: Cost ratios of the optimal SPs and the optimal SWs at type 3 location under different working conditions ($T_{hydrate} = 20°C$)

extra insulation layer employed syntatic polypropylene (37.78%), rubber (26.67%) and polypropylene (35.56%).

Figure 5.18 marks the preferred application conditions of the SPs. As shown, SPs exhibit substantial advantages over SWs for the type 4 pipeline with the cost ratio of SPs and SWs ranges from 0.25 to 0.74. The cost ratio decreases substantially with the increase of h_{wd}. Even with the small water depth ($h_{wd} = 1000$), replacing SWs

by SPs would result in cost reduction ranges from 45% to 60%. For ultra-deepwater ($h_{wd} = 3000$), the cost of SPs is only 25% to 45% of the SW cost.

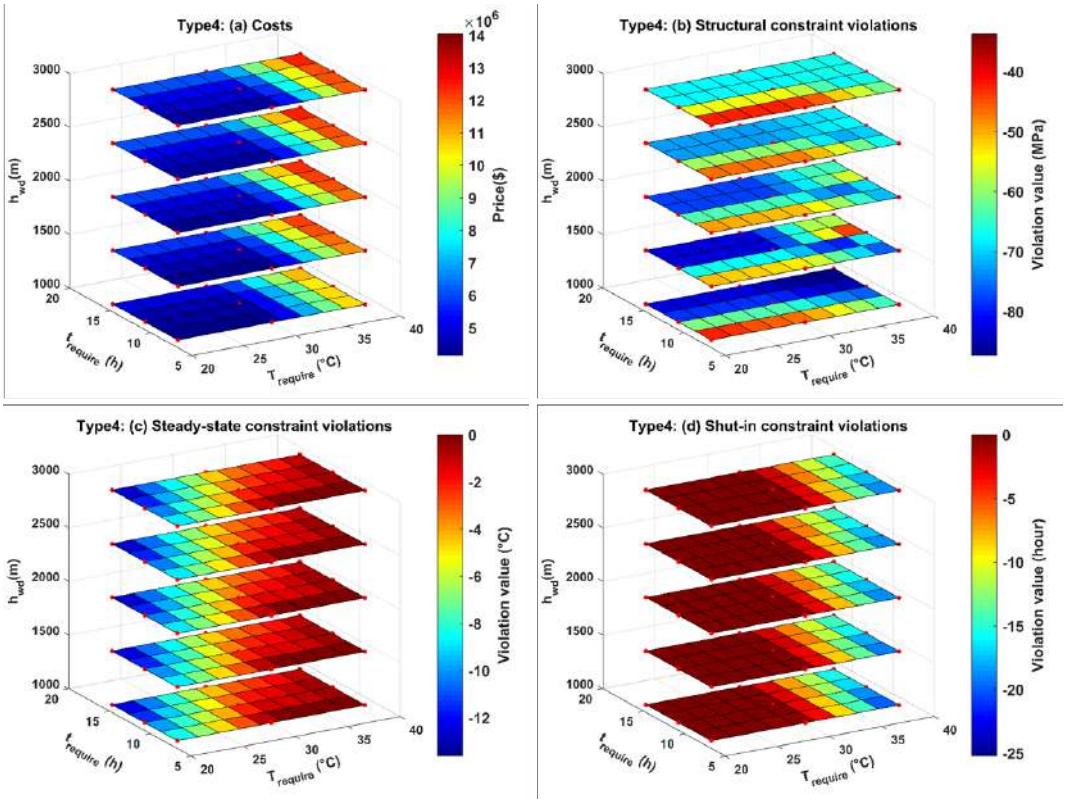

Figure 5.16: Costs and constraints violations of the optimal SPs at type 4 location under different working conditions ($T_{hydrate} = 20°C$): (a) Costs; (b) Structural violation; (c) Steady-state violation; (d) Shut-in violation

5.4 Summary

The contributions and conclusions of this chapter can be summarized as follows.

1. A cost model of SPs, including the costs of material and fabrication for each layer and the welding cost, was proposed.

2. An MINLP model for the SP optimal design was developed. Several stochastic optimization algorithms were tested for a robust solution to the proposed model. The GA-PSO algorithm was proven to perform stable and robust.

3. Using typical input parameters, a case study was conducted to verify the optimization model by comparing its results with the SPs and SW obtained from previous design procedures. The proposed optimization model was able to decrease the SP cost by 32.7% for the SHCC SP and 43.5% for the PP SP. Further, the cost of the optimal SP is only 60% of that of the SW.

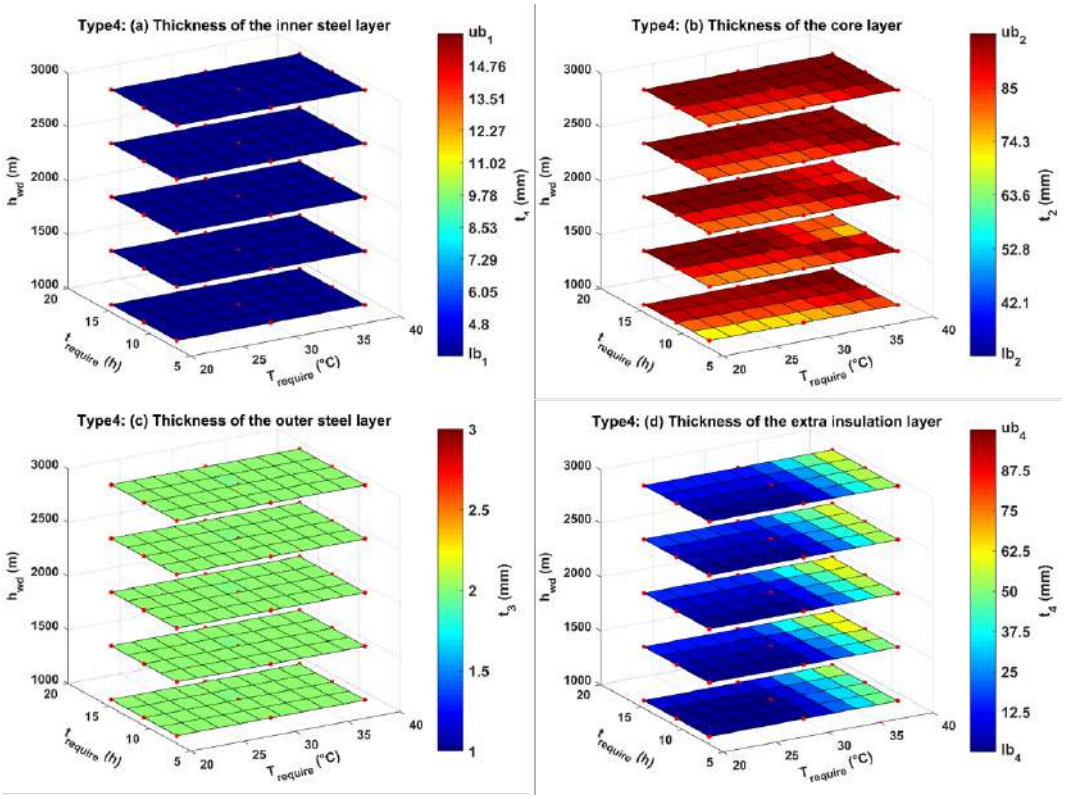

Figure 5.17: Thicknesses of each layer of the optimal SPs at type 4 location under different working conditions ($T_{hydrate} = 20°C$): (a) t_1; (b) t_2; (c) t_3; (d) t_4

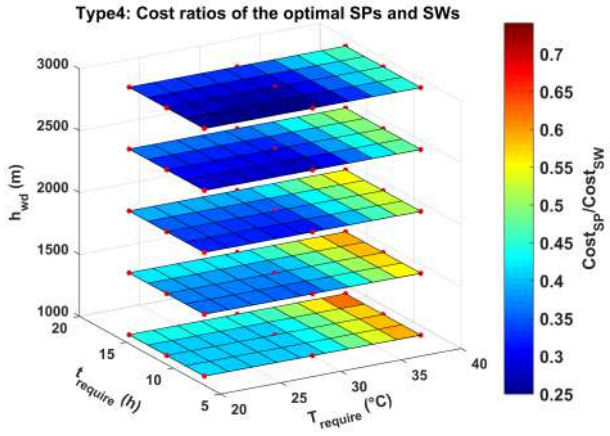

Figure 5.18: Cost ratios of the optimal SPs and the optimal SWs at type 4 location under different working conditions ($T_{hydrate} = 20°C$)

4. The optimal SP configurations under different working conditions were investigated. Due to the abundance of the input parameters, the subsea pipelines were categorized into four types so that the length, diameter, inlet fluid temperature, and the mass flow rate of the pipeline are defined in practical application ranges. For each pipeline type, the calculation results were visualized by 3D surfaces. Through the parametric study, some insights were obtained,

as described below.

- *Performance improvement*
  Figures 5.7, 5.10, and 5.13 show that the costs of the optimal SPs are mainly affected by the required cool-down time ($t_{require}$). All the shut-in constraint violations equal zero, indicating that the optimal SPs can just meet the shut-in design requirement. Thus, for SPs at types 1, 2, and 3 locations, the required cool-down time ($t_{require}$) is the principal design requirement. For the SP at type 4 location, the principal design requirement changes from $t_{require}$ to $T_{require}$ when $T_{require} > 30$ (Figure 5.16). Meanwhile, the increase of the water depth hardly influences the SP costs. The structural constraint violations, in most cases, are negative values. Figures 5.7, 5.10, 5.13, and 5.16 illustrate that, for the investigated cases, thermal insulation requirements like $t_{require}$ and $T_{require}$ are more challenging than the structural requirement for the SP. To satisfy the thermal insulation requirements, the optimal SP inevitably employed a thick core layer which results in an SP with the structural strength that exceeds the structural design requirement. In this sense, the high structural strength is low efficient. Besides, a thick core layer can create installation problems. Thus, the proposal of new materials, with adequate structural properties, to improve the thermal insulation performance, especially in the shut-in condition, is promising for a further improvement of the SP optimal design. Cementitious composites that incorporate phase change material could be a wise direction, but the SP final cost must be controlled.

- *SP design with current materials*
  Based on the observation of the SP optimal configurations some points are emphasized. The thickness of the inner steel layer not necessarily equals the thickness of the outer steel layer (Figure 5.8-a). The steel layers should be as thin as possible in most cases. X-60 steel grade is more efficient in cost than both X-70 and X-80. A thick core layer is helpful for an economical design since the core material provides both structural and thermal insulation functionalities. And SHCC is more efficient than the PP as the core material for most of the cases. Syntactic epoxy is not suitable for the SP insulation layer due to the high cost. The other three insulation materials were employed in the SP optimal configurations. No obvious pattern exists to define the material and thickness of the insulation layer.

- *Insights on the preferred working conditions of SPs*

SP is not suitable for pipelines with a small diameter. For the type 1 pipeline with 4 inches of the innermost diameter, SPs can be even more expensive than SWs. However, for pipelines with diameters beyond 6 inches, the advantage of applying SPs becomes noticeable. For the type 4 pipeline with 14 inches of the innermost diameter, the cost ratio of SPs and SWs ranges from 0.25 to 0.74. Further, the cost ratio decreases with the increase of the water depth, indicating that replacing SWs by SPs in deeper water yields higher cost reduction. The cost ratio is smaller for the cases with lower $t_{require}$ and $T_{require}$, which means that working conditions with lower thermal insulation requirements are preferable for SPs. In general, the preferred application condition of SPs includes large pipeline diameter (larger than 6 inches), large water depth, and low thermal insulation requirements. In this study, the minimum cost ratio of SPs and SWs reached 0.25 which shows a high potential for SPs in deep-water applications.

5. The proposed optimization model considers three design constraints based on structural strength and thermal behavior. However, in an actual application, more constraints associated with the installation process and the corrosion problem under operational conditions should be included.

Chapter 6

Conclusion and future work

6.1 Overall summary

Sandwich pipes have been studied for decades. It is proven to be a promising solution in deepwater applications. However, a proper design method, which is critical for the SP application, has not been reported yet. This thesis made efforts to develop an optimal SP design model considering structural and thermal insulation requirements. To be specific, an optimization model was proposed with constraints including the required SP collapse pressure under the corresponding water depth, the minimum working temperature in the steady-state condition, and the required cool-down time in the shut-in condition.

On the structural strength aspect, a finite element model correlated by experimental results was established for the SHCC SP collapse simulation. A parametric study consist of 6000 cases was conducted to analyze the collapse pressure and post-buckling behavior of SHCC SPs with different configurations, where the effects of the thickness and ovality of each layer and the steel grade on the collapse behavior were investigated. The accuracies of the previous analytical solutions for the SP collapse pressure were evaluated by the experimental results. Based on machine learning, a wide range of equation forms were tested for a suitable prediction equation of the SP collapse pressure.

On the thermal insulation aspect, a comparative study was carried out in the OLGA software to analyze the insulation performance of the SHCC SP. The relationship between the thermal properties of the SP core layer and the SP insulation performance was investigated. Further, a mathematical model for heat transfer analysis in a multilayer pipeline was developed and verified against the simulation results by the OLGA software.

Finally, an MINLP model was established for the SP optimization. A case study was conducted to test the optimization model. A parametric study, which covers

most of the working conditions for subsea pipelines, was finished to investigate the optimal SP configurations under different application scenarios.

6.2 Conclusion

Since most of the findings are presented in the summary section of each chapter, the major findings and contributions of the thesis are summarized below.

A special collapse behavior of SHCC SPs and a new collapse mechanism The parametric study in section 3.1.3 revealed a special collapse behavior of SHCC SPs. When applying a thicker outer steel layer to an SHCC SP, the collapse pressure may, depending on the SP configurations, decrease or increase, or decrease first, then increase. This particular phenomenon was comprehensively discussed. Since the outside radius was fixed with the variation of the pipe thickness, an SP with a thicker outer steel layer would have a thinner core layer. Thus, an increase of the outer steel layer thickness would increase the strength of the outer steel layer and reduce the strength of the core layer. With the frictionless inter-layer condition, the structural strength and characteristic response of the SP system were found more related to its strongest layer rather than the summation of all layers. Further, due to relatively high Young's modulus of the SHCC, a thick core layer could be the strongest layer of an SP. Variation in the outer steel layer thickness could induce the transformation of the strongest layer from the core layer to the outer steel layer. Consequently, the collapse pressure of the whole SP system is not monotonic correlated to the thickness of the outer steel layer. The same behavior has never been reported in previous studies since SPs with PP cores have a fully bonded inter-layer condition and a low core layer stiffness. It can be inferred that this collapse mechanism holds not only for the SHCC SP but also for the SPs with weak inter-layer adhesion and relatively hard core layer material.

With the newly discovered collapse mechanism of the SHCC SP, it is rational to design an SHCC SP with thinner steel layers to utilize the strength of the core layer. Also, avoiding a thick outer steel layer would be wise since it could decrease the structural strength of the whole system.

A suitable prediction equation for SHCC SPs First, the existing analytical equations were compared with the experimental results. It was observed that the analytical equations fail to give accurate predictions due to the assumptions made to simplify the problem. However, even for the simplified problem, solving the SP collapse pressure analytically is rather complex. Improving the accuracy of the analytical solutions would inevitably increase the complexity of the problem.

Therefore, the empirical equation by the regression method was adopted to propose the predict the collapse pressure of the SHCC SP.

All the existing prediction models for the SP collapse pressure did not consider the special collapse behavior revealed in this work. Thus, large deviations may occur when applying previous prediction models to the SHCC SP. Using machine learning techniques, a suitable prediction equation was proposed by testing a wide range of equation forms. The developed equation is able to capture the complex collapse behavior of the SHCC SP. Among the test data, the proposed equation is able to predict the collapse pressure with an average error of 8.47%. Moreover, the proposed equation tends to overpredict the collapse pressure for SPs with X70 or X80 steel grade when elastic buckling happens. Also, relatively large errors should be noted when applying the proposed equation to SPs with thick core and thin steel layers. Fortunately, the two areas are not the areas of design interest. Usually, the water depth for SP applications varies from 1500 to 3000 meters, which is an area (15 to 30 Mpa) in which the proposed equation performs well.

Thermal insulation performance of the SP The comparative study presented in chapter 4 reveals that the SP performs well in the steady-state condition but inadequate in the shut-in condition. The insulation performance of the SP can be improved by either reducing the thermal conductivity or raising the VHC of the core layer material. However, a lower thermal conductivity always results in the lower structural strength of a material. Special attention should be paid to the structural performance of the SP when applying core layer material with lower thermal conductivity. Moreover, it is very difficult for the common insulation material to reach a required VHC high enough to provide a good insulation performance. Incorporating PCM in the core layer could be a promising direction for better insulation performance. Interestingly, the thickness of the inner steel layer was found to have a positive influence on the thermal insulation of the SP in the shut-in condition. Due to its ideal location and a large VHC, a thicker inner steel layer could reduce the extra insulation thickness needed to provide required cool-down time. For any changes in the core layer or the inner steel layer, the structural and thermal insulation performance changes accordingly. Thus, the design for the SP should combine both structural and thermal performance with a proper evaluation function.

An SP optimization design model The optimal design model proposed in this work fills the research blank of this area. This work can be a reference for the possible design criteria of SPs in the future. The case study shows that, comparing with the existing SP design procedure, the model was able to decrease the SP cost by 32.7% for the SHCC SP and 43.5% for the PP SP. The SP cost model shows

that the steel and extra insulation layers account for a large part of the total cost, which range from 41.6% to 56.5% and from 30.8% to 47.4%, respectively. In the meantime, the welding cost and the cost of the core layer account for less than 5% and 10%.

The established model was employed to investigate the optimal SP configurations under 540 different working conditions. It was observed that the thermal insulation requirements are more challenging than the structural requirement for the SP in most cases. The optimal SP usually employs a thick core layer to meet the thermal insulation requirements at a low cost. This configuration results in a pressure capacity that exceeds considerably the structural requirement. Besides, a thick core layer could bring troubles to the installation process. For a more balanced SP design, a core material with good insulation performance and adequate structural strength is a promising direction. For the optimal SP design with current materials, the steel grade of X60 is more efficient than that of X70 and X80. Further, the SHCC is more preferred than the PP as the core layer material. Large thicknesses for both inner and outer steel layers should be avoided since increasing the steel layers' thickness would increase the steel pipe cost as well as the welding cost. By comparing the cost of the optimal SPs and the optimal SWs, the preferred working conditions for SPs were marked. The SP is not suitable for small diameter pipelines (below 4 inches), where employing SPs would lead to an even higher cost, in some cases, than the scenario with the SW. In general, the preferred application condition of SPs includes large pipeline diameter (larger than 6 inches), large water depth (beyond 1000 m), and low thermal insulation requirements (cool-down time below 8 hours), where the employment of SP can reduce the pipeline cost significantly.

6.3 Future work

For a more practical design, the following work will continue to complete the optimal design model.

- The mechanical and thermal analyses were decoupled in this study. However, the influence of the temperature on the mechanical behavior, especially for the polymeric materials, should be included for more practical analysis.
- In addition to the external hydrostatic pressure, the SP is subjected to localized loads, during the installation, such as tension, bending moments, and the loads induced by the tensioner shoes. The optimal model should include structural failure constraints considering SPs under loads during the installation process.

- In cases where the SP serves as the riser part, analyses on the structural response under dynamic loads should be included. Moreover, the fatigue analysis on the SP core layer is an important issue.
- Structural constraints should include the thermal buckling problem.
- The thermal analysis model established in this work simplifies the problem into single-phase flow. Normally, multiphase flow exists in the subsea pipeline and the inner convective heat transfer coefficient is greatly impacted by the flow regime. Thus, a more comprehensive thermal analysis model could be developed to improve the reliability of the optimal design model.
- Further, the behavior of the SP under fluid-structure interactions should be investigated when multiphase flow exists.
- Except for the structural and thermal insulation constraints, the corrosion problem should be included in the optimal design model.
- In this work, the cost model of the SP was established assuming all the SPs will be installed by reeling-lay method. However, Pipelines with large diameters could cause problems for the reeling-lay method. A cost model including the SP installed by S-lay or J-lay using SP connectors is necessary for large diameter SPs.
- A more refined cost model for the SP is critical for the optimal design.
- Risk analysis should be included in the optimization model.
- The proposed design model gives optimal configuration for a single SP. However, the optimal SP configurations of several SPs in a subsea production system remained unanswered.

In order to improve the overall performance of SPs, new materials incorporating PCM into polymeric or cementitious composite seem to be promising core materials for the SP. However, the mechanical and thermal performance of the material should be studied carefully.

Bibliography

[1] ZHANG, G., QU, H., CHEN, G., et al. "Giant discoveries of oil and gas fields in global deepwaters in the past 40 years and the prospect of exploration", *Journal of Natural Gas Geoscience*, v. 4, n. 1, pp. 1–28, 2019.

[2] CAMARGO, R., GONÇALVES, M., MONTESANTI, J., et al. "A perspective view of flow assurance in deepwater fields in Brazil". In: *Offshore Technology Conference*. Offshore Technology Conference, 2004.

[3] CARDOSO, C. B., ALVES, I. N., RIBEIRO, G. S., et al. "Management of flow assurance constraints". In: *Offshore Technology Conference*. Offshore Technology Conference, 2003.

[4] PASQUALINO, I., PINHEIRO, B., ESTEFEN, S. F. "Comparative structural analyses between sandwich and steel pipelines for ultra-deep water". In: *International Conference on Offshore Mechanics and Arctic Engineering*, v. 36142, pp. 165–173, 2002.

[5] NETTO, T., SANTOS, J., ESTEFEN, S. "Sandwich pipes for ultra-deep waters". In: *International Pipeline Conference*, v. 36207, pp. 2093–2101, 2002.

[6] ESTEFEN, S. F., NETTO, T. A., PASQUALINO, I. P. "Strength analyses of sandwich pipes for ultra deepwaters", 2005.

[7] AN, C. *Collapse of sandwich pipes with PVA fiber reinforced cementitious composites core under hydrostatic pressure*. Doctoral thesis, Federal University of Rio de Janeiro, UFRJ/COPPE, 2012.

[8] ARJOMANDI, K., TAHERI, F. "Bending capacity of sandwich pipes", *Ocean Engineering*, v. 48, pp. 17–31, 2012.

[9] CASTELLO, X., ESTEFEN, S. F., LEON, H. R., et al. "Design aspects and benefits of sandwich pipes for ultra deepwaters". In: *International Conference on Offshore Mechanics and Arctic Engineering*, v. 43437, pp. 453–459, 2009.

[10] ARJOMANDI, K., TAHERI, F. "A new look at the external pressure capacity of sandwich pipes", *Marine Structures*, v. 24, n. 1, pp. 23–42, 2011.

[11] PARANHOS BASTOS, A. *Technical-economic optimization of thicknesses of sandwich pipe walls*. D.Sc. thesis, Federal University of Rio de Janeiro, Rio de Janeiro, Brazil, 2018.

[12] YANG, J., LOURENÇO, M. I., ESTEFEN, S. F. "Thermal insulation of subsea pipelines for different materials", *International Journal of Pressure Vessels and Piping*, v. 168, pp. 100–109, 2018.

[13] HAUSNER, M., DIXON, M., OTHERS. "Optimized design of pipe-in-pipe systems". In: *Offshore Technology Conference*. Offshore Technology Conference, 2002.

[14] "OLGA 2014". .

[15] DE SOUZA, A. R., NETTO, T. A., PASQUALINO, I. P. "Materials selection for Sandwich Pipes under the combined effect of pressure, bending and temperature". In: *International Conference on Offshore Mechanics and Arctic Engineering*, v. 4269, pp. 111–122, 2007.

[16] CASTELLO, X., ESTEFEN, S. F., OTHERS. "Sandwich pipes for ultra deepwater applications". In: *Offshore Technology Conference*. Offshore Technology Conference, 2008.

[17] OGDEN, R. W. *Non-linear elastic deformations*. Courier Corporation, 1997.

[18] AN, C., CASTELLO, X., DUAN, M., et al. "Ultimate strength behaviour of sandwich pipes filled with steel fiber reinforced concrete", *Ocean engineering*, v. 55, pp. 125–135, 2012.

[19] AN, C., DUAN, M., TOLEDO FILHO, R. D., et al. "Collapse of sandwich pipes with PVA fiber reinforced cementitious composites core under external pressure", *Ocean Engineering*, v. 82, pp. 1–13, 2014.

[20] HOLSCHEMACHER, K., MUELLER, T., RIBAKOV, Y. "Effect of steel fibres on mechanical properties of high-strength concrete", *Materials & Design (1980-2015)*, v. 31, n. 5, pp. 2604–2615, 2010.

[21] LI, V. C., WANG, S., WU, C., et al. "Tensile strain-hardening behavior of polyvinyl alcohol engineered cementitious composite (PVA-ECC)", *ACI Materials Journal-American Concrete Institute*, v. 98, n. 6, pp. 483–492, 2001.

[22] FU, G., MOURA PAZ, C., HERNÁNDEZ CHUJUTALLI, J. A., et al. "Sandwich Pipes With Strain Hardening Cementitious Composites (SHCC): Numerical Analyses". In: *International Conference on Offshore Mechanics and Arctic Engineering*, v. 45462, p. V06AT04A030. American Society of Mechanical Engineers, 2014.

[23] AN, C., DUAN, M., ESTEFEN, S. F. "Collapse and buckle propagation of sandwich pipes: a review". In: *International Conference on Offshore Mechanics and Arctic Engineering*, v. 55362, p. V04AT04A015. American Society of Mechanical Engineers, 2013.

[24] TYAGI, V. V., BUDDHI, D. "PCM thermal storage in buildings: a state of art", *Renewable and sustainable energy reviews*, v. 11, n. 6, pp. 1146–1166, 2007.

[25] SOARES, N., COSTA, J. J., GASPAR, A. R., et al. "Review of passive PCM latent heat thermal energy storage systems towards buildings' energy efficiency", *Energy and buildings*, v. 59, pp. 82–103, 2013.

[26] ZHOU, D., ZHAO, C.-Y., TIAN, Y. "Review on thermal energy storage with phase change materials (PCMs) in building applications", *Applied energy*, v. 92, pp. 593–605, 2012.

[27] ZALBA, B., MARIN, J. M., CABEZA, L. F., et al. "Review on thermal energy storage with phase change: materials, heat transfer analysis and applications", *Applied thermal engineering*, v. 23, n. 3, pp. 251–283, 2003.

[28] RAMAKRISHNAN, S., WANG, X., SANJAYAN, J., et al. "Thermal performance assessment of phase change material integrated cementitious composites in buildings: Experimental and numerical approach", *Applied Energy*, v. 207, pp. 654–664, 2017.

[29] MANKEL, C., CAGGIANO, A., KOENDERS, E. "Thermal energy storage characterization of cementitious composites made with recycled brick aggregates containing PCM", *Energy and Buildings*, v. 202, pp. 109395, 2019.

[30] NEPOMUCENO, M. C., SILVA, P. D. "Experimental evaluation of cement mortars with phase change material incorporated via lightweight expanded clay aggregate", *Construction and Building Materials*, v. 63, pp. 89–96, 2014.

[31] SATO, M., PATEL, M. H. "Exact and simplified estimations for elastic buckling pressures of structural pipe-in-pipe cross sections under external hydrostatic pressure", *Journal of marine science and technology*, v. 12, n. 4, pp. 251–262, 2007.

[32] ARJOMANDI, K., TAHERI, F. "Elastic buckling capacity of bonded and unbonded sandwich pipes under external hydrostatic pressure", *Journal of Mechanics of Materials and Structures*, v. 5, n. 3, pp. 391–408, 2010.

[33] HASHEMIAN, R., MOHAREB, M. "Finite difference model for the buckling analysis of sandwich pipes under external pressure", *Ocean Engineering*, v. 122, pp. 172–185, 2016.

[34] HASHEMIAN, R., MOHAREB, M. "Buckling finite element formulation for sandwich pipes under external pressure", *International Journal of Pressure Vessels and Piping*, v. 147, pp. 41–54, 2016.

[35] JIN, Z., SHEN, X., YAN, S., et al. "A three-dimensional analytical solution for sandwich pipe systems under linearly varying external pressures", *Ocean Engineering*, v. 124, pp. 298–305, 2016.

[36] XUE, J., WANG, Y., YUAN, D. "A shear deformation theory for bending and buckling of undersea sandwich pipes", *Composite Structures*, v. 132, pp. 633–643, 2015.

[37] SHAHGHOLIAN-GHAHFAROKHI, D., RAHIMI, G. "New analytical approach for buckling of composite sandwich pipes with iso-grid core under uniform external lateral pressure", *Journal of Sandwich Structures & Materials*, p. 1099636218821397, 2019.

[38] DE SOUZA, A. *Structural strength of sandwich pipes under external pressure, longitudinal bending and thermal loading*. Master's dissertation, Federal University of Rio de Janeiro, UFRJ/COPPE, 2008.

[39] CASTELLO, X. *Influence of adhesion between layers on the collapse resistance of sandwich pipes*. Doctoral thesis, Federal University of Rio de Janeiro, UFRJ/COPPE, 2011.

[40] CASTELLO, X., ESTEFEN, S. F., OTHERS. "Sandwich pipes for ultra deepwater applications". In: *Offshore Technology Conference*. Offshore Technology Conference, 2008.

[41] CASTELLO, X., ESTEFEN, S. "Limit strength and reeling effects of sandwich pipes with bonded layers", *International journal of mechanical sciences*, v. 49, n. 5, pp. 577–588, 2007.

[42] AN, C., CASTELLO, X., OLIVEIRA, A. M., et al. "Limit strength of new sandwich pipes with strain hardening cementitious composites (SHCC) core: Finite element modelling". In: *International Conference on Offshore Mechanics and Arctic Engineering*, v. 44908, pp. 499–506. American Society of Mechanical Engineers, 2012.

[43] ARJOMANDI, K., TAHERI, F. "Stability and post-buckling response of sandwich pipes under hydrostatic external pressure", *International Journal of Pressure Vessels and Piping*, v. 88, n. 4, pp. 138–148, 2011.

[44] ARJOMANDI, K., TAHERI, F. "The influence of intra-layer adhesion configuration on the pressure capacity and optimized configuration of sandwich pipes", *Ocean engineering*, v. 38, n. 17-18, pp. 1869–1882, 2011.

[45] HE, T., DUAN, M., WANG, J., et al. "On the external pressure capacity of deepwater sandwich pipes with inter-layer adhesion conditions", *Applied Ocean Research*, v. 52, pp. 115–124, 2015.

[46] XU, Q., GONG, S., HU, Q. "Collapse analyses of sandwich pipes under external pressure considering inter-layer adhesion behaviour", *Marine Structures*, v. 50, pp. 72–94, 2016.

[47] FERNÁNDEZ-VALDÉS, D., VÁZQUEZ-HERNÁNDEZ, A., ORTEGA-HERRERA, J., et al. "FEM-based evaluation of friction and initial imperfections effects on sandwich pipes local buckling", *Marine Structures*, v. 72, pp. 102769, 2020.

[48] "ABAQUS, 2013, "User's and Theory Manuals"". 2013.

[49] GONG, S., WANG, X., ZHANG, T., et al. "Buckle propagation of sandwich pipes under external pressure", *Engineering Structures*, v. 175, pp. 339–354, 2018.

[50] BAI, Q., BAI, Y. *Subsea pipeline design, analysis, and installation*. Gulf Professional Publishing, 2014.

[51] ESTEFEN, S. "Collapse behaviour of intact and damaged deepwater pipelines and the influence of the reeling method of installation", *Journal of Constructional Steel Research*, v. 50, n. 2, pp. 99–114, 1999.

[52] PAZ, C. M., FU, G., ESTEFEN, S. F., et al. "Sandwich pipe: reel-lay installation effects". In: *International Conference on Offshore Mechanics and Arctic Engineering*, v. 56529, p. V05BT04A033. American Society of Mechanical Engineers, 2015.

[53] JOSÉ LUIS PÁRRAGA, Q. *Design and Threaded Connector Analysis for Sandwich Pipe*. Master's dissertation, Federal University of Rio de Janeiro, UFRJ/COPPE, 2016.

[54] ONYEGIRI, I., KASHTALYAN, M. "Finite element analysis of a sandwich pipe joint", *Ocean Engineering*, v. 146, pp. 363–374, 2017.

[55] ONYEGIRI, I., KASHTALYAN, M. "Threaded connectors for sandwich pipes–Part 1: Parametric & comparative studies", *International Journal of Pressure Vessels and Piping*, v. 168, pp. 117–124, 2018.

[56] ONYEGIRI, I., KASHTALYAN, M. "Threaded connectors for sandwich pipes–Part 2: Optimisation of stress relief groove", *International Journal of Pressure Vessels and Piping*, v. 168, pp. 125–131, 2018.

[57] ONYEGIRI, I., KASHTALYAN, M. "Engineering critical assessment for a sandwich pipe field joint", *Ocean Engineering*, v. 172, pp. 788–802, 2019.

[58] SU, J. "Flow assurance of deepwater oil and gas production: a review". In: *International Conference on Offshore Mechanics and Arctic Engineering*, v. 36827, pp. 601–620, 2003.

[59] KAISER, M. J. *The Offshore Pipeline Construction Industry: Activity Modeling and Cost Estimation in the US Gulf of Mexico*. Gulf Professional Publishing, 2020.

[60] GREALISH, F., RODDY, I. "State-of-the-art on deep water thermal insulation systems". In: *International Conference on Offshore Mechanics and Arctic Engineering*, v. 36134, pp. 339–347, 2002.

[61] COLLINS, M. "Thermal insulation materials for subsea flowlines", *Materials & Design*, v. 10, n. 4, pp. 168–174, 1989.

[62] LE GAC, P., CHOQUEUSE, D., MELOT, D., et al. "Life time prediction of polymer used as thermal insulation in offshore oil production conditions: Ageing on real structure and reliability of prediction", *Polymer testing*, v. 34, pp. 168–174, 2014.

[63] HALLOT, R., COUPRIE, S., CHOMARD, A., et al. "Ils-A Passive Insulation Solution To Answer Cool Down Time Challenges On Deep Water Flowlines". In: *Offshore Technology Conference*. Offshore Technology Conference, 2002.

[64] ALAWADHI, E. M. "Thermal analysis of a pipe insulation with a phase change material: Material selection and sizing", *Heat transfer engineering*, v. 29, n. 7, pp. 624–631, 2008.

[65] WANG, H., DUAN, M., AN, C., et al. "Investigation of thermal behavior of long-distance multilayer pipeline with MicroPCM particles", *International Journal of Heat and Mass Transfer*, v. 153, pp. 119605, 2020.

[66] SU, J., REGIS, C. R., BOTTO, A. "Thermal analysis of combined active heating and passive insulation of deepwater pipelines". In: *International Conference on Offshore Mechanics and Arctic Engineering*, v. 36142, pp. 185–190, 2002.

[67] SU, J., CERQUEIRA, D. R., ESTEFEN, S. F. "Thermal analysis of sandwich pipes with active electrical heating". In: *International Conference on Offshore Mechanics and Arctic Engineering*, v. 36827, pp. 809–814, 2003.

[68] NYSVEEN, A., KULBOTTEN, H., BOMES, A., et al. "Direct electrical heating of subsea pipelines-technology development and operating experience". In: *Record of Conference Papers Industry Applications Society 52nd Annual Petroleum and Chemical Industry Conference*, pp. 177–187. IEEE, 2005.

[69] VERDEIL, J., GIRAUDBIT, S., SILCOCK, D., et al. "Combining the Most Efficient Active Heating Technology with Subsea Electrical Distribution to Develop Remote Resources". In: *Offshore Technology Conference*. Offshore Technology Conference, 2017.

[70] ESTEFEN, S. F., LOURENÇO, M. I., FENG, J., et al. "Sandwich pipe for long distance pipelines: flow assurance and costs". In: *International Conference on Offshore Mechanics and Arctic Engineering*, v. 49965, p. V005T04A025. American Society of Mechanical Engineers, 2016.

[71] BARRERA ESCOBEDO, J. J., NIECKELE, A. O., AZEVEDO, L. F. A. "Analysis of the Transient Cooldown of Sub-Sea Pipelines". In: *International Pipeline Conference*, v. 42614, pp. 845–853, 2006.

[72] SU, J., CERQUEIRA, D. "Simulation of transient heat transfer in multilayered composite pipeline". In: *Proceeding of OMAE01, 20nd International Conference on Offshore Mechanics and Arctic Engineering, June*, pp. 3–8, 2001.

[73] SU, J., CERQUEIRA, D. R., ESTEFEN, S. F. "Simulation of transient heat transfer of sandwich pipes with active electrical heating", 2005.

[74] AN, C., SU, J. "Improved lumped models for transient combined convective and radiative cooling of multi-layer composite slabs", *Applied Thermal Engineering*, v. 31, n. 14-15, pp. 2508–2517, 2011.

[75] KAYHANI, M., NOROUZI, M., DELOUEI, A. A. "A general analytical solution for heat conduction in cylindrical multilayer composite laminates", *International Journal of Thermal Sciences*, v. 52, pp. 73–82, 2012.

[76] ZULKEFLI, N., PAO, W. *Optimum Thermal Insulation Design for Subsea Pipeline Flow Assurance*. Technical report, Technical Report, Universiti Teknologi PETRONAS, Malaysia, 8pp, 2016.

[77] JANOFF, D., MCKIE, N., DAVALATH, J., et al. "Prediction of cool down times and designing of insulation for subsea production equipment". In: *Offshore Technology Conference*. Offshore Technology Conference, 2004.

[78] WATT, S., PAUL, S., OTHERS. "A Variable U Value Flowline Solution for Life-of-Field Thermal Management of Conventional and HPHT Fields". In: *SPE Offshore Europe Conference & Exhibition*. Society of Petroleum Engineers, 2017.

[79] GEERTSEN, C., PAILLUSSEAU, C., THOME, M., et al. "Deep Water Flowlines & Risers: Optimization of the Installed Cost & Thermal Performance Ex: the Shell Bonga Project". In: *The Seventeenth International Offshore and Polar Engineering Conference*. International Society of Offshore and Polar Engineers, 2007.

[80] AZEVEDO, F., TEIXEIRA, M., PORTESAN, G., et al. "Deepwater Insulation System for the Steel and Flexible Flowlines of Roncador Field in Brazil". In: *Offshore Technology Conference*. Offshore Technology Conference, 2001.

[81] KEÇEBAŞ, A., ALKAN, M. A., BAYHAN, M. "Thermo-economic analysis of pipe insulation for district heating piping systems", *Applied Thermal Engineering*, v. 31, n. 17-18, pp. 3929–3937, 2011.

[82] ERTÜRK, M. "Optimum insulation thicknesses of pipes with respect to different insulation materials, fuels and climate zones in Turkey", *Energy*, v. 113, pp. 991–1003, 2016.

[83] WECHSATOL, W., LORENTE, S., BEJAN, A. "Tree-shaped insulated designs for the uniform distribution of hot water over an area", *International Journal of Heat and Mass Transfer*, v. 44, n. 16, pp. 3111–3123, 2001.

[84] KAYNAKLI, O. "Economic thermal insulation thickness for pipes and ducts: A review study", *Renewable and Sustainable Energy Reviews*, v. 30, pp. 184–194, 2014.

[85] ÖZTÜRK, İ., KARABAY, H., BILGEN, E. "Thermo-economic optimization of hot water piping systems: A comparison study", *Energy*, v. 31, n. 12, pp. 2094–2107, 2006.

[86] LI, Y., CHOW, W. "Optimum insulation-thickness for thermal and freezing protection", *Applied energy*, v. 80, n. 1, pp. 23–33, 2005.

[87] KALYON, M., SAHIN, A. Z. "Application of optimal control theory in pipe insulation", *Numerical Heat Transfer: Part A: Applications*, v. 41, n. 4, pp. 391–402, 2002.

[88] ZAKI, G., AL-TURKI, A. "Optimization of multilayer thermal insulation for pipelines", *Heat transfer engineering*, v. 21, n. 4, pp. 63–70, 2000.

[89] CHIN, Y. D., BOMBA, J. G., OTHERS. "Structural and thermal optimization of cased insulated flowlines". In: *Offshore Technology Conference*. Offshore Technology Conference, 1999.

[90] ZHANG, H., LIANG, Y., MA, J., et al. "An improved PSO method for optimal design of subsea oil pipelines", *Ocean Engineering*, v. 141, pp. 154–163, 2017.

[91] FALUOMI, V., ARCIPRETI, P., OTHERS. "Pipeline Insulation Systems: State of Art and Design Methods". In: *Offshore Mediterranean Conference and Exhibition*. Offshore Mediterranean Conference, 2007.

[92] BÁRTA, P., KOPPERDAL, H., ŠINDLER, J., et al. "Automated Insulation Optimization for Subsea Equipment". In: *The Twenty-fourth International Ocean and Polar Engineering Conference*. International Society of Offshore and Polar Engineers, 2014.

[93] BAI, Y., BAI, Q. *Subsea pipelines and risers*. Elsevier, 2005.

[94] SHILLING, R., ALEXANDER, C., LIVESAY, R. "Limit State Design Based on Experimental Methods for High Pressure, High Temperature Riser and Pipeline Design". In: *International Conference on Offshore Mechanics and Arctic Engineering*, v. 44366, pp. 367–379, 2011.

[95] WANG, G., ZHAO, Z., CHEN, W., et al. "Stress analysis in the structural design of a pipeline at an offshore oil field". In: *ICPTT 2011: Sustainable Solutions For Water, Sewer, Gas, And Oil Pipelines*, pp. 798–809, 2011.

[96] HASAN, S., SWEET, L., HULTS, J., et al. "Corrosion risk-based subsea pipeline design", *International Journal of Pressure Vessels and Piping*, v. 159, pp. 1–14, 2018.

[97] SRISKANDARAJAH, T., RAGUPATHY, P., RAO, V., et al. "Design aspects of pipe-in-pipe systems for HP-HT applications". In: *Offshore Technology Conference*. Offshore Technology Conference, 2016.

[98] SRISKANDARAJAH, T., ANURUDRAN, G., RAGUPATHY, P., et al. "Design considerations in the use of pipe-in-pipe systems for Hp/Ht subsea pipelines". In: *The Ninth International Offshore and Polar Engineering Conference*. International Society of Offshore and Polar Engineers, 1999.

[99] SAHOTA, B., RAGUPATHY, P., WILKINS, R., et al. "Critical aspects of shell ETAP HP/HT pipe-in-pipe pipeline design and construction". In: *The Ninth International Offshore and Polar Engineering Conference*. International Society of Offshore and Polar Engineers, 1999.

[100] DE LUCENA, R. R., BAIOCO, J. S., DE LIMA, B. S. L. P., et al. "Optimal design of submarine pipeline routes by genetic algorithm with different constraint handling techniques", *Advances in Engineering Software*, v. 76, pp. 110–124, 2014.

[101] MAN, K.-F., TANG, K.-S., KWONG, S. "Genetic algorithms: concepts and applications [in engineering design]", *IEEE transactions on Industrial Electronics*, v. 43, n. 5, pp. 519–534, 1996.

[102] EBERHART, R., KENNEDY, J. "A new optimizer using particle swarm theory". In: *MHS'95. Proceedings of the Sixth International Symposium on Micro Machine and Human Science*, pp. 39–43. Ieee, 1995.

[103] DAO, S. D., ABHARY, K., MARIAN, R. "A bibliometric analysis of Genetic Algorithms throughout the history", *Computers & Industrial Engineering*, v. 110, pp. 395–403, 2017.

[104] BANIASSADI, A., SAJADI, B., AMIDPOUR, M., et al. "Economic optimization of PCM and insulation layer thickness in residential buildings", *Sustainable Energy Technologies and Assessments*, v. 14, pp. 92–99, 2016.

[105] GOLDENBERG, D. E. "Genetic algorithms in search, optimization and machine learning". 1989.

[106] KENNEDY, J. "Swarm intelligence". In: *Handbook of nature-inspired and innovative computing*, Springer, pp. 187–219, 2006.

[107] MAZHOUD, I., HADJ-HAMOU, K., BIGEON, J., et al. "Particle swarm optimization for solving engineering problems: a new constraint-handling mechanism", *Engineering Applications of Artificial Intelligence*, v. 26, n. 4, pp. 1263–1273, 2013.

[108] LI, C., ZHAI, R., LIU, H., et al. "Optimization of a heliostat field layout using hybrid PSO-GA algorithm", *Applied Thermal Engineering*, v. 128, pp. 33–41, 2018.

[109] NILASHI, M., BIN IBRAHIM, O., AHMADI, H., et al. "An analytical method for diseases prediction using machine learning techniques", *Computers & Chemical Engineering*, v. 106, pp. 212–223, 2017.

[110] LIU, Y., HORNE, R. N., OTHERS. "Interpreting pressure and flow-rate data from permanent downhole gauges by use of data-mining approaches", *SPE Journal*, v. 18, n. 01, pp. 69–82, 2012.

[111] GRIMSTAD, B., GUNNERUD, V., SANDNES, A., et al. "A simple data-driven approach to production estimation and optimization". In: *SPE Intelligent Energy International Conference and Exhibition*. Society of Petroleum Engineers, 2016.

[112] MANNODI-KANAKKITHODI, A., PILANIA, G., RAMPRASAD, R. "Critical assessment of regression-based machine learning methods for polymer dielectrics", *Computational Materials Science*, v. 125, pp. 123–135, 2016.

[113] TOMIN, N. V., KURBATSKY, V. G., SIDOROV, D. N., et al. "Machine learning techniques for power system security assessment", *IFAC-PapersOnLine*, v. 49, n. 27, pp. 445–450, 2016.

[114] LE, H. H., VIVIANI, J.-L. "Predicting bank failure: An improvement by implementing a machine-learning approach to classical financial ratios", *Research in International Business and Finance*, v. 44, pp. 16–25, 2018.

[115] M, S., H, L. "Eureqa (Version 0.98 beta) [Software]". 2014. Available in: <Availablefromwww.nutonian.com>.

[116] SCHMIDT, M., LIPSON, H. "Distilling free-form natural laws from experimental data", *science*, v. 324, n. 5923, pp. 81–85, 2009.

[117] YU, T., TENG, J., WONG, Y., et al. "Finite element modeling of confined concrete-I: Drucker–Prager type plasticity model", *Engineering structures*, v. 32, n. 3, pp. 665–679, 2010.

[118] PAZ, C. M., FU, G., ESTEFEN, S. F., et al. "Sandwich pipe: reel-lay installation effects". In: *International Conference on Offshore Mechanics and Arctic Engineering*, v. 56529, p. V05BT04A033. American Society of Mechanical Engineers, 2015.

[119] Y.NG, A. "Machine learning lecture notes". 2013.

[120] VAN DEN BERGH, F., ENGELBRECHT, A. P. "A cooperative approach to particle swarm optimization", *IEEE transactions on evolutionary computation*, v. 8, n. 3, pp. 225–239, 2004.

[121] CHENG, R., JIN, Y. "A social learning particle swarm optimization algorithm for scalable optimization", *Information Sciences*, v. 291, pp. 43–60, 2015.

[122] JORDEHI, A. R. "Enhanced leader PSO (ELPSO): a new PSO variant for solving global optimisation problems", *Applied Soft Computing*, v. 26, pp. 401–417, 2015.

[123] KENNEDY, J., MENDES, R. "Neighborhood topologies in fully informed and best-of-neighborhood particle swarms", *IEEE Transactions on Systems, Man, and Cybernetics, Part C (Applications and Reviews)*, v. 36, n. 4, pp. 515–519, 2006.

[124] LIU, P., LIU, J. "Multi-leader PSO (MLPSO): A new PSO variant for solving global optimization problems", *Applied Soft Computing*, v. 61, pp. 256–263, 2017.

[125] "Standard: DNVGL - DNV-OS-F101". out. 2013.

[126] ESCOBEDO, J. J. B., NIECKELE, A. O., AZEVEDO, L. F. A. "Transient thermal analysis in subsea pipelines". In: *Proceedings of the COBEM 2005: 18 th International Congress of Mechanical Engineering*, 2005.

[127] PETIT, A.-T., DULONG, P.-L. "Recherches sur quelques points importants de la Théorie de la Chaleur", *Annales de Chimie et de Physique (in French)*, , n. 10, pp. 395–413, 1819.

[128] "Volumetric heat capacity". fev. 2017. Available in: <https://en.wikipedia.org/w/index.php?title=Volumetric_heat_capacity&oldid=764844373>. Page Version ID: 764844373.

[129] DITTUS, F., BOELTER, L. "Heat transfer in automobile radiators of the tubular type", *International Communications in Heat and Mass Transfer*, v. 12, n. 1, pp. 3–22, 1985.

[130] CHEN, Z., HUANG, J., HE, Y., et al. "Non-uniform temperature fields of a deep-sea pipeline in steady flow", *J. Harbin Eng. Univ*, v. 38, n. 2, pp. 189–194, 2017.

[131] KAISER, M. J. "Offshore pipeline construction cost in the US Gulf of Mexico", *Marine Policy*, v. 82, pp. 147–166, 2017.

[132] "Questor". maio 2019.

[133] "Concrete Prices - How Much Does Concrete Cost? - The Concrete Network". . Available in: <https://www.concretenetwork.com/concrete-prices.html>.

[134] "2019 Concrete Prices | Concrete Truck Delivery Costs (Per Yard)". . Available in: <https://homeguide.com/costs/concrete-prices>.

[135] ESTEFEN, S. F., LOURENÇO, M. I., FENG, J., et al. "Sandwich pipe for long distance pipelines: flow assurance and costs". In: *International Conference on Offshore Mechanics and Arctic Engineering*, v. 49965, p. V005T04A025. American Society of Mechanical Engineers, 2016.

[136] PALMER, A. C., KING, R. A. *Subsea pipeline engineering*. PennWell Books, 2004.

[137] FEKETE, J. R., SOWARDS, J. W., AMARO, R. L. "Economic impact of applying high strength steels in hydrogen gas pipelines", *international journal of hydrogen energy*, v. 40, n. 33, pp. 10547–10558, 2015.

[138] "Seamless Steel Pipe,Tubing and Casing, API 5L line pipe- Bestar Steel Co., Ltd." . Available in: <http://www.bestarpipe.com/ASTM_A53-ASTM_A178-ASTM_A500-ASTM_A501-ASTM_A691-ASTM_A1020-ASTM_A252-ASTM_A672-EN_10219.html?gclid=EAIaIQobChMIi9a74ZD55AIVUwiRCh3COwAlEAAYASAAEgIVWvD_BwE>.

[139] COATH, G., HALGAMUGE, S. K. "A comparison of constraint-handling methods for the application of particle swarm optimization to constrained nonlinear optimization problems". In: *The 2003 Congress on Evolutionary Computation, 2003. CEC'03.*, v. 4, pp. 2419–2425. IEEE, 2003.

[140] SAHOO, L., BANERJEE, A., BHUNIA, A. K., et al. "An efficient GA–PSO approach for solving mixed-integer nonlinear programming problem in reliability optimization", *Swarm and Evolutionary Computation*, v. 19, pp. 43–51, 2014.

[141] "Thermocline". maio 2020. Available in: <https://en.wikipedia.org/w/index.php?title=Thermocline&oldid=956035863>. Page Version ID: 956035863.

[142] HIGHAM, D. J., HIGHAM, N. J. *MATLAB guide*. SIAM, 2016.

[143] SANDERS JR, J. L. "Nonlinear theories for thin shells", *Quarterly of Applied Mathematics*, v. 21, n. 1, pp. 21–36, 1963.

[144] HASHEMIAN, R. *Buckling analysis of sandwich pipes under external pressure*. Doctoral thesis, Université d'Ottawa/University of Ottawa, 2014.

[145] YOO, C. H., LEE, S. C. "Chapter 9 - Buckling of Thin Cylindrical Shell Elements". In: Yoo, C. H., Lee, S. C. (Eds.), *Stability of Structures*, Butterworth-Heinemann, pp. 441–474, Boston, jan. 2011. ISBN: 978-0-12-385122-2. doi: 10.1016/B978-0-12-385122-2.10009-0. Available in: <http://www.sciencedirect.com/science/article/pii/B9780123851222100090>.

Appendix A

Analytical solution for elastic collapse pressure of the SP

A long SP subjected to a gradually increasing external hydrostatic pressure is considered. It is required to determine the external pressure at which the SP will collapse.

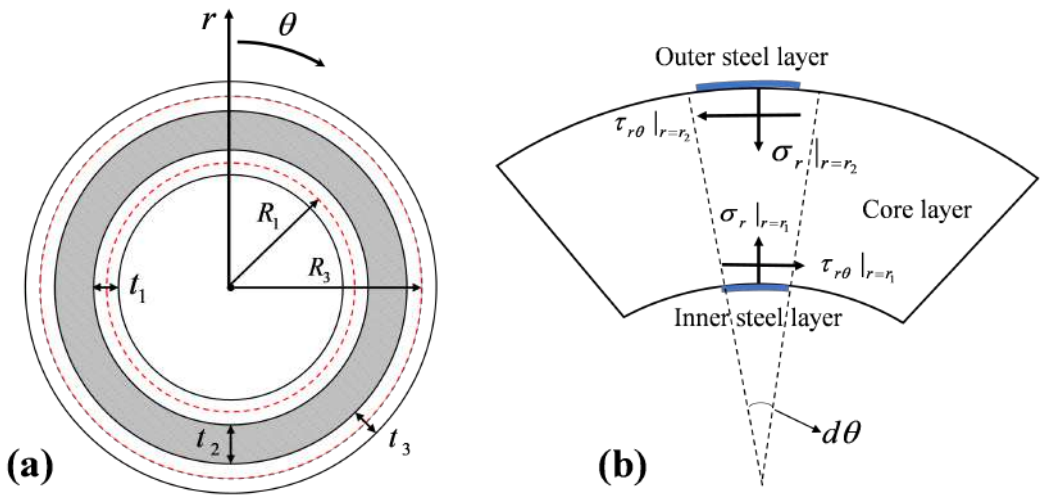

Figure A.1: (a) Geometry of the sandwich pipe cross-section; (b) Stresses at the interfaces between the core layer and the steel layers

Figure A.1 shows the cross-section of a sandwich pipe and the stresses at the contact surfaces. R_1 is the radius of the inner steel layer at the middle surface and R_3 is that of the outer steel layer. The interfaces between the core layer and the steel layers are defined by the outside radius of the inner steel layer, $r_1 = R_1 + \frac{t_1}{2}$ and that of the core layer,$r_2 = R_3 - \frac{t_3}{2}$ The external hydrostatic pressure is to be determined at which the sandwich pipe would collapse.
The following assumptions are made:

- The SP is considered a perfect cylinder.

- Since the pipe length is several orders of magnitude larger than the pipe radius, the problem can be idealized as a plane strain problem.
- SP materials are assumed linearly elastic and isotropic.
- The SP is subject only to external hydrostatic pressure.
- A linear kinematic relation is applied to the core layer.
- Kirchhoff's assumption holds for the steel layers.

For the steel layers, the circumferential strain of any point throughout the layer can be expressed as:

$$\epsilon_{\theta,i} = \epsilon^0_{\theta,i} + zk_{\theta,i}, \quad i = 1, 3 \tag{A.1}$$

where $\epsilon^0_{\theta,i}$ is the circumferential strain at the middle surface of the i-th layer, z is the distance from the middle surface, and $k_{\theta,i}$ is the curvature of the i-th layer. $i = 1$ stands for inner steel layer and $i = 3$ stands for outer steel layer.

Sander's equation [143] is employed for the displacement and strain relations:

$$\epsilon^0_{\theta,i} = \frac{v_i^{'} + w_i}{R_i} + \frac{1}{2}(\frac{v_i - w_i^{'}}{R_i})^2, \quad i = 1, 3 \tag{A.2}$$

$$k_{\theta,i} = \frac{v_i^{'} - w_i^{''}}{{R_i}^2} \tag{A.3}$$

where w_i and v_i are respectively the radial and circumferential displacements of the mid-surface of the i-th layer.

The constitutive equation for the steel layers is:

$$\sigma_{\theta,i} = \frac{E_p}{1 - {v_p}^2}\epsilon_{\theta,i}, \quad i = 1, 3 \tag{A.4}$$

where $\sigma_{\theta,i}$ is the stress of the i-th layer, E_p is the elastic modulus of steel, and v_p is the poisson's ratio of steel.

The total energy of the SP (U_{total}) per unit length due to non-circular configuration is given by:

$$U_{total} = U_1 + U_2 + U_3 + W_p \tag{A.5}$$

Where U_1 is the strain energy of the inner steel layer, U_2 is the strain energy of the core layer, U_3 is the strain energy of the outer steel layer, and W_p is the work done by the external pressure.

The strain energy of the steel layers can be expressed as:

$$U_i = \int (\frac{1}{2}\epsilon\sigma)dV = \int_{-t/2}^{t/2}\int_0^{2\pi} \frac{1}{2}(\epsilon_{\theta,i}\sigma_{\theta,i})R_i d\theta dz, \quad i = 1,3 \tag{A.6}$$

Adding Equations A.1 - A.4 into Equation A.6 , U_1 and U_3 can be written as:

$$\begin{aligned} U_i =& \frac{R_i E_p t_i}{2(1-{v_p}^2)} \int_0^{2\pi} \left\{ \frac{{v_i}' + w_i}{R_i} + \frac{1}{2}(\frac{v_i - {w_i}'}{R_i})^2 \right\}^2 d\theta + \\ & \frac{R_i E_p {t_i}^3}{24(1-{v_p}^2)} \int_0^{2\pi} (\frac{{v_i}' - {w_i}''}{{R_i}^2})^2 d\theta, \qquad i = 1,3 \end{aligned} \tag{A.7}$$

The strain energy of the core layer (U_2) can be expressed as the work done by the entire layer's stresses applied to inner and outer steel layers at the interfaces:

$$\begin{aligned} U_2 = & \int_0^{2\pi} (\sigma_r|_{r=r_1}\, w_1|_{r=r_1} + \tau_{r\theta}|_{r=r_1} \times v_1|_{r=r_1}) r_1 d\theta + \\ & \int_0^{2\pi} (\sigma_r|_{r=r_2}\, w_3|_{r=r_2} + \tau_{r\theta}|_{r=r_2} \times v_3|_{r=r_2}) r_2 d\theta \end{aligned} \tag{A.8}$$

where σ_r is the radial stress and $\tau_{r\theta}$ is the shear stress of the core layer.

The work done by the external pressure (P) on the outside surface of the outer steel layer is [144]:

$$W_p = P r_3 \int_0^{2\pi} [w_3 + \frac{1}{2r_3}({v_3}^2 + {w_3}^2 - v_3 {w_3}' + {v_3}' w_3)] d\theta \tag{A.9}$$

Substituting Equations A.7 – A.9 into Equation A.5 yields the expression of U_{total} which is a functional of the displacements and their derivatives of the inner and outer steel layer mid-surfaces:

$$U_{total} = \int_0^{2\pi} F(v_1, w_1, v_3, w_3, {v_1}', {w_1}', {v_3}', {w_3}', {w_1}'', {w_3}'') d\theta \tag{A.10}$$

The displacement functions $(v_1(\theta), w_1(\theta), {v_1}'(\theta), {w_1}'(\theta)...)$ should ensure that the total potential function remain at minimum value. Thus, the first order variation of the functional should be zero.

$$\begin{aligned} \delta U_{total} = \int_0^{2\pi} \Bigg(& \frac{\partial F}{\partial v_1}\delta v_1 + \frac{\partial F}{\partial w_1}\delta w_1 + \frac{\partial F}{\partial v_3}\delta v_3 + \frac{\partial F}{\partial w_3}\delta w_3 + \frac{\partial F}{\partial {v_1}'}\delta {v_1}' + \frac{\partial F}{\partial {w_1}'}\delta {w_1}' + \\ & \frac{\partial F}{\partial {v_3}'}\delta {v_3}' + \frac{\partial F}{\partial {w_3}'}\delta {w_3}' + \frac{\partial F}{\partial {w_1}''}\delta {w_1}'' + \frac{\partial F}{\partial {w_3}''}\delta {w_3}'' \Bigg) d\theta = 0 \end{aligned} \tag{A.11}$$

By applying integration by parts, the Euler-Lagrange equations that define the displacement functions can be obtained:

$$\frac{\partial F}{\partial v_i} - \frac{\partial}{\partial \theta}(\frac{\partial F}{\partial v_i{}'}) = 0, \qquad i = 1, 3 \tag{A.12a}$$

$$\frac{\partial F}{\partial w_i} - \frac{\partial}{\partial \theta}[\frac{\partial F}{\partial w_i{}'} - \frac{\partial}{\partial \theta}(\frac{\partial F}{\partial w_i{}''})] = 0, \qquad i = 1, 3 \tag{A.12b}$$

The equilibrium equations of the SP system can be established by adding Equation A.10 into Equation A.12 :

$$M_{\theta,1}{}'' - R_1 N_{\theta,1} - R_1 (N_{\theta,1}\beta_1)' - R_1\sigma_r \mid_{r=r_1} = 0 \tag{A.13a}$$

$$R_1 N_{\theta,1}{}' + M_{\theta,1}{}' - R_1 N_{\theta,1}\beta_1 + R_1\tau_{r\theta} \mid_{r=r_1} = 0 \tag{A.13b}$$

$$M_{\theta,3}{}'' - R_3 N_{\theta,3} - R_3 (N_{\theta,3}\beta_3)' - PR_3(v_3{}' + w_3) + R_3\sigma_r \mid_{r=r_2} = Pr_3{}^2 \tag{A.13c}$$

$$R_3 N_{\theta,3}{}' + M_{\theta,3}{}' - R_3 N_{\theta,3}\beta_3 - PR_3{}^2\beta_3 - R_3\tau_{r\theta} \mid_{r=r_2} = 0 \tag{A.13d}$$

Where

$$N_{\theta,i} = \frac{E_p t_i}{1 - v_p{}^2}[\frac{v_i{}' + w_i}{R_i} + \frac{1}{2}(\frac{v_i - w_i{}'}{R_i})^2], \qquad i = 1, 3 \tag{A.14}$$

$$M_{\theta,i} = \frac{E_p t_i{}^3}{12(1 - v_p{}^2)}(\frac{v_i{}' - w_i{}''}{R_i{}^2}), \qquad i = 1, 3 \tag{A.15}$$

$$\beta_i = \frac{v_i{}' - w_i{}''}{R_i{}^2}, \qquad i = 1, 3 \tag{A.16}$$

Equations A.13 - A.16 can be solved numerically for the elastic collapse pressure of the SP under external pressure. For an analytical solution, the equations governing the elastic buckling of the SP need to be developed using the equilibrium equations. Several approaches are suitable for this purpose, like setting the second variation of U_{total} to zero or applying adjacent equilibrium criterion [145]. In the thesis, bifurcation buckling equations are established by perturbing the pre-buckling state with the buckling mode $(\widetilde{v_1}, \widetilde{w_1}, \widetilde{v_3}, \widetilde{w_3})$ and linearizing Equations (A.13), which results in the following:

$$\frac{E_p}{1-{v_p}^2}\left(\frac{t_1}{R_1}\right)(w_1+{v_1}^{'}) + \frac{E_p}{12(1-{v_p}^2)}\left(\frac{t_1}{R_1}\right)^3(v_1-{w_1}^{'})''' - R_1\sigma_r\mid_{r=r_1}=0 \tag{A.17a}$$

$$\frac{E_p}{1-{v_p}^2}\left(\frac{t_1}{R_1}\right)(w_1+{v_1}^{'})' + \frac{E_p}{12(1-{v_p}^2)}\left(\frac{t_1}{R_1}\right)^3(v_1-{w_1}^{'})'' + R_1\tau_{r\theta}\mid_{r=r_1}=0 \tag{A.17b}$$

$$\frac{E_p}{1-{v_p}^2}\left(\frac{t_3}{R_3}\right)(w_3+{v_3}^{'}) - \frac{E_p}{12(1-{v_p}^2)}\left(\frac{t_3}{R_3}\right)^3(v_3-{w_3}^{'})''' + P(v_3+{w_3}^{''}) + R_3\sigma_r\mid_{r=r_2}=0 \tag{A.17c}$$

$$\frac{E_p}{1-{v_p}^2}\left(\frac{t_3}{R_3}\right)(w_3+{v_3}^{'})' + \frac{E_p}{12(1-{v_p}^2)}\left(\frac{t_3}{R_3}\right)^3(v_3-{w_3}^{'})'' - R_3\tau_{r\theta}\mid_{r=r_2}=0 \tag{A.17d}$$

As shown in Equation A.17, the elastic collapse pressure of the SP system can be determined once $\sigma_r\mid_{r=r_1}$, $\tau_{r\theta}\mid_{r=r_1}$, $\sigma_r\mid_{r=r_2}$ and $\tau_{r\theta}\mid_{r=r_2}$ are obtained. Thus, the stress function is employed for the core layer. The compatibility equation of the core layer stress function is expressed as:

$$(\frac{\partial^2}{\partial r^2}+\frac{1}{r}\frac{\partial}{\partial r}+\frac{1}{r^2}\frac{\partial^2}{\partial\theta^2})(\frac{\partial^2\phi(r,\theta)}{\partial r^2}+\frac{1}{r}\frac{\partial\phi(r,\theta)}{\partial r}+\frac{1}{r^2}\frac{\partial^2\phi(r,\theta)}{\partial\theta^2})=0 \tag{A.18}$$

The radial and circumferential normal stresses $(\sigma_r, \sigma_\theta)$ and the shear stress $(\tau_{r\theta})$ are obtained from:

$$\sigma_r = \frac{1}{r}\frac{\partial\phi(r,\theta)}{\partial r}+\frac{1}{r^2}\frac{\partial^2\phi(r,\theta)}{\partial\theta^2} \tag{A.19a}$$

$$\sigma_\theta = \frac{\partial^2\phi(r,\theta)}{\partial r^2} \tag{A.19b}$$

$$\tau_{r\theta} = -\frac{\partial}{\partial r}(\frac{1}{r}\frac{\partial\phi(r,\theta)}{\partial\theta}) \tag{A.19c}$$

The stress function is assumed to have circumferentially periodic forms written as:

$$\phi(r,\theta) = f_n(r)\cos n\theta \tag{A.20}$$

where n is the buckling mode number. Substituting Equation A.20 into Equation A.18 yields:

$$(\frac{d^2}{dr^2} + \frac{1}{r}\frac{d}{dr} - \frac{n^2}{r^2})(\frac{d^2 f_n(r)}{dr^2} + \frac{1}{r}\frac{df_n(r)}{dr} - \frac{n^2}{r^2}f_n(r)) = 0 \tag{A.21}$$

The general solutions of EquationA.21 is:

$$f_n(r) = A_n r^{-n} + B_n r^{2-n} + C_n r^{2+n} + D_n r^n (n >= 2) \tag{A.22}$$

where A_n , B_n , C_n and D_n are arbitrary constants. Replacing corresponding items in Equation A.19 by Equations A.20 and A.22, the expressions of the core layer stresses are obtained:

$$\begin{aligned}\sigma_r = -\{&A_n n(n+1)r^{-n-2} + B_n(n-1)(n+2)r^{-n} \\ &+ C_n(n+1)(n-2)r^n + D_n n(n-1)r^{n-2}\}\cos n\theta\end{aligned} \tag{A.23a}$$

$$\begin{aligned}\sigma_\theta = \{&A_n n(n+1)r^{-n-2} + B_n(n-1)(n-2)r^{-n} \\ &+ C_n(n+1)(n-2)r^n + D_n n(n-1)r^{n-2}\}\cos n\theta\end{aligned} \tag{A.23b}$$

$$\begin{aligned}\tau_{r\theta} = \{&-A_n n(n+1)r^{-n-2} + B_n n(n-1)r^{-n} \\ &+ C_n n(n+1)r^n + D_n n(n-1)r^{n-2}\}\sin n\theta\end{aligned} \tag{A.23c}$$

As shown in Equation A.23, the core layer stresses can be determined once A_n , B_n , C_n and D_n are defined. The strain components of the core layer for plane strain problem are derived as:

$$\begin{Bmatrix} \epsilon_r \\ \epsilon_\theta \\ \gamma_{r\theta} \end{Bmatrix} = \frac{1}{E_c}\begin{bmatrix} 1-{v_c}^2 & -v_c(1+v_c) & 0 \\ -v_c(1+v_c) & 1-{v_c}^2 & 0 \\ 0 & 0 & 2(1+v_c) \end{bmatrix}\begin{Bmatrix} \sigma_r \\ \sigma_\theta \\ \tau_{r\theta} \end{Bmatrix} \tag{A.24}$$

where E_c and v_c are respectively the elastic modulus and the Poisson's ratio of the core layer.

A linear displacement-strain relationship is assumed for the core layer. And the core layer displacements in the radial and circumferential directions are obtained from Equations A.23 and A.24:

$$
\begin{aligned}
w_2(r,\theta) &= \int \epsilon_r dr \\
&= \frac{1+v_c}{E_c}\{A_n n r^{-n-1} + B_n(n-4v_c+2)r^{1-n} \\
&\quad - C_n(n+4v_c-2)r^{n+1} - D_n n r^{n-1}\}\cos n\theta + G_1
\end{aligned} \tag{A.25a}
$$

$$
\begin{aligned}
v_2(r,\theta) &= \int (r\epsilon_\theta - w)d\theta \\
&= \frac{1+v_c}{E_c}\{A_n n r^{-n-1} + B_n(n+4v_c-4)r^{1-n} \\
&\quad - C_n(n-4v_c+4)r^{n+1} + D_n n r^{n-1}\}\sin n\theta + G_2
\end{aligned} \tag{A.25b}
$$

where G_1 and G_2 are the integration constants. The middle surface displacements of the steel layers are taken to have circumferentially periodic forms as:

$$
\begin{aligned}
w_1 &= W_1 \cos n\theta, \qquad & v_1 &= V_1 \sin\theta \\
w_3 &= W_3 \cos n\theta, \qquad & v_3 &= V_3 \sin\theta
\end{aligned} \tag{A.26}
$$

where W_1 , V_1 , W_3 , and V_3 are the maximum displacements at the middle surfaces of the steel layers.

Assuming a perfect bonded inter-layer relation, the displacements at the interfaces between the core layer and the steel layers should equal, see Equation A.27.

$$w_2(r_1,\theta) = W_1 \cos n\theta \tag{A.27a}$$

$$v_2(r_1,\theta) = V_1 \sin n\theta + (\frac{nt_1}{2R_1}W_1 + \frac{t_1}{2R_1}V_1)\sin n\theta \tag{A.27b}$$

$$w_2(r_2,\theta) = W_3 \cos n\theta \tag{A.27c}$$

$$v_2(r_2,\theta) = V_3 \sin n\theta + (\frac{nt_3}{2R_3}W_3 + \frac{t_3}{2R_3}V_3)\sin n\theta \tag{A.27d}$$

From Equations A.25 and A.27, the arbitrary constants A_n , B_n , C_n and D_n in Equation A.23 can be expressed by W_1 , V_1 , W_3 , and V_3 , see Equation A.28 .

$$
M_c \begin{Bmatrix} A_n \\ B_n \\ C_n \\ D_n \end{Bmatrix} = \begin{Bmatrix} W_1 \\ V_1 \\ W_3 \\ V_3 \end{Bmatrix} \quad \rightarrow \quad \begin{Bmatrix} A_n \\ B_n \\ C_n \\ D_n \end{Bmatrix} = {M_c}^{-1} \begin{Bmatrix} W_1 \\ V_1 \\ W_3 \\ V_3 \end{Bmatrix} \tag{A.28}
$$

where

$$M_c = \begin{bmatrix} nR_1{}^{-n-1} & (n-4v_c+2)R_1{}^{1-n} & -(n+4v_c-2)R_1{}^{1+n} & -nR_1{}^{n-1} \\ nR_1{}^{-n-1} & (n+4v_c-2)R_1{}^{1-n} & (n-4v_c+4)R_1{}^{1+n} & nR_1{}^{n-1} \\ nR_3{}^{-n-1} & (n-4v_c+2)R_3{}^{1-n} & -(n+4v_c-2)R_3{}^{1+n} & -nR_3{}^{n-1} \\ nR_3{}^{-n-1} & (n+4v_c-2)R_3{}^{1-n} & (n-4v_c+4)R_3{}^{1+n} & nR_3{}^{n-1} \end{bmatrix} \quad \text{(A.29)}$$

Further, from Equations A.17, A.23 and A.28, the core layer stresses at the interfaces, $\sigma_r \mid_{r=r_1}$, $\tau_{r\theta} \mid_{r=r_1}$, $\sigma_r \mid_{r=r_2}$ and $\tau_{r\theta} \mid_{r=r_2}$, can be expressed by the maximum displacements of the steel layers at the middle surface, Equation A.29.

$$\begin{Bmatrix} \sigma_r \mid_{r=r_1} \\ \tau_{r\theta} \mid_{r=r_1} \\ \sigma_r \mid_{r=r_2} \\ \tau_{r\theta} \mid_{r=r_2} \end{Bmatrix} = M_b \times \begin{Bmatrix} A_n \\ B_n \\ C_n \\ D_n \end{Bmatrix} = M_b \times M_c{}^{-1} \times \begin{Bmatrix} W_1 \\ V_1 \\ W_3 \\ V_3 \end{Bmatrix} \quad \text{(A.30)}$$

where:

$$M_b = \begin{bmatrix} -n(n+1)R_1{}^{-n-2} & (1-n)(n+2)R_1{}^{-n} & (n+1)(2-n)R_1{}^{n} & n(1-n)R_1{}^{n-2} \\ -n(n+1)R_1{}^{-n-2} & (1-n)nR_1{}^{-n} & (n+1)nR_1{}^{n} & n(n-1)R_1{}^{n-2} \\ -n(n+1)R_3{}^{-n-2} & (1-n)(n+2)R_3{}^{-n} & (n+1)(2-n)R_3{}^{n} & n(1-n)R_3{}^{n-2} \\ -n(n+1)R_3{}^{-n-2} & (1-n)nR_3{}^{-n} & (n+1)nR_3{}^{n} & n(n-1)R_3{}^{n-2} \end{bmatrix} \quad \text{(A.31)}$$

Substituting Equations A.30 and A.26 into the Equation A.17 gives:

$$\left\{ \begin{bmatrix} c_{11} & c_{12} & & \\ c_{21} & c_{22} & & \\ & & c_{33} & c_{34} \\ & & c_{43} & c_{44} \end{bmatrix} + M_b \times M_c{}^{-1} \right\} \begin{Bmatrix} W_1 \\ V_1 \\ W_3 \\ V_3 \end{Bmatrix} = 0 \quad \text{(A.32)}$$

where:

$$c_{11} = \frac{E_p t_1}{R_1(1-{v_p}^2)}\left[1+\frac{1}{12}\left(\frac{t_1}{R_1}\right)^2 n^4\right] \tag{A.33a}$$

$$c_{12} = -c_{21} = \frac{E_p t_1 n}{R_1(1-{v_p}^2)}\left[1+\frac{1}{12}\left(\frac{t_1}{R_1}\right)^2 n^2\right] \tag{A.33b}$$

$$c_{22} = -\frac{E_p t_1 n^2}{R_1(1-{v_p}^2)}\left[1+\left(\frac{t_1}{R_1}\right)^2\right] \tag{A.33c}$$

$$c_{33} = \frac{E_p t_3}{R_3(1-{v_p}^2)}\left[1+\frac{1}{12}\left(\frac{t_3}{R_3}\right)^2 n^4\right] + P(1-n^2) \tag{A.33d}$$

$$c_{34} = -c_{43} = \frac{E_p t_3 n}{R_3(1-{v_p}^2)}\left[1+\frac{1}{12}\left(\frac{t_3}{R_3}\right)^2 n^2\right] \tag{A.33e}$$

$$c_{44} = -\frac{E_p t_3 n^2}{R_3(1-{v_p}^2)}\left[1+\frac{1}{12}\left(\frac{t_3}{R_3}\right)^2\right] \tag{A.33f}$$

The Equation A.32 is a linear homogeneous equation and the determinant of the coefficients must equal zero for a non-trivial solution. Thus, the elastic collapse pressure of the SP can be calculated by setting the coefficient determinant to zero.

Note that the Equation A.27 defines the inter-layer relation between the core layer and the steel layers, by substituting the Equations A.27b and A.27d with the following:

$$\tau_{r\theta}\,|_{r=r_1} = 0 \tag{A.34a}$$

$$\tau_{r\theta}\,|_{r=r_2} = 0 \tag{A.34b}$$

With the shear stress on the interface equal zero, the analytical solution for the elastic collapse pressure of the SP with frictionless inter-layer condition at tangential direction can be established. The solution is proposed by Taheri et al. [32].